Unconventional superconductivity of the heavy fermion compound UNi_2Al_3

Dissertation

zur Erlangung des Grades

Doktor der Naturwissenschaften (Dr. rer. nat.)

am Fachbereich Physik

der Johannes Gutenberg-Universität Mainz

von

Andrey Zakharov

geb. in Kharkiv, Ukraine

univer
sität
mainz

Mainz, 2008

Contents

List of Figures

List of Tables

Introduction

Heavy fermion systems are rare earth or actinide intermetallic compounds in which local magnetic moments dominate the dynamics of the itinerant electrons. These compounds are known to develop strong electronic correlations at low temperature, resulting in a pronounced increase of the effective quasiparticle mass, which may be as large as several hundred times the free electron mass.

The phenomenon of superconductivity in heavy fermion materials was first discovered in 1979 by Steglich et. al. during an investigation of the low-temperature properties of $CeCu_2Si_2$ [1]. Later, superconductivity was observed in many other heavy fermion materials [2, 3, 4]. Some examples are UPt_3 [5], UBe_{13} [6], URu_2Si_2 [7], UPd_2Al_3 [8], and UNi_2Al_3 [9], which exhibit superconductivity in coexistence with magnetic order. In contrast to conventional superconductors, in which the attractive electron-electron interaction is mediated by phonons, in heavy fermion superconductors due to an unconventional properties of superconducting state [10, 11, 12] an alternative pairing mechanism is considered to be possible [13, 14]. However, different superconducting and magnetic properties are observed in many of these complex metals, and the understanding of the superconducting pairing interaction in heavy fermion systems is of interest to a wide community.

Recently, clear progress concerning the superconductivity of the heavy fermion compound UPd_2Al_3 was reported. Combined experimental investigations based on tunneling spectroscopy on planar thin film junctions [15] and inelastic neutron scattering [16, 17, 18], gave evidence for an unconventional mechanism of superconductivity. The Cooper pair formation in this compound is believed to be mediated by magnetic excitations. However, the question whether these excitations are spin fluctuations [19] or magnetic excitons [18, 20, 21] is not finally answered. In this framework the investigation of the compound UNi_2Al_3, which is isostructural to UPd_2Al_3, is of great interest.

In the present work the preparation, characterization, and electronic property investigations of UNi_2Al_3 single crystalline thin film samples are discussed. The

first chapter of this thesis introduces the heavy fermion superconductors UNi_2Al_3 and UPd_2Al_3. Here, a short summary of known theoretical and experimental data is given and the superconducting and magnetic properties of these isostructural compounds are compared. The second chapter gives a short introduction to the experimental methods of preparation and crystallographic quality investigation of thin film samples. The employed MBE system is presented, and the applied methods of crystallographic characterization are illustrated. The following chapter describes the details of the preparation process. The growth of (100)-oriented UNi_2Al_3 thin films on different substrate types is discussed, the crystallographic quality of thin film samples is evaluated, and the optimized deposition parameters are given. The fourth chapter presents the magnetic structure study of UNi_2Al_3 thin films by means of resonant magnetic x-ray scattering. The magnetic order of thin film samples, the formation of the magnetic domains, depending on the moment direction, and the magnetic correlation length are discussed. In the fifth chapter a survey of the transport measurements is presented. The behavior of the temperature dependent resistivity and of the upper critical magnetic field of UNi_2Al_3 thin films is analyzed. Chapter 6 presents the results of the tunneling spectroscopy experiments. The preparation of various types of planar junctions is described, and the measured tunneling conductivities are discussed in the framework of junction quality and barrier effects.

Chapter 1

The heavy fermion superconductors UNi$_2$Al$_3$ and UPd$_2$Al$_3$

Superconductivity of the compounds UNi$_2$Al$_3$ and UPd$_2$Al$_3$ was discovered by C. Geibel et al. in 1991 in the framework of a systematical search for new heavy fermion superconductors. Both systems exhibit the coexistence of superconductivity and magnetism at low temperatures and are considered to be unconventional superconductors with a non-phononic Cooper pairing mechanism. Although UNi$_2$Al$_3$ and UPd$_2$Al$_3$ are isostructural compounds, their magnetic and superconducting properties are quite different. Therefore a comparison of these materials is a key to the understanding of the interplay between magnetism and superconductivity in heavy fermion superconductors.

1.1   Crystallographic structure

Both compounds UNi$_2$Al$_3$ and UPd$_2$Al$_3$ crystallize in the hexagonal PrNi$_2$Al$_3$ structure within the space group P6/mmm [9, 8] (Figure 1.1). The Pd atoms have a larger radius than Ni atoms, that explains the different lattice parameters, which amount to a=0.5207 nm and c=0.4017 nm for UNi$_2$Al$_3$, and a=0.5365 nm, c=0.4184 nm for UPd$_2$Al$_3$, respectively. The uranium atoms are located at the edges of the hexagonal unit cell, which leads to a large atom separation and, as a consequence, to an enhancement of the localized character of the uranium f-electrons, which is a prerequisite for heavy fermion behavior. The larger lattice

parameters of UPd$_2$Al$_3$ and consequently the large distance between uranium atoms leads to the uranium f-electrons in UPd$_2$Al$_3$ being even more localized than in UNi$_2$Al$_3$.
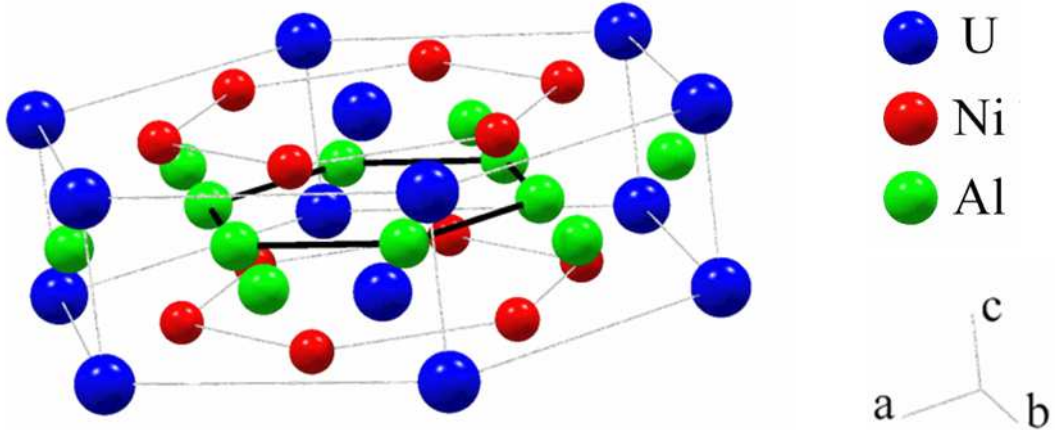
Figure 1.1: PrNi$_2$Al$_3$ hexagonal structure. In the upper and lower ab-planes of the structure the uranium and nickel atoms are situated. The aluminum atoms form the intermediate layer.

1.2   Magnetic structure

Since the magnetic structure of these compounds is typically investigated using single crystal bulk samples by means of inelastic neutron scattering, many more experiments were performed on UPd$_2$Al$_3$ than on UNi$_2$Al$_3$ because of the better quality and larger size of available crystals.

UPd$_2$Al$_3$ orders into a simple antiferromagnetic structure below $T_{\mathrm{N}} = 14.3\,\mathrm{K}$. The commensurate magnetic order is described with a propagation vector $Q_{\mathrm{UPA}} = (0, 0, \frac{1}{2})$ in the hexagonal reciprocal lattice units. The ordered moments are about $0.85\,\mu_{\mathrm{B}}$ at low T and coupled antiferromagnetically along the c-axis and ferromagnetically within ab-planes [22]. In UNi$_2$Al$_3$ the magnetic ordering temperature is lower, $T_{\mathrm{N}} = 5\,\mathrm{K}$, the moment smaller, $\mu \simeq 0.2\,\mu_B$, and the magnetic structure as determined in bulk single crystals has an incommensurate propagation vector $Q_{\mathrm{UNA}} = (\pm\frac{1}{2} \pm 0.11, 0, \frac{1}{2})$ [23, 24]. The authors of Ref. [25] have established that the magnetic structure in zero field is an amplitude modulated magnetization

density wave with the magnetic moments parallel to a^*.

Such a significant difference in the magnetic structure of these crystallographically isostructural compounds may results in different unconventional superconducting pairing mechanisms.

1.3 Superconducting and magnetic properties

UNi_2Al_3 and UPd_2Al_3 become superconducting at $T_c^{UNA} \approx 1\,K$ and $T_c^{UPA} \approx 2\,K$, respectively. The large value of both specific-heat jumps at T_c and the Sommerfeld coefficient of the electronic normal-state specific heat, $\gamma = 140\,mJ/K^2$ for UPd_2Al_3 and $\gamma = 120\,mJ/K^2$ for UNi_2Al_3, point to the formation of a heavy fermion pairing states below T_c. Like with all other heavy fermion superconductors the mechanisms of the Cooper pair formation in UNi_2Al_3 and UPd_2Al_3 are of great interest.

For the same reason as in the case of magnetic structure studies, there is much more progress in the investigation of the superconducting properties of UPd_2Al_3 than of UNi_2Al_3. NMR measurements of UPd_2Al_3 have shown, that the nuclear relaxation rate $1/T_1$ behaves like T^3 in the superconducting state and the Knight shift decreases below T_c independent of the direction of the magnetic field, pointing out a spin-singlet superconductivity with a line-node gap [26, 27]. Measurements of the temperature dependence of the upper critical field reveal a strong Pauli limiting effect in UPd_2Al_3, suggesting an even parity superconducting order parameter [28]. A whole series of neutron scattering experiments have been performed on UPd_2Al_3 single crystals [16, 17, 18]. The observation of a weak suppression of the antiferromagnetic Bragg intensity at $Q = (0, 0, 1/2)$ below T_c together with increasing spin wave excitation energy and linewidth indicates the strong coupling between magnetism and superconductivity in UPd_2Al_3. Employing a thin film technique it was possible to prepare UPd_2Al_3-based tunneling junctions and to probe the superconducting energy gap directly [15]. In the left panel of Figure 1.2 the normalized differential tunneling conductivity of UPd_2Al_3–AlO_x–Pb planar junction at $T = 0.3\,K$ in magnetic field of $\mu_0 H = 0.3\,T$, which suppresses the superconductivity of the lead counter electrode, and the corresponding Dynes fit are shown. A clear superconducting gap of UPd_2Al_3 with a gap width of at $\Delta = 235\,\mu eV$ can be identified. Moreover, at the bias voltage of about $V_B \approx 1.2\,meV$, conductivity modulations, which could not be described by a standard Dynes fit, were observed (left inset of Figure 1.2). Since the mod-
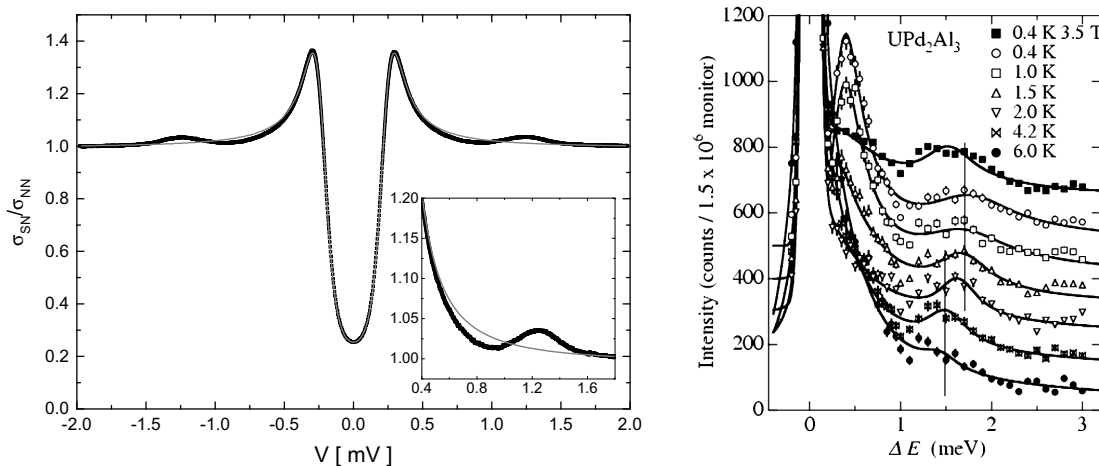
Figure 1.2: Left pannel: NIS spectroscopy on UPd$_2$Al$_3$ along the c-axis, at $T = 0.3\,$K, $\mu_0 H = 0.3\,$T, with corresponding Dynes-fit (grey). Inset: Strong coupling features. Figure taken from M. Jourdan, PhD-thesis [29].

Right pannel: Temperature dependence of the neutron inelastic scattering profile of UPd$_2$Al$_3$ measured at $Q = (0,0,1/2)$. Figure taken from Metoki et al. [16].

ulations in the tunneling spectrum were observed in the same energy range as a gapped spin wave mode in inelastic neutron scattering profiles (Figure 1.2), these features can be explained by a strong coupling effect of the charge carriers with magnetic excitations. Thus, the combination of tunneling spectroscopy and inelastic neutron scattering experiments gave compelling evidence that superconductivity in UPd$_2$Al$_3$ is mediated by antiferromagnetic spin fluctuations inducing a presumably d-wave order parameter without symmetry reduction.

In contrast to UPd$_2$Al$_3$ the superconducting nature of UNi$_2$Al$_3$ has been studied only by a few experiments. Moreover, the quality of the only available single crystal samples leave much to be desired. Measurements of the upper critical field on the very first samples reveal a strong anisotropy of the $H_{c2}(T)$ curves depending on the field direction. The authors of Ref. [30] have found, that the upper critical field H_{c2} for $H \parallel a$ is much larger than for $H \parallel c$. Moreover, no influence of a paramagnetic limitation was observed. Recent measurements by Terashima et al. reveal much less anisotropy of H_{c2} than previously reported, but they still argue that the upper critical field in UNi$_2$Al$_3$ is dominated by orbital effects [31]. Additionally, the ^{27}Al Knight shift measurements reveal, that in contrast to UPd$_2$Al$_3$ the spin part of the Knight shift in UNi$_2$Al$_3$ does not change down to 50 mK across the superconducting transition temperature [32]. Thus,

based on the $H_{c2}(T)$ and Knight shift measurement, the authors suggest that in contrast to UPd$_2$Al$_3$ a spin triplet pairing takes place in UNi$_2$Al$_3$.

To this day there are no successful attempts to investigate the superconducting gap of UNi$_2$Al$_3$ directly by spectroscopic means. The main problem which experimentalists have to solve is obviously suppressed superconductivity in the surface region of the samples. By ex-situ methods such as point-contact spectroscopy the probed surface layer can be oxidized. But even vacuum tunneling spectroscopy on in-situ prepared break junctions did not reveal any superconducting features, providing evidence for a pair-breaking effect at the interface.

Chapter 2

Experimental methods

2.1 Preparation technique

The preparation of single crystalline bulk samples of the heavy fermion compound UNi_2Al_3 [30, 33] poses a major challenge. Due to peritectical decomposition, the preparation from the melt results in the formation of an UAl_2 impurity phase [34], and hence a strongly reduced sample quality. This metallurgical problem can be avoided by molecular beam epitaxy deposition of thin film samples. Furthermore, these samples offer novel possibilities, since they are especially suitable for experiments requiring well defined geometries or surfaces, like transport measurements [35, 36, 37], tunneling spectroscopy [38], optical conductivity [39, 40, 41], etc.

2.1.1 Molecular beam epitaxy

Molecular beam epitaxy (MBE) is one of a number of methods of thin film deposition. In MBE thin films crystallize via reaction between thermal-energy molecular or atomic beams of the constituent elements on the surface of a single crystalline substrate at elevated temperatures in ultrahigh vacuum. The stoichiometric composition of the growing compound can easily be varied by separate evaporation of elementary components with independent rate monitoring and control. Very clean growth conditions and the possibility to control the growth process in situ by surface sensitive diagnostic methods such as reflection high energy electron diffraction (RHEED) or Auger electron spectroscopy (AES) (see e. g. [42, 43]) are main advantages of the MBE technique in comparison to other epitaxial growth methods. For a detailed description of MBE technology see e. g. [44, 45].

An atomic beam of material can be produced by different methods, for example by thermal evaporation of material from an effusion cell or by high frequency heating. The thin films described in this work were prepared by electron beam evaporation. This technique is based on the heat produced by high energy electron beam bombardment of the material to be deposited. The electron beam is generated by an electron gun, which uses the thermal emission of electrons produced by an incandescent filament (cathode). The emitted electrons are accelerated by an anode at high positive potential (kilovolts). A magnetic field is applied to bend the electron trajectory, allowing the cathode to be positioned below the evaporation line. It is possible to obtain a very localized heating of the material and to evaporate it with a high density of evaporation power while the crucible can be cooled. This allows to deposit materials with high melting point and to control the evaporation rate from low to very high values. Measurements of the evaporation rates are usually performed via oscillating crystal monitors by means of measuring resonance frequency, which is reduced with the increasing crystal mass. However, in general the sticking coefficients of evaporated atoms on the oscillating cooled crystal and on the heated substrate are different. Therefore, exact direct measurements of the deposition rates are impossible.

2.1.2   The MBE preparation system

Thin films samples were prepared in a previously installed MBE-system (*Picotorr 450*) manufactured by Varian. The system consists of two connected UHV chambers: An MBE preparation chamber and a transfer chamber, which are separated by gate valves. The transfer chamber has a connection to a sputter chamber, which was constructed for the complete in-vacuo preparation of thin film based tunnel junctions [29].

The transfer chamber is used for mounting and demounting of the substrates and for transferring the samples from the MBE deposition chamber to a junction preparation chamber without breaking the vacuum. It contains two transfer rods with a bayonet like lock system and a carousel for three sample holders. The transfer chamber is pumped by a roughing pump and a turbo molecular pump. This leads to a base pressure of $10^{-8} - 10^{-9}$ mbar.

The junction preparation chamber is based on a CF-160 doublecross connected to the transfer chamber. Employing the MBE transfer system it is possible to transfer the substrate holder onto and from the pivoted sample stage. The dou-
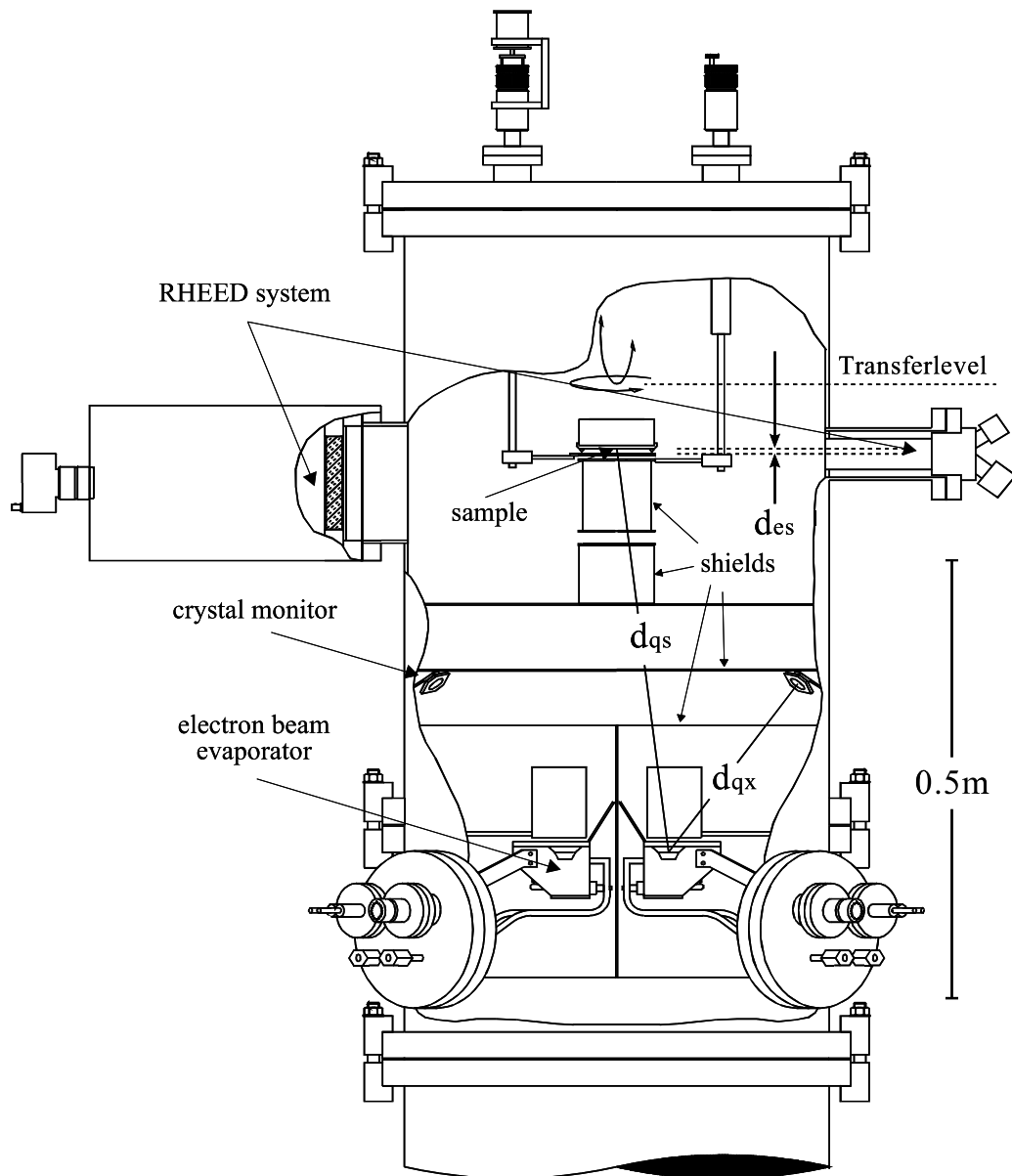
- distance electron beam evaporator – substrate $d_{qs} \approx 53$ cm
- distance electron beam evaporator – quartz monitor $d_{qx} \approx 24$ cm
- $d_{es} \approx 4.8$ mm $\Rightarrow$ incidence angle of electron beam on the film $\varphi \approx 1.15°$

Figure 2.1: Schematic of the components of the MBE preparation chamber. *(Courtesy of M. Huth).*

ble cross is equipped with a home-built magnetron sputtering source [46] allowing sputter deposition either of the barrier material or of the counter electrode. For alternative thermal deposition of the counter electrode a simple evaporator (current heated Wo or Ta boat) is added. Different shadow masks can be moved in front of the substrate. For oxidation or substrate cleaning purpose an oxygen glow discharge can be employed using two Al electrodes. The chamber can be pumped either by the transfer chamber's pumps or separately by a pumping set of a roughing pump and a turbo molecular pump. Its base pressure is 10^{-6} mbar.

The main part of the system is the MBE preparation chamber. It is equipped with three *Leybold ESV4* and one *Leybold ESV6* electron beam evaporators (nominal operating voltage 8 kV), placed in the lower part of the chamber. The evaporators are filled with uranium, aluminum, palladium (*ESV4*) and nickel (*ESV6*), which allows to deposit UNi_2Al_3 and UPd_2Al_3 thin films in the same run without opening the chamber. Two evaporators (*ESV4* for aluminum and palladium) are operated by *Varian* high voltage power supplies with an accelerating voltage limited to maximum 4 kV. With beam current limiting to 500 mA it produces a maximum power of 2 kW. The uranium and nickel evaporators are operated by *Leybold* 8 kV power supplies with a maximum power of 4 kW. The major difference between *ESV4* and *ESV6* evaporators is their design concerning electron beam deflection angle and crucible size. The measurement of the deposition rates is performed by *LeyboldXTC* oscillating quartz crystals. In the upper part of the chamber resides a CAR (Continuous Azimuth Rotation) sample stage with a heating element. It has two degrees of freedom: an azimuthal and a polar rotation axis. Transferring of the substrate holder is performed by a rod manipulator with a bayonet like lock system. During the deposition the crystal growth of the films can be monitored by a RHEED system. It is at the same height as a substrate and consists of an electron gun on one side of the chamber and of a fluorescence screen with a CCD-camera on the opposite side. A schematic of the MBE preparation chamber is shown in Figure 2.1. A detailed description of the MBE system can be found elsewhere [47].

2.2 Characterization methods

The optimization of the preparation process requires a careful characterization of the film samples. Therefore, several different methods were involved for the investigation of the film quality. For in situ characterization during the deposition the

RHEED-system was used. The standard crystallographic analysis was performed by x-ray diffraction in Bragg-Brantano geometry. For detailed structural characterization of the films a four-circle x-ray diffractometer was employed. Energy dispersive x-ray analysis (EDX) was used to estimate the sample stoichiometry. Investigations of the film surface were carried out by an atomic force microscope (AFM) and scanning electron microscope (SEM). A transmission electron microscope (TEM) was used to get direct information about the crystallographic structure of the samples on the atomic scale.

2.2.1 RHEED

Reflection High Energy Electron Diffraction or RHEED is a surface sensitive technique which allows to investigate the properties of the surface of a sample during the growth process. This technique can also be used quantitatively to measure the in-plane surface lattice parameters and in-plane structural coherence length of a sample. The accuracy of the quantitative measurements depends on many parameters (e.g. sample position, incident angle of the electron beam, distance to the screen, quality of the phosphor screen, camera settings etc.) and in practice is often very limited. In this work RHEED was used mostly for a qualitative characterization.

The geometry of RHEED is quite simple (see Figure 2.2). An electron beam (10 keV) is incident on the surface with a glancing angle. The electrons are diffracted by the crystal structure of the sample and then impinge on a phosphor screen mounted opposite to the electron gun. Because of the glancing angle of incidence and the strong interaction of the electron beam and the electronic system of the sample, the penetration depth is limited to a few Å [48]. As only the surface is probed, the sample can be approximated by a two-dimensional layer. The reciprocal lattice then degenerates into a set of one-dimensional rods directed perpendicular to the sample surface. The intersection of the Ewald sphere with every rod produces the diffraction pattern. If a sample is single crystalline and has a flat surface, RHEED patterns consisting of a series of points placed on a half circle are seen. In reality, thermal vibrations and lattice imperfections as well as the energy width of the Ewald sphere cause the reciprocal lattice rods to have a finite thickness. Therefore, even diffraction from a perfectly flat surface results in a diffraction pattern consisting in a series of streaks rather than points. If the sample is not perfectly flat, the electrons will be scattered by islands of different

height resulting in a RHEED pattern constituted by many spotty features. The diffraction from a polycrystalline sample as well as from an amorphous surface gives no diffraction pattern at all, and only a diffuse background will result. Furthermore, RHEED provides information about the flatness of the surface. The pure spotted pattern resulting from transmission of electrons through surface islands shows that the sample surface is rough. For more details about the RHEED technique see, for example, [48].
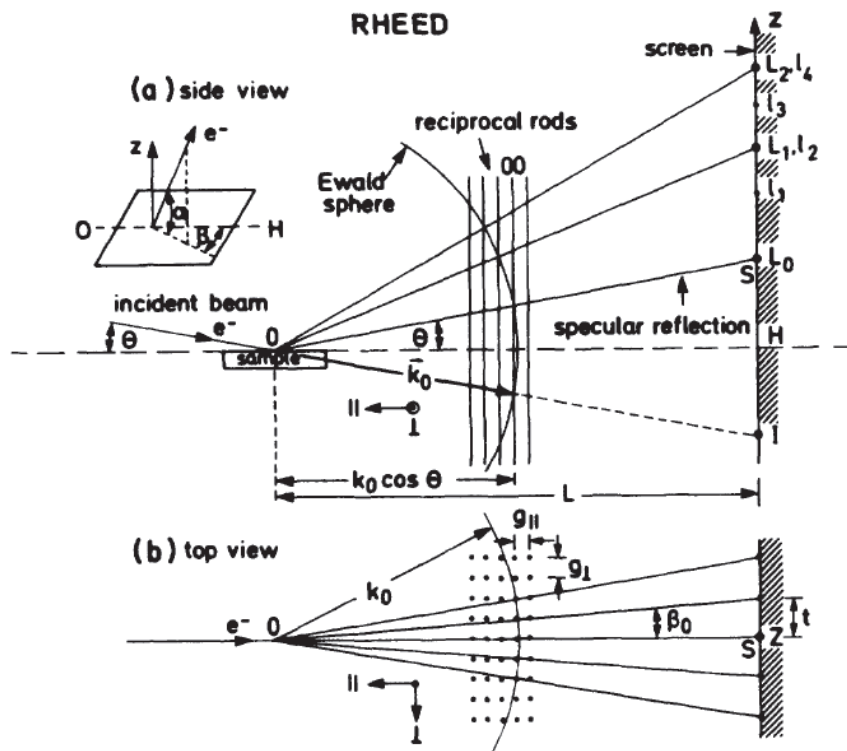
Figure 2.2: Ewald sphere construction and diffraction geometry of RHEED. The maxima of intensity on the screen correspond to projected intersections of the Ewald sphere with the reciprocal lattice. *Adapted from Hernández-Calderon and Höchst* [49].

2.2.2   X-ray diffraction

X-ray diffraction was employed to determinate crystallographic properties of the films [50, 51]. A Philips (X'Pert-MPD) two-circle x-ray diffractometer was used

for the standard characterization of the films. In this diffractometer the samples are measured in Bragg-Brentano geometry employing Cu-K$_\alpha$ radiation. Two measurement procedures ($\omega/2\Theta$-scan and ω-scan of a specular reflection of the film) were performed on almost all samples. By an $\omega/2\Theta$-scan the incident angle $\omega \approx \Theta$ and angle of detector 2Θ are correlated. These angles are varied simultaneously and refractions from the crystal planes perpendicular to the surface normal occur according to Bragg's law

$$\sin\theta = \frac{n \cdot \lambda}{2 \cdot d}$$

at an angle θ given by the diffraction order n, wave length λ, and the distance d between crystal planes of the sample. The $\omega/2\Theta$-scan delivers information about the growth orientation of the films and their crystallographic quality concerning the out-of-plane order and impurities contaminations. For an ω-scan of a specular reflection the detector is fixed at the reflection angle 2Θ, but the incident angle of the beam ω continuously changes. From the width of a this rocking curve of the reflections information about the correlation length and crystal mosaicity can be obtained [52].

The film thickness can be determinated by performing an $\omega/2\Theta$-scan at grazing incident angles (about 0.2º to 5º). At incident angles ω below the critical angle ω_c total external reflection occurs, but for incident angles greater than ω_c ($\omega > \omega_c$) the x-ray beam partly penetrates inside the film. Reflection therefore occurs at the top and the bottom surfaces of the film. The interference between the rays reflected from the top and the bottom of the film surfaces results in interference fringes, the period of which is related to the film thickness. From the Bragg-formula follows approximately for the film thickness d:

$$\frac{2\pi}{d} = \Delta q = \frac{4\pi}{n\lambda}\sin\theta$$

with the refraction order n, wave length λ and refraction angle θ.

For a detailed study of the in-plane orientation and epitaxy of the samples the four-circle geometry is necessary. The employed four-circle diffractometer has a rotating Cu anode manufactured by Nonius and a goniometer from Stoe in Eulerian cradle configuration. The four independent angles are ω, θ, χ and φ (see Figure 2.3). In order to calculate the orientation matrix of the crystal the position of two independent reflections with respect to the goniometer's coordinate system has to be found. Then the orientation matrix is refined by centering on
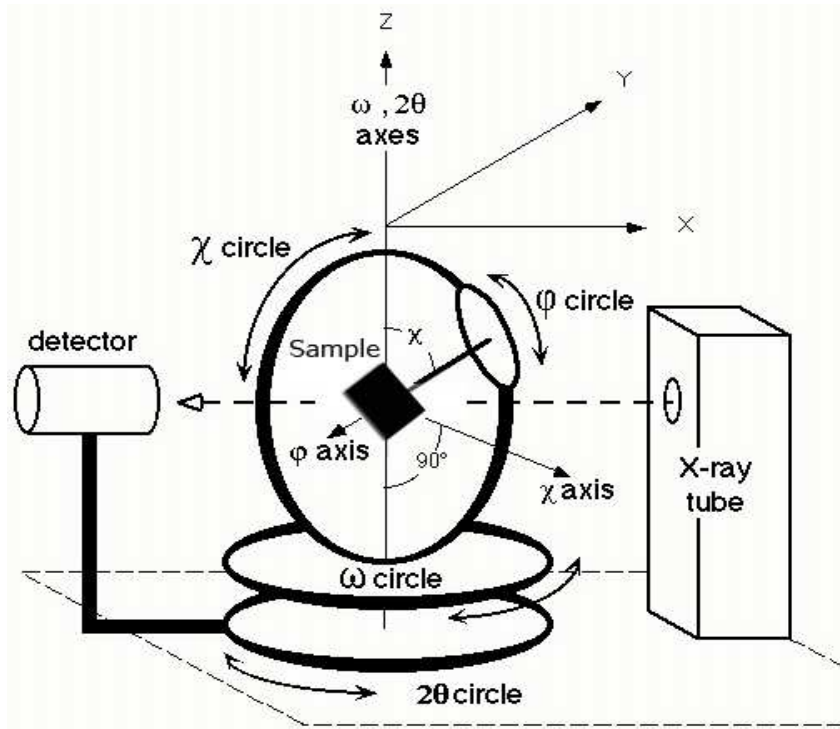
Figure 2.3: Schematic of a four-circle diffractometer.

various calculated reflections. By using the orientation matrix, the position of all other reflection and the lattice parameters of the crystal can be determined. The more reflections are used to refine the orientation matrix the better accuracy is obtained.

The in-plane orientation of the film with respect to the underlying substrate is determinated via φ-scan. In a φ-scan the sample is rotated around the film normal at constant momentum transfer $|\vec{q}|$. As a consequence $\vec{q}$ describes a circle in reciprocal space. If this circle intersects the points of the reciprocal lattice of the crystal, reflection peaks occur at the according φ angles (see Figure 2.4).

A planar sector of reciprocal space can be scanned via a Q-scan. In a Q-scan $\vec{q}$ is varied in a way to describe a planar segment in reciprocal space and all points of the reciprocal lattice in this segment occur as reflections (see Figure 2.5).
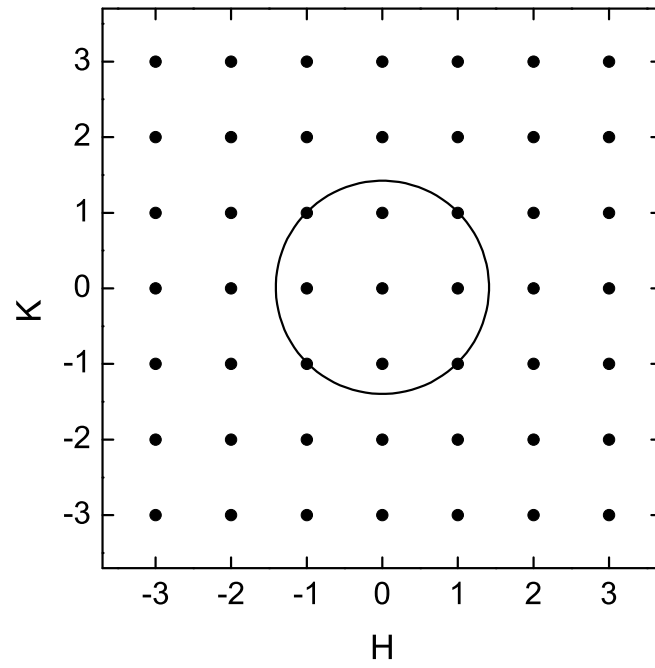
Figure 2.4: Schematic of a φ-scan in a cubic lattice.
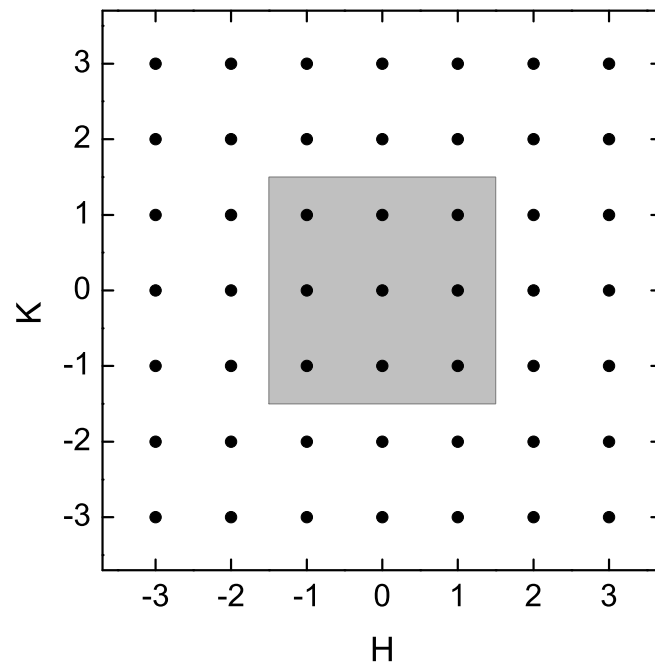
Figure 2.5: Schematic of a Q-scan in a cubic lattice.

Chapter 3

Preparation and characterization of UNi$_2$Al$_3$ thin films

3.1 The preparation process

The high purity source materials were bought from the following manufacturers: aluminum and nickel with purity 99.999% and 99.99% respectively were purchased from Advent Research Materials Ltd, uranium with a purity of 99.9% was purchased from Goodfellow. The substrates were ordered from CrysTec GmbH and Crystal GmbH.

Before the deposition, the substrates were carefully cleaned in an ultrasonic bath by several steps in water, acetone and isopropanol. The cleaned substrates were mounted on the special substrate holder with silver glue. In order to remove the solvent of the silver glue the substrate holder was put in an exsiccator for half an hour. After this the substrate holder was installed on the transfer rod and the transfer chamber was pumped at least for one hour to reach a base pressure of 10^{-7} mbar. After transferring to the MBE chamber the substrates were heated up to 1000 °C in forty-five minutes and annealed at this temperature for another sixty minutes. This procedure was made in order to clean the substrate surface from contaminations. After the annealing process the substrates were cooled to the deposition temperature within five minutes.

The elementary components uranium, aluminum and nickel were evaporated out of three parallelly operated and independently controlled electron beam evaporators. For U and Ni graphite liners were used, Al was evaporated from Al$_2$O$_3$ or boron nitride liners. The evaporation rate of each material was independently

monitored by oscillating quartz crystals. The real ratios of the rates were adjusted by setting the density of the evaporated material in the control units of the quartz monitors. This method allows a precise adjustment of the nominal film composition.

The substrate temperature was monitored by a thermo element installed in the sample stage. A temperature controller regulated the current through the radiation heating element and kept a constant temperature ($\pm 1\,\mathrm{K}$) of the sample holder. The real temperature at the substrate surface was measured by a pyrometer. Because of the very low emissivity of the substrate in the infrared range the emissivity coefficient of polished stainless steel ($\epsilon = 0.35$) was used.

The pressure in the chamber during deposition is another very important parameter. Films deposited at a pressure higher than $6 \cdot 10^{-6}\,\mathrm{mbar}$ have never been of good quality. That can be explained by the higher rate of the oxidation process (first of all for U) compared to absorption processes at the film surface. Normally the pressure of the system rises from $\approx 10^{-8}\,\mathrm{mbar}$ up to $\approx 10^{-6}\,\mathrm{mbar}$ at the beginning of deposition mainly due to thermal evaporation of the materials but also because of increasing the temperature of the chamber parts by heat radiation.

3.2   Substrates

The first series of UNi$_2$Al$_3$ thin films was prepared by M. Jourdan in the scope of his Diploma thesis [53]. These films were deposited on three different types of substrates: Al$_2$O$_3$ randomly oriented, Al$_2$O$_3$(110) and LaAlO$_3$(111). UPd$_2$Al$_3$, which is isostructural to UNi$_2$Al$_3$, grows epitaxially on LaAlO$_3$(111) with its crystallographic (001)-axis oriented perpendicular to the film surface. Although the *a*-axis of UNi$_2$Al$_3$ is about 3% shorter than the *a*-axis of UPd$_2$Al$_3$, it was expected that UNi$_2$Al$_3$ would grow epitaxially on the same substrate with similar deposition parameters. However, the x-ray analysis of the UNi$_2$Al$_3$ films on LaAlO$_3$(111) showed only a weak UNi$_2$Al$_3$ phase, which was induced by the substrate in (001)-direction, and a strong impurity phase of AlNi. A variation of the deposition parameters did not improve the quality of the films on these substrates.

To determine the natural growth direction of UNi$_2$Al$_3$, films were prepared on non epitaxial Al$_2$O$_3$ substrates. It was found, that hexagonal UNi$_2$Al$_3$ has a clear tendency for (100)-oriented growth (*ac*-plane parallel to the film surface) in contrast to UPd$_2$Al$_3$, which prefers (001) orientation even on the non epitaxial

UNi$_2$Al$_3$(100) on Al$_2$O$_3$ (110)

UNi$_2$Al$_3$(100) on MgAl$_2$O$_4$ (100)

UNi$_2$Al$_3$(100) on YAlO$_3$ (112) and YAlO$_3$(010)
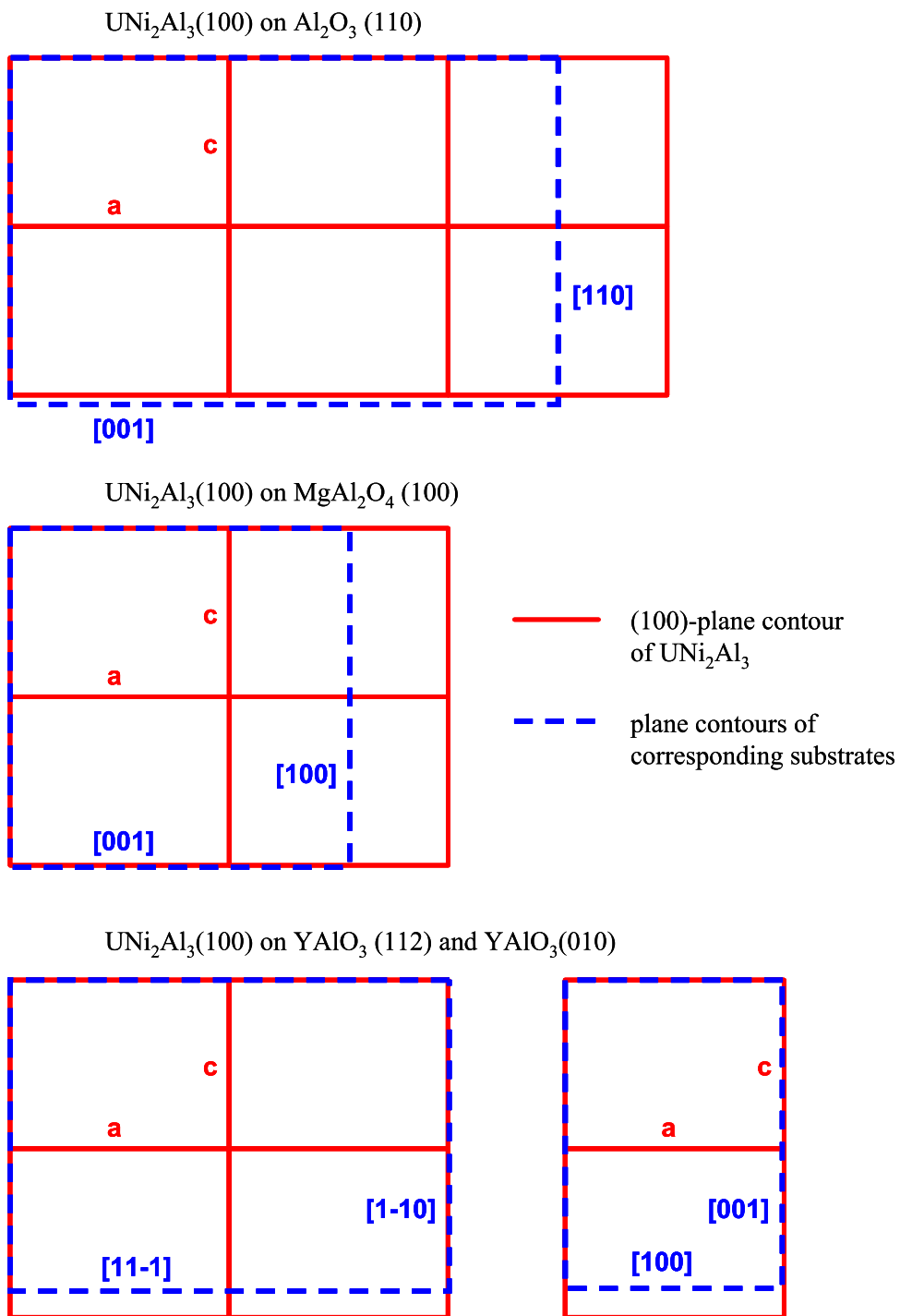
Figure 3.1: Orientation of UNi$_2$Al$_3$ thin films with respect to the substrates.

substrates. However, previously no epitaxial UNi$_2$Al$_3$ films could be prepared.

In the frame of this work four different substrate types were tested for providing epitaxial growth of (100)-oriented UNi$_2$Al$_3$ thin films. These substrates are hexagonal Al$_2$O$_3$ (space group R$\bar{3}$c, lattice parameters: a=0.477 nm, c=1.304 nm) cut in (110)-direction, cubic MgAl$_2$O$_4$ (space group F43m, lattice parameter a=0.8083 nm) cut in (100)-direction, and orthorhombic YAlO$_3$ (space group P63/mmc, lattice parameters: a=0.517 nm, b=0.5307 nm, c=0.7355 nm) cut in (010)- and (112)-directions. Possible in-plane orientations of (100)-oriented UNi$_2$Al$_3$ films on the substrates and corresponding lattice misfits of these are shown in Figure 3.1 and in Table 3.1, respectively.

Substrate type	Misfit for the a axis	Misfit for the c axis
Al$_2$O$_3$(110)	(1×3) +16.7%	(1×2) −2.8%
MgAl$_2$O$_4$(100)	(2×3) −3.4%	(1×2) −0.6%
YAlO$_3$(010)	(1×2) +0.7%	(1×2) +8.5%
YAlO$_3$(112)	(1×1) −0.5%	(1×2) +7.9%

Table 3.1:   Mismatchs of the substrates for the a and b axis of UNi$_2$Al$_3$ are calculated as $(N \cdot axis_{UNi_2Al_3} - M \cdot axis_{substrate})/N \cdot axis_{UNi_2Al_3}$.   Thus, for example for Al$_2$O$_3$(110), one obtaines a lattice mismatch of $(3 \cdot [100]_{UNi_2Al_3} - [110]_{Al_2O_3})/3 \cdot [100]_{UNi_2Al_3}$ for the tripled a axis of UNi$_2$Al$_3$ ((M×N)=(1×3)), and $(2 \cdot [001]_{UNi_2Al_3} - [001]_{Al_2O_3})/2 \cdot [001]_{UNi_2Al_3}$ for the doubled c axis ((M×N)=(1×2)).

For a given substrate type the optimal deposition parameters can be found by a systematical variation of the substrate temperature and the evaporation rates of the materials and further investigation of the film quality by means of structural characterization and transport measurements.

3.3   UNi$_2$Al$_3$ thin films on Al$_2$O$_3$ and MgAl$_2$O$_4$ substrates

From the employed substrates, sapphire provides the largest lattice mismatch between the (100)-plane of UNi$_2$Al$_3$ and a corresponding crystallographic plane of the substrate (see Figure 3.1, Table 3.1). Nevertheless, x-ray diffraction in Bragg-Brentano geometry of the films on Al$_2$O$_3$(110) reveals (100)-oriented growth of UNi$_2$Al$_3$ (Figure 3.2), but strong impurity phases consisting of UAl$_2$, UNiAl, and
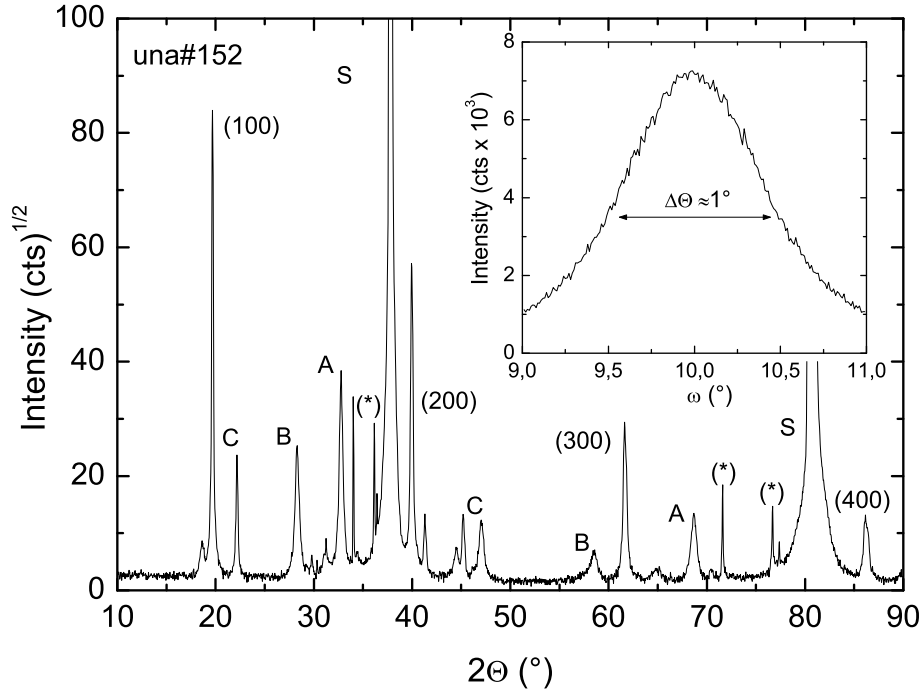
Figure 3.2: XRD $\omega/2\Theta$-scan of a UNi$_2$Al$_3$ film on Al$_2$O$_3$(110). The diffraction peaks of UNi$_2$Al$_3$ are labelled (ℓ00), the substrate peaks (S) and the substrate peaks caused by Wo-L radiation (*). The impurity phases are A: UAl$_2$, B: UO$_x$, C: UNiAl. The inset shows a rocking curve measured at the (100) peak.

UO$_x$ are present. SEM investigations (Figure 3.3) suggest that these impurities are accumulated in segregations. This leads to the formation of a rough surface and, as a consequence, to a poor RHEED diffraction pattern which is observed for all UNi$_2$Al$_3$ thin films on Al$_2$O$_3$(110). The ω-scan of the (100)-peak, shown in the inset of Figure 3.2, indicates a rocking curve full width at half maximum (FWHM) of 1° - the average value of the rocking curve width for the UNi$_2$Al$_3$ thin films on Al$_2$O$_3$(110). The dominant contribution to the peak width is obtained from crystal mosaicity, generated probably due to a large lattice misfit between substrate and film at the interface.

Despite the large lattice misfit of the substrate, the UNi$_2$Al$_3$ thin films on Al$_2$O$_3$(110) are in-plane ordered. This can be conclude from the φ-scan of an UNi$_2$Al$_3$ film which is presented in the upper panel of Figure 3.4. The scan shows the (10$\bar{1}$) and equivalent (101) reflections of UNi$_2$Al$_3$, i.e. combinations of in-plane (001) and out-of-plane (100) vectors (in a hexagonal crystal (001) $\|$ [001]).
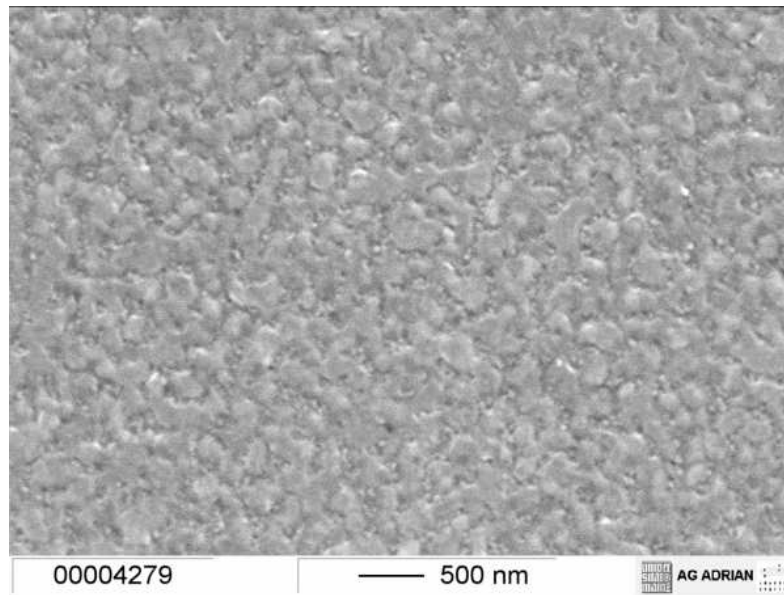
Figure 3.3: SEM image of a UNi$_2$Al$_3$ thin film on Al$_2$O$_3$(110) some hours after deposition.
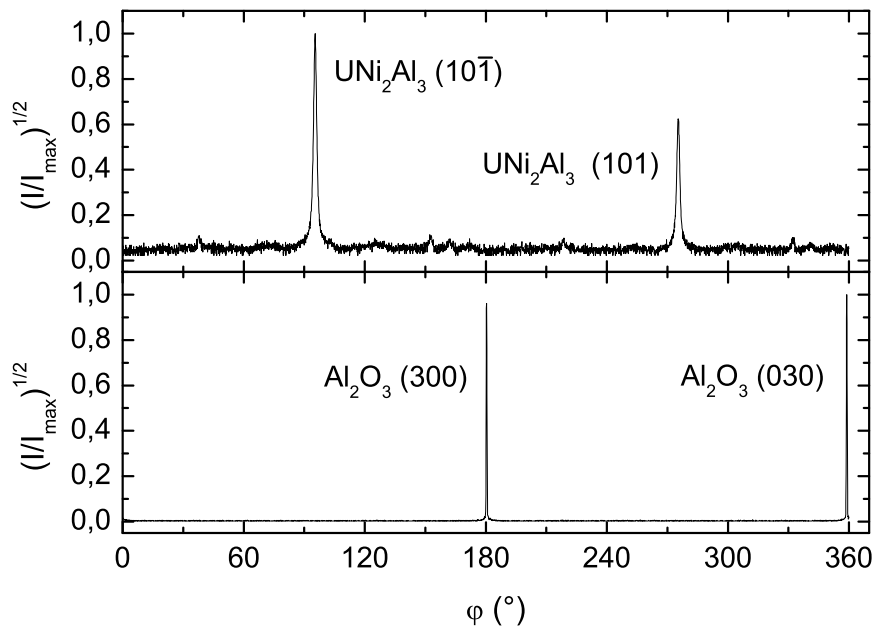
Figure 3.4: Upper panel: φ-scan of (10$\bar{1}$) and equivalent (101) reflections of UNi$_2$Al$_3$ thin film on Al$_2$O$_3$(110). Lower panel: φ-scan of the (300) and equivalent (030) reflections of the underlying Al$_2$O$_3$ substrate.

In the lower panel of Figure 3.4 the φ-scan of the underlying Al$_2$O$_3$(110) substrate is shown. The scanned (300) and equivalent (030) peaks are combinations of the in-plane ($\bar{1}$10) and out-of-plane (110) vectors of sapphire (in a hexagonal crystal ($\bar{1}$10) $\|$ [1$\bar{1}$0]). Comparing the positions of the thin film peaks with the positions of the substrate peaks and noticing that in hexagonal crystals (001) $\|$ [001] and ($\bar{1}$10) $\|$ [1$\bar{1}$0] it can be concluded that UNi$_2$Al$_3$(100) growth with its [001] axis aligned along the [001] axis of Al$_2$O$_3$.

Further investigation of the sample purity were performed by resistivity measurements. Figure 3.5 shows the $R(T)$ dependence of ordered UNi$_2$Al$_3$ thin film on Al$_2$O$_3$(110). The typical $R(T)$ behavior (known from the measurements performed on bulk samples) with a relatively large residual resistance ratio up to $RRR = R(300\,\mathrm{K})/R(2\,\mathrm{K}) \approx 7$ ($RRR \simeq 30$ in best bulk single crystals [31]) is observed. At low temperatures the $R(T)$ dependence indicates an onset of superconductivity which is shown in the inset of Figure 3.5. The onset vanishes at an external magnetic field of $\mu_0 H \approx 1\,\mathrm{T}$ proving its superconducting character. However, a full superconducting transition has never been observed for
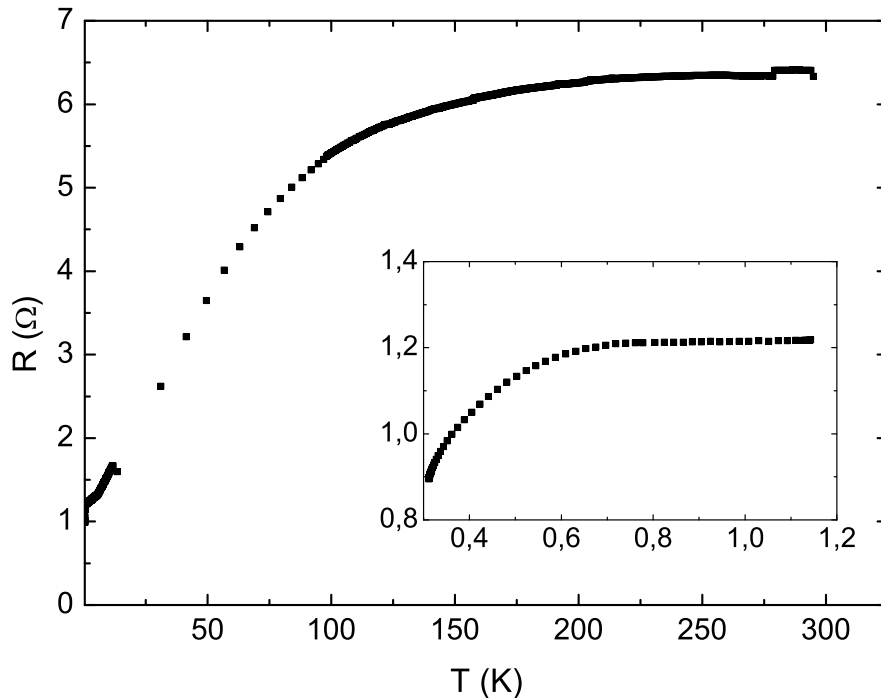
Figure 3.5: R(T) dependence of a UNi$_2$Al$_3$ thin film on Al$_2$O$_3$(110). The inset shows the superconducting onset at low temperatures.
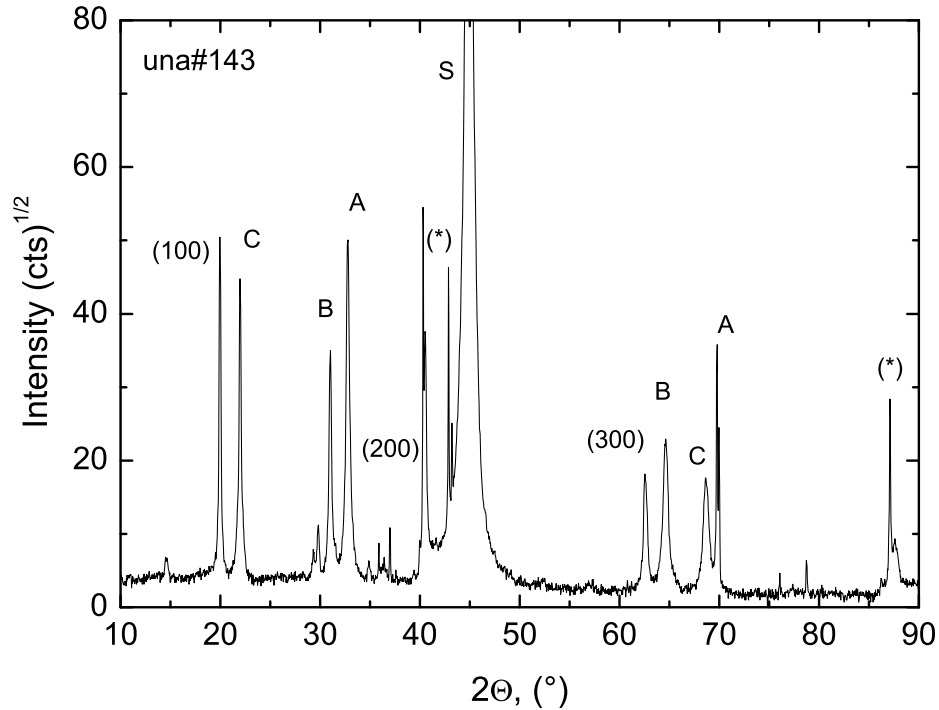
Figure 3.6: XRD $\omega/2\Theta$-scan of a UNi$_2$Al$_3$ film on MgAl$_2$O$_4$(100). The diffraction peaks of UNi$_2$Al$_3$ are labelled (ℓ00), the substrate peaks (S) and the substrate peaks caused by Wo-L radiation (*). The impurity phases are A: UAl$_2$, B: UO$_x$, C: UNiAl.

films on Al$_2$O$_3$(110). A variation of substrate temperature and evaporation rates of the elementary components did not improve the quality of the films on these substrates. The pronounced impurity phases could not be avoided.

A cubic MgAl$_2$O$_4$ substrate cut in (100)-direction has one crystallographic axis with a length similar to the doubled length of the in-plane [001]-axis of UNi$_2$Al$_3$(100) (see Figure 3.1 and Table 3.1). Although the lattice misfit of both in-plane axes is smaller than in the case of an Al$_2$O$_3$(110) substrate, the crystallographic quality of the UNi$_2$Al$_3$ films obtained on MgAl$_2$O$_4$(100) is even worse compared to films on sapphire. The formation of the pronounced impurity phases of UAl$_2$, UNiAl, and UO$_x$ on MgAl$_2$O$_4$(100) substrates could not be avoided by a variation of the deposition parameters. The films are textured but show no in-plane orientation. The resistivity measurements indicate poor residual resistance ratios $RRR \approx 1$. No indication of superconductivity was observed.

3.4 Epitaxial UNi$_2$Al$_3$(100) thin films on YAlO$_3$ substrates

In order to obtain epitaxial growth, thin films were prepared on orthorhombic YAlO$_3$ cut in (010)- or (112)-direction. Both substrates have one in-plane axis with a length similar to the in-plane [010] axis of UNi$_2$Al$_3$(100) (see Figure 3.1 and Table 3.1). In situ monitoring by RHEED during deposition and x-ray analysis already of the first films prepared on YAlO$_3$ indicated a strong phase of ordered UNi$_2$Al$_3$(100) revealing good preconditions for epitaxial growth on both types of substrates. During the film quality optimization process thin films with thicknesses d between 20 nm and 200 nm were deposited. The deposition parameters were found by a systematical variation of the substrate temperature and the evaporation rates and further investigations of the film quality by means of structural characterization and transport measurements. High purity single crystalline thin films of UNi$_2$Al$_3$(100) were obtained on both types of substrates.

The optimized deposition parameters for epitaxial growth of UNi$_2$Al$_3$(100) thin films on YAlO$_3$ substrates are:

- Substrate temperature (pyrometer, $\epsilon = 0.35$) $T^{pyro}_{\epsilon=0.35} = 730^{o}C$.

- Effective evaporation rate U (at monitor) $\rho_U = 0.058\,\text{nm/s}$.

- Effective evaporation rate Ni (at monitor) $\rho_{Ni} = 0.080\,\text{nm/s}$.

- Effective evaporation rate Al (at monitor) $\rho_{Al} = 0.198\,\text{nm/s}$.

- Effective growth rate of the film amounted to $\rho_{tot} = 0.06\,\text{nm/s}$

These evaporation rates correspond to a ratio of the numbers of the impinging atoms of $\dot{n_U} : \dot{n_{Ni}} : \dot{n_{Al}} = 1 : 2.62 : 4.33$. The ratio at the monitor differs from the exact stoichiometric ratio of $\dot{n_U} : \dot{n_{Ni}} : \dot{n_{Al}} = 1 : 2 : 3$ due to difference of sticking coefficients of oscillating quartz crystals and substrate. The probability of reevaporation of the impinging atoms from the hot substrate surface is higher than from the surface of the quartz monitor due to temperature difference and different absorption conditions. Thus, the exact calculation of the film atomic ratio from the experimentally measured evaporation rates at the monitor is not possible.

3.4.1   Crystallographic properties

UNi$_2$Al$_3$ thin films grow epitaxially on YAlO$_3$(010) and YAlO$_3$(112) substrates
as can be proved by x-ray diffraction as well as by in situ RHEED. The crystal-
lographic (100)-axis of the films is oriented perpendicular to the substrate sur-
face. In Figure 3.7 x-ray scans in Bragg-Brentano geometry of UNi$_2$Al$_3$ films on
YAlO$_3$(010) and on YAlO$_3$(112) substrates are shown. On both scans only (h00)
reflections can be seen together with substrate peaks and some minor impurity
phases (presumably UO$_x$). ω-scans of the (100)-reflection of different films reveal
a full width at half maximum (FWHM) of the rocking curves in the range of
0.2° - 0.7°, pointing out a low mosaicity of the structure (inset of Figure 3.7). The
rocking curve width is independent of the diffraction order (h00) for a given film
and thus is not determined by a lateral correlation length effect but by crystal
mosaicity (see subsection 3.4.2).

The in-plane order of the films was studied by x-ray analysis in a four-circle
diffractometer. In Figure 3.8 a two-dimensional Q-scan of the reciprocal (1kl)
plane of UNi$_2$Al$_3$ is shown. From the observation of reflections at integer k and
l values the in-plane order of the film is obvious.

An in situ characterization by RHEED supplements the x-ray data. For both
substrate types the typical RHEED diffraction patterns of an in-plane ordered
surface are visible during the whole deposition process (Figure 3.9). Moreover,
RHEED shows, that the in-plane axis of UNi$_2$Al$_3$ crystals are aligned parallel
to the substrate in-plane axis. This is clear evidence for epitaxial growth with
substrate induced order.

In Figure 3.10 a TEM image of an UNi$_2$Al$_3$ film is shown. In this case, the
electron beam was directed along the real space b axis of UNi$_2$Al$_3$. The prominent
lattice rows reveal the atomic distances which fit to the distances of the UNi$_2$Al$_3$
(100) and (001) planes, proving again in-plane and out-of-plane order and purity
of the sample.

Further information about the epitaxial relations were obtained by x-ray φ-
scans. In Figure 3.11 φ-scans of selected UNi$_2$Al$_3$ and YAlO$_3$ reflections are pre-
sented. The scan in the upper panel shows the (10$\bar{1}$) and equivalent (101) peak
of UNi$_2$Al$_3$, i. e. combinations of in-plane (001) and out-of-plane (100) vec-
tors. In the lower panel of Figure 3.11 a φ-scan of the YAlO$_3$(112) substrate is
shown. The scanned (202) and (022) peaks are combinations of in-plane (1$\bar{1}$0)
and out-of-plane (112) vectors of YAlO$_3$. Due to the specific crystal structure of
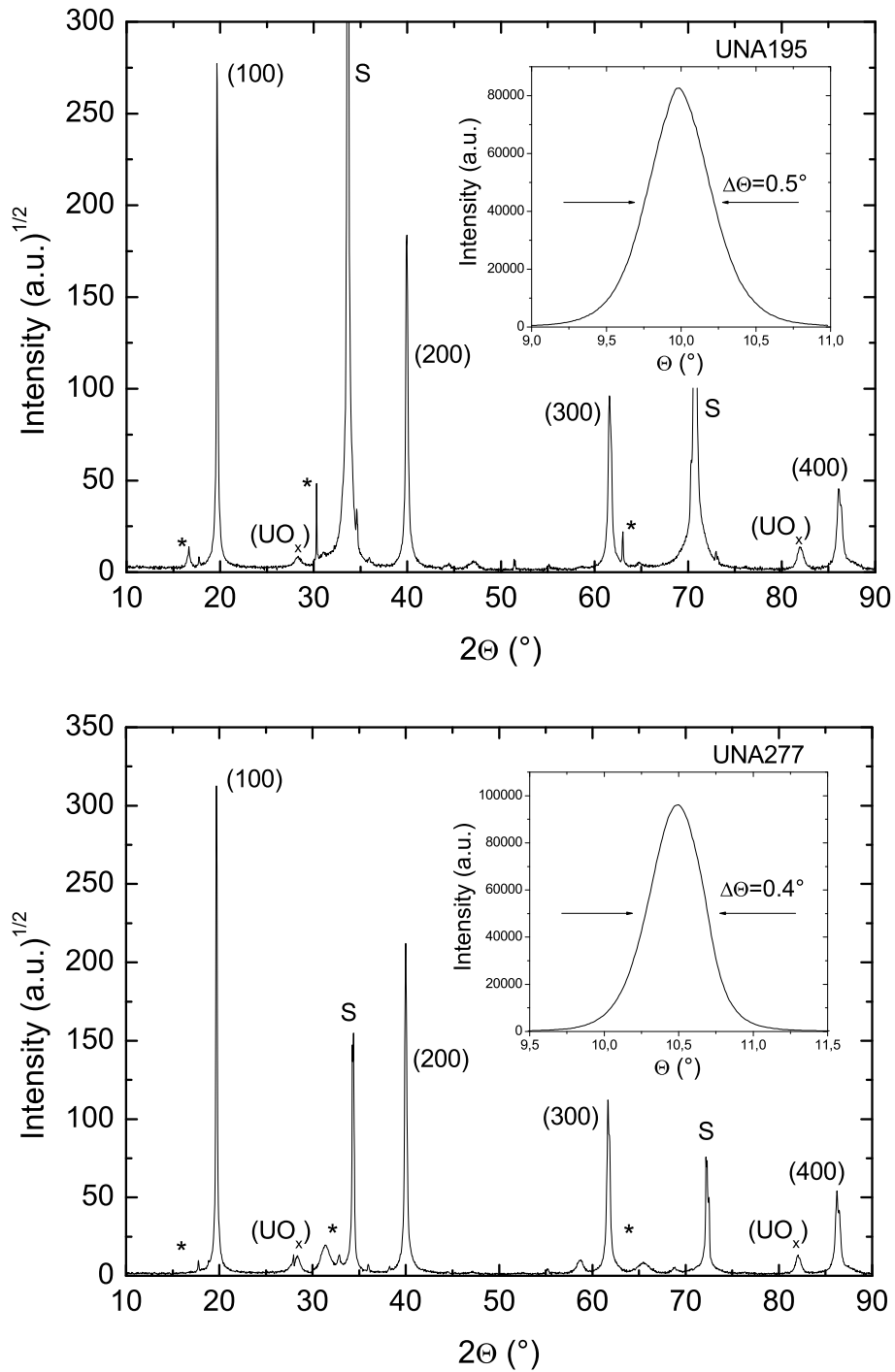
Figure 3.7: X-ray $\theta/2\theta$-scans of UNi₂Al₃ films on YAlO₃(010)(upper panel) and on YAlO₃(112)(lower panel). S: substrate, X: UO$_x$, *: peaks caused by Wo-L radiation . Insets: ω-scans of the (100)-reflection.
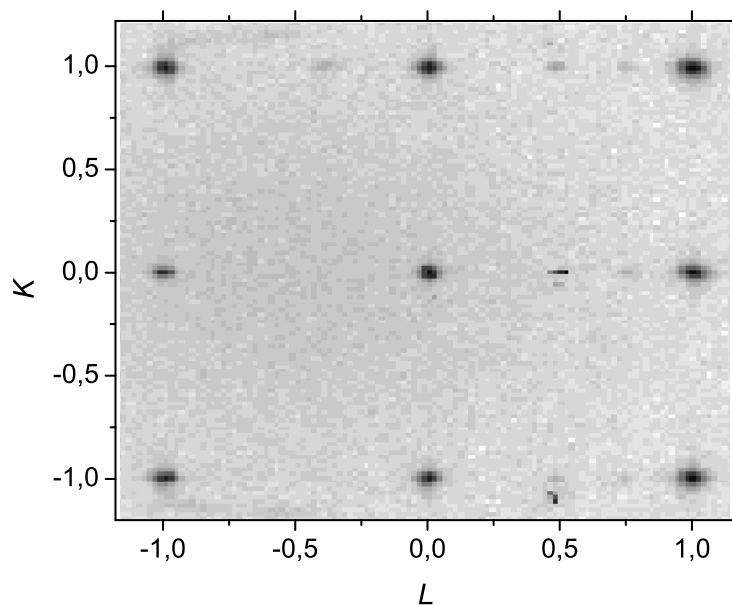
Figure 3.8: Q-scan of the reciprocal ($1kl$)-plane of UNi$_2$Al$_3$. The x-ray intensity (linear gray scale) is plotted versus the momentum transfer in units of the reciprocal lattice vectors. The narrow reflections close to $(1\,\frac{1}{2}\,\bar{1})$ and $(1\,\frac{1}{2}\,0)$ are substrate reflections.
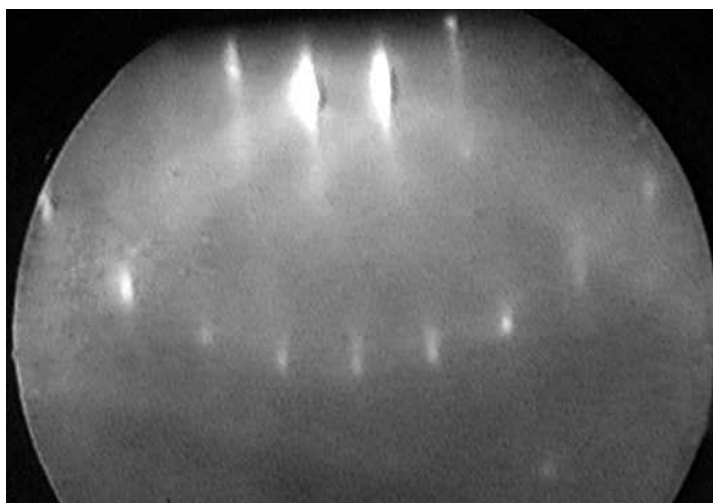
Figure 3.9: RHEED-pattern of an UNi$_2$Al$_3$ film on YAlO$_3$(010). Electron-beam directed along c-axis (typical diffraction pattern of an in plane ordered surface).
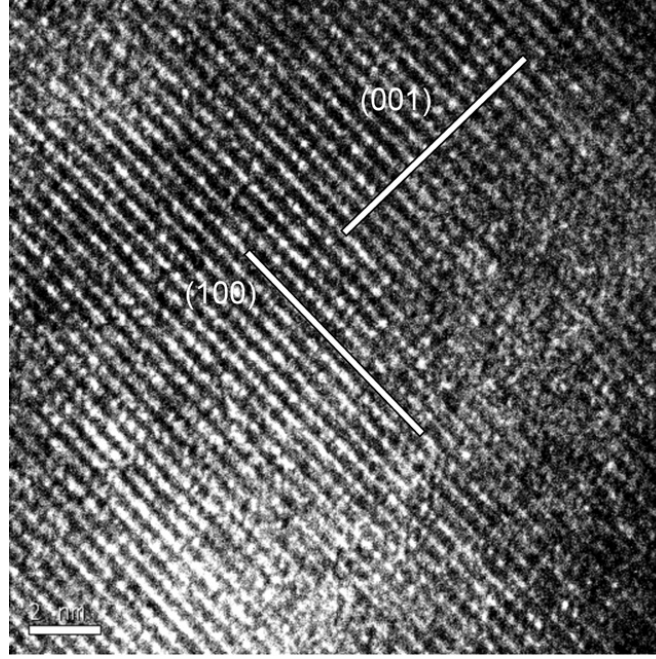
Figure 3.10: TEM image of UNi$_2$Al$_3$ thin film. The electron beam is directed along the real space b axis of UNi$_2$Al$_3$. The lattice rows correspond to the (100) and (001) planes of the UNi$_2$Al$_3$ crystal.

the substrate the reciprocal $(1\bar{1}0)$ direction is almost parallel to the real space $[1\bar{1}0]$ direction. Thus from the observation that the thin film peaks of the upper panel are observed at the same φ-angles as the substrate peaks of the lower panel it can be concluded that UNi$_2$Al$_3$(100) growth with its [001] axis aligned parallel to the $[1\bar{1}0]$ axis of YAlO$_3$. Consequently, the epitaxial relations for UNi$_2$Al$_3$ thin films on YAlO$_3$(112) are established to be

$$(112)_{YAlO_3}||(100)_{UNi_2Al_3}$$

$$[11\bar{1}]_{YAlO_3}||[010]_{UNi_2Al_3}$$

$$[1\bar{1}0]_{YAlO_3}||[001]_{UNi_2Al_3}$$

Similar measurements were performed for UNi$_2$Al$_3$ films on YAlO$_3$(010) substrate. The following epitaxial relations were found:

$$(010)_{YAlO_3}||(100)_{UNi_2Al_3}$$

$$[100]_{YAlO_3}||[010]_{UNi_2Al_3}$$
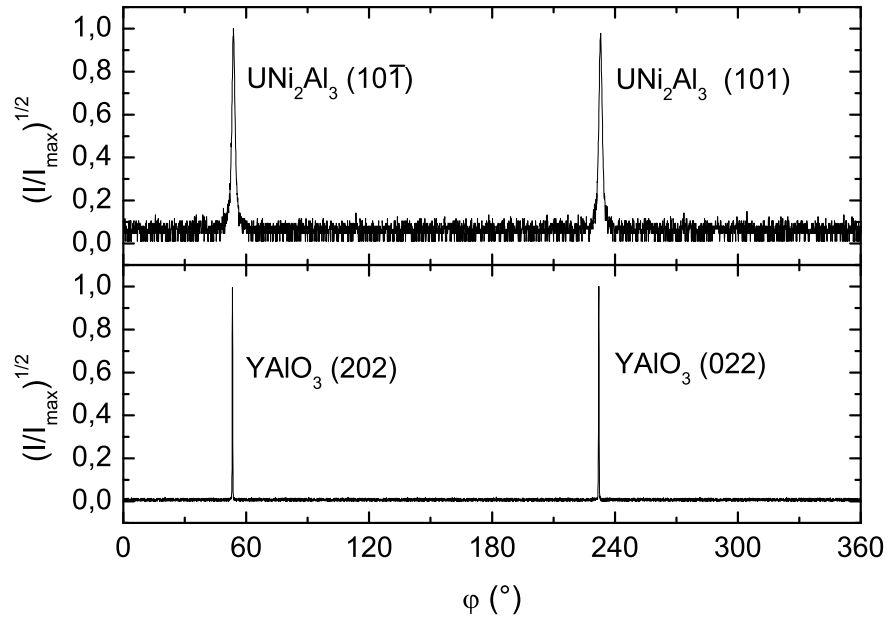
Figure 3.11: Upper panel: φ-scan of (10$\bar{1}$) and equivalent (101) reflections of UNi$_2$Al$_3$ thin film on YAlO$_3$(112). Lower panel: φ-scan of the (202) and equivalent (022) reflections of the underlying YAlO$_3$(112) substrate.

$$[001]_{YAlO_3}||[001]_{UNi_2Al_3}$$

The lattice parameters of the UNi$_2$Al$_3$ film calculated from the positions of 16 x-ray reflections ($a = 0.5211(5)$ nm, $b = 0.5221(8)$ nm, $c = 0.4017(2)$ nm) are in agreement with the values obtained from polycrystalline bulk samples [9] and rule out any growth process induced stress in the bulk of the films.

3.4.2   Morphology

An AFM was used to investigate the topography of the films. An island morphology which is typical for metallic thin films on insulating substrates is observed (Figure 3.12). In contrast to UPd$_2$Al$_3$ thin films on LaAlO$_3$(111) substrates, which show almost square-shaped islands with a regular size [29], the UNi$_2$Al$_3$ films on YAlO$_3$ have rougher surface with the rounded shape of the islands . This dissimilarity in surface formation could be due to the different growth direction of UNi$_2$Al$_3$.

In Figure 3.13 the AFM images of two films with thicknesses 100 nm and 150 nm are shown. The form and size of the islands of both films are very similar.

The smallest islands have a diameter of about 100 nm and a height of about 10 nm. The largest islands can reach a diameter of 500 nm and a height of 70 nm. For the film with a thickness of 150 nm the general features of the morphology are almost identical.
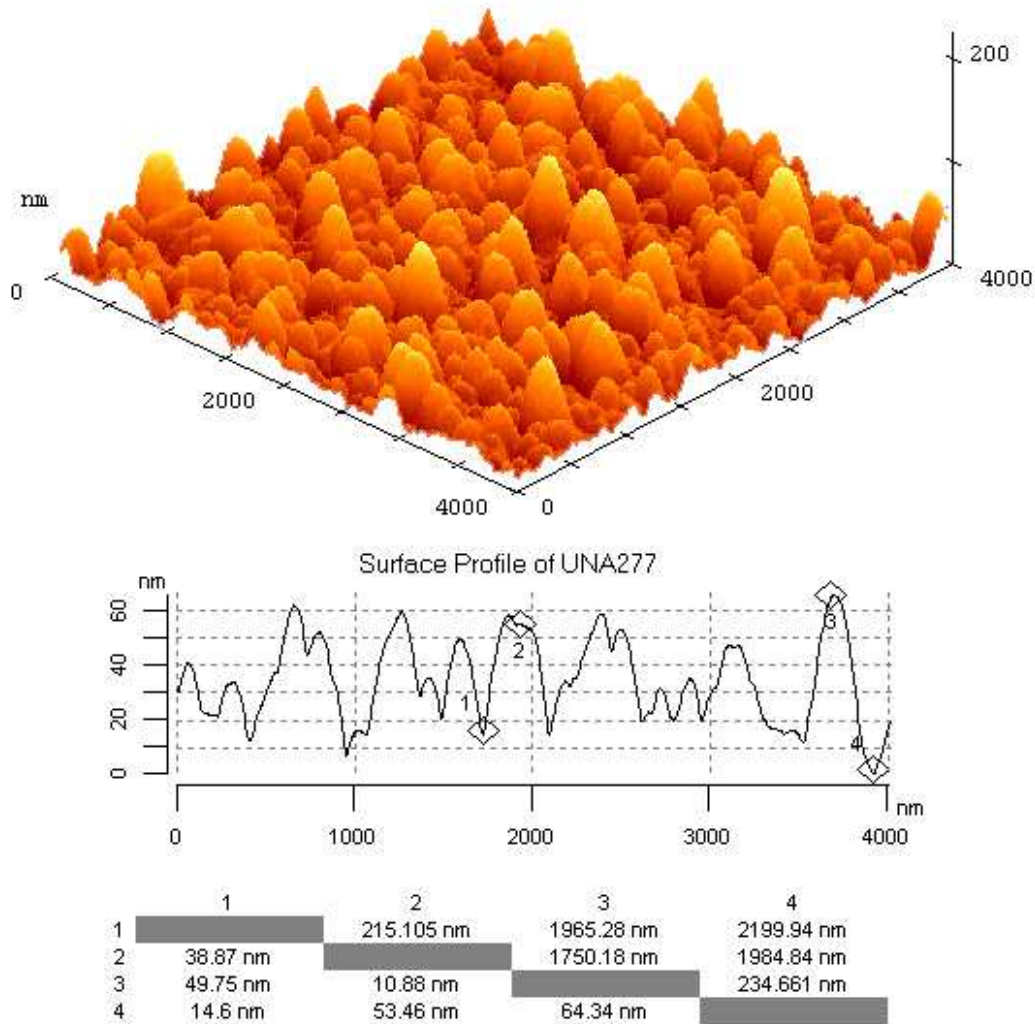
Figure 3.12: The upper panel shows an AFM image of the surface of a UNi$_2$Al$_3$ thin film (thickness $d = 150$ nm) some hours after deposition. The lower panel shows a line scan height profile of this image.
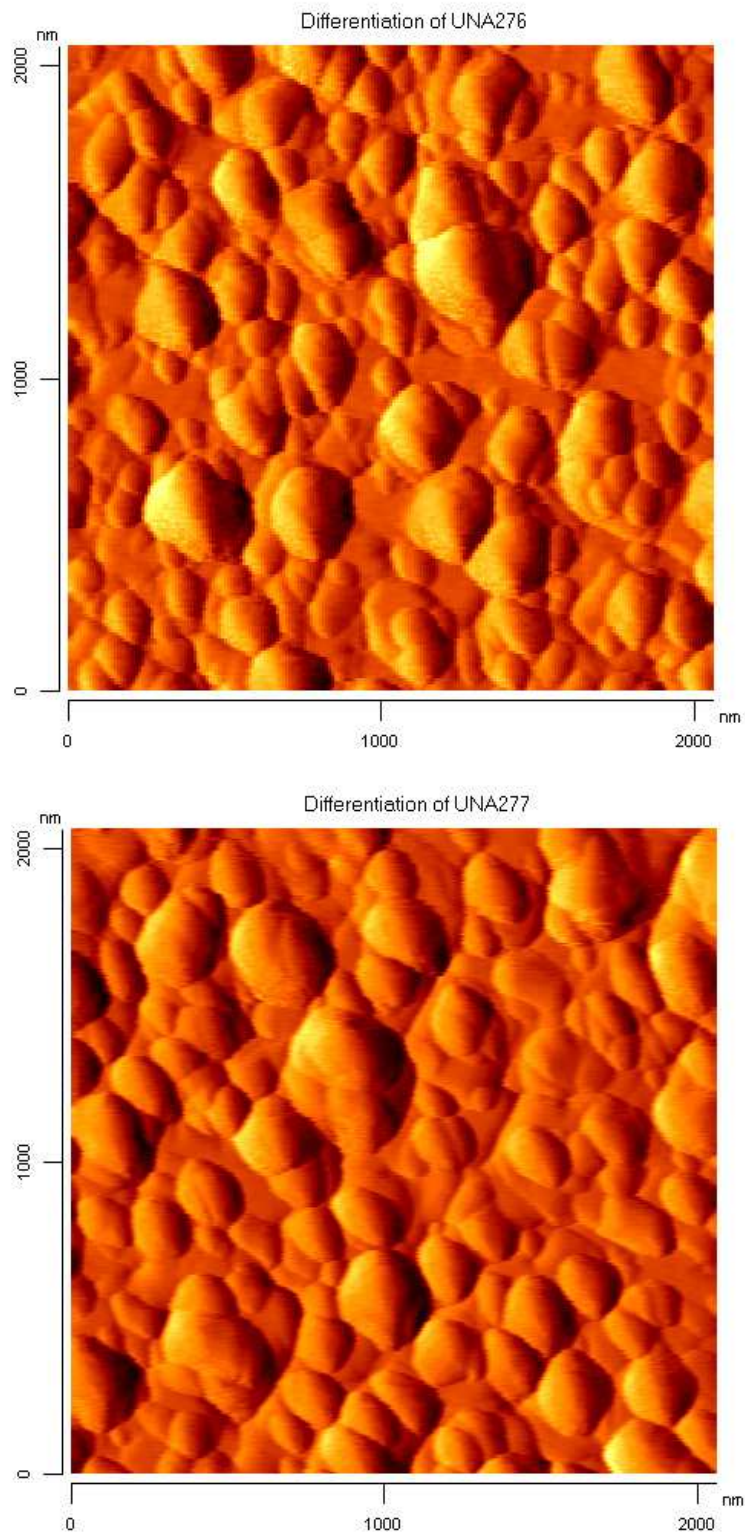
Figure 3.13: AFM images of UNi$_2$Al$_3$ thin films of different thicknesses. Upper panel $d = 100$ nm, lower panel $d = 150$ nm.

Chapter 4

Magnetic order

UNi_2Al_3 as well as the isostructural UPd_2Al_3 both belong to the heavy fermion superconductors which exhibit the coexistence of superconductivity and magnetic order at low temperatures. However, their superconducting and magnetic properties are quite different. Whereas for UPd_2Al_3 there is evidence for a magnetic Cooper-pairing interaction [17, 15, 18], the mechanism of superconductivity in UNi_2Al_3 remains open. Since a different unconventional superconducting pairing mechanism may be realized in UNi_2Al_3, the magnetic properties are crucial to an understanding of the origin of superconductivity.

4.1 Resonant magnetic x-ray scattering

It is well known that x-rays are sensitive to charge distribution. But additionally to the charge scattering the magnetic component of the x-rays also interacts with the magnetic moments which gives rise to magnetic scattering [54]. However, the first experimental observation of magnetic x-ray scattering [55] was not possible for a long time due to the fact that the magnetic scattering cross section is very small. By scattering on a single electron with typical x-ray energies of 10keV it is reduced by factor of 10^{-4} compared to the charge scattering cross section. By scattering on an atom, the magnetic scattering cross section is further reduced as compared to charge scattering, because only unpaired electrons take part in the magnetic scattering process. Therefore, the intensity of magnetic scattering far from the resonance is typically 10^5 to 10^6 times smaller than the charge scattering intensity [56]. The investigation of magnetic structures by x-ray diffraction became possible by employing synchrotron radiation sources which provide high

photon flux. The intensity of the magnetic scattering can be increased by tuning the phonon energy near an absorption threshhold. This method is called *resonant magnetic x-ray scattering*. The resonance is expected when the x-ray energy is tuned to an electric multipole transition of the magnetic ion [57]. An enhancement of the magnetic scattering signal occurs if there is a difference in the cross section for electrons with different $\vec{l}$ and $\vec{s}$. In the case of $4f$ or $5f$ elements the most obvious reason for this difference is the magnetic polarization of the partially filled states into which the core electron is exited. Different probabilities for transitions to the states with the opposite polarization lead to a magnetic contrast in the scattering cross section. Thus, for lanthanides and actinides a resonant enhancement of the magnetic scattering signal can be expected at the M_{IV} and M_V absorption threshholds due to the resonant contribution of the electric dipole transition E1.

On account of the small sample volume, x-ray resonant magnetic scattering is the experimental method of choice to investigate the microscopic magnetic properties of UNi_2Al_3 thin films.

4.2   Experiments on UNi_2Al_3 thin films

The experiments were performed at the XMaS-CRG beamline (BM28) of the European Synchrotron Radiation Facility (ESRF) in Grenoble, France. The main goal of the experiment was to gain detailed knowledge of the magnetic structure and the magnetic ordering transition of UNi_2Al_3 thin film samples and to compare it to single crystal data.

The measurements were performed in σ-π geometry [58] with the photon energy tuned to the uranium M_4 absorption edge (E$\simeq$ 3.73keV). At low temperatures magnetic scattering has been observed at $(2, 0.39, \frac{1}{2})$ (see inset of Fig. 4.2) and with reduced intensity at $(1, 1.39, \frac{1}{2})$ proving that there is spatial magnetic order in the studied film at least on the resonant probe time scale $(10^{-15} - 10^{-14}\,\mathrm{s})$. The observed position corresponds to the propagation vector reported of the bulk. On the other hand no magnetic scattering peaks at the $(\frac{1}{2}\pm0.11, 0, \frac{1}{2})$ and $(1.39, 0, \frac{1}{2})$ positions were observed.

A magnetic peak will be extinct when there is no projection of the magnetic moment on the scattered vector at the selected position [58]. However, given the off specular geometry, this condition is not met by all magnetic peaks on the form $(\mathrm{h}, 0, \frac{1}{2})$ simultaneously. Thus an alternative explanation is proposed: Within the
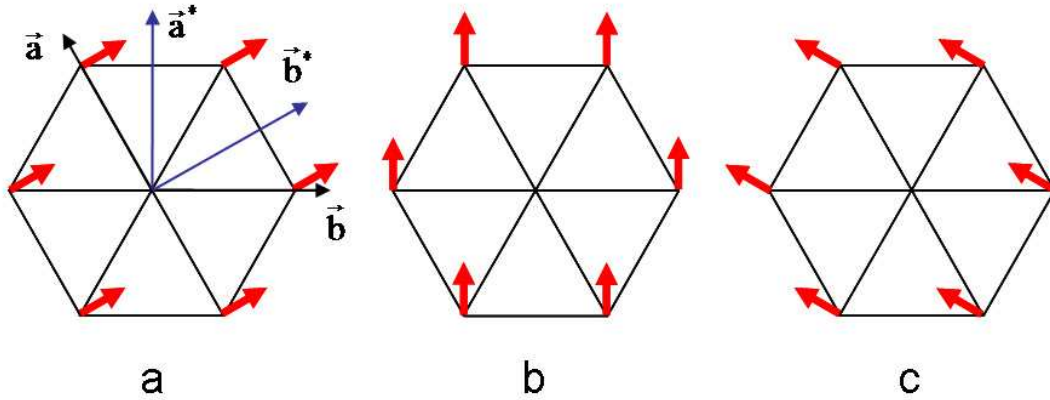
Figure 4.1: Three possible orientations of the magnetic domains in UNi$_2$Al$_3$ thin film with magnetic moments oriented along equivalent crystallographic directions: a) magnetic moments oriented along $(1\bar{1}0)$-direction with the propagation vector $(\pm\frac{1}{2}\pm0.11, 0, \frac{1}{2})$, b) magnetic moments oriented parallel to the film normal ((100)-direction) with the propagation vector $(\pm\frac{1}{2}\pm0.11, 0, \frac{1}{2})$, c) magnetic moments oriented along (010)-direction with the propagation vector $(\pm\frac{1}{2}\pm0.11, 0, \frac{1}{2})$.
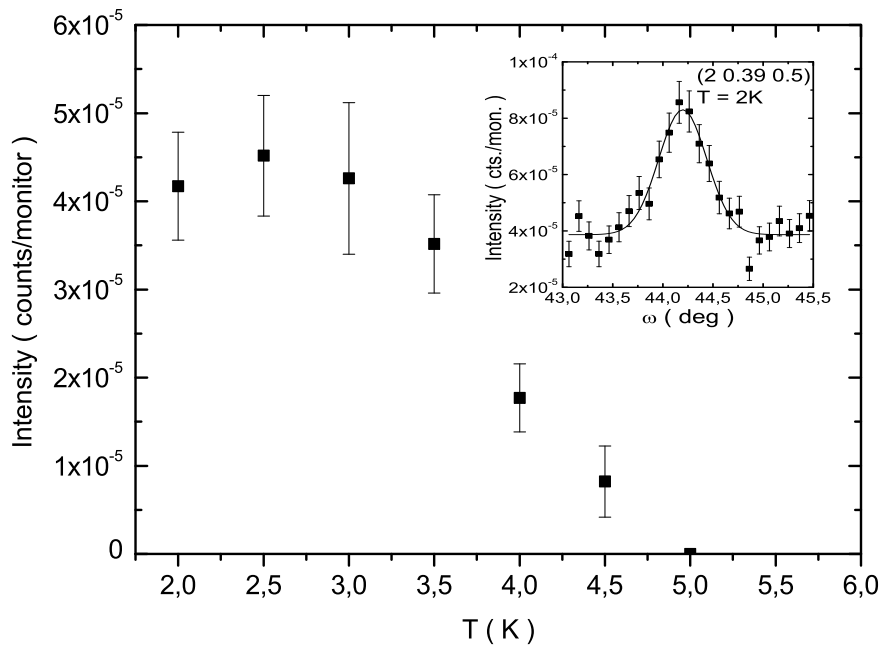
Figure 4.2: Temperature dependence of the integrated scattering intensity of ω-scans (see inset) of the magnetic Bragg-peak $Q_m=(2, 0.39, \frac{1}{2})$.

hexagonal plane of UNi_2Al_3 there are three equivalent crystallographic directions resulting in the formation of three magnetic domains. Since each of these domains is associated with a different magnetic ordering wave vector, $(\pm\frac{1}{2}\pm0.11, 0, \frac{1}{2})$, $(0, \pm\frac{1}{2}\pm0.11, \frac{1}{2})$ and $(\pm\frac{1}{2}\pm0.11, \mp\frac{1}{2}\mp0.11, \frac{1}{2})$, at any given magnetic Bragg position scattering arises from only one magnetic domain (see Figure 4.1). Thus the lack of $(h, 0, \frac{1}{2})$ intensity can be explained by the absence of magnetic domains with moment direction perpendicular to the film surface. In these experiments magnetic scattering was observed from the second domain only, in which the moment direction was rotated by 60° with respect to the film normal. The third domain was not accessible with the goniometer geometry.

The temperature dependence of the integrated intensity of the magnetic Bragg peak $(2, 0.39, \frac{1}{2})$ is shown in Figure 4.2. The UNi_2Al_3 1200Å film orders magnetically below $T_N = (4.7 \pm 0.2)$K, the same temperature where the resistivity curve $R(T)$ shows a kink and increases the magnitude of its slope with decreasing temperature [35].

4.2.1   Correlation lengths

In general, from the width of Bragg reflections information about the correlation lengths of the sample can be obtained (the longitudinal coherence length of the incident photon is $> 1\mu$m). Assuming a constant x-ray intensity in the scattering volume, the scattered amplitude of a finite lattice is proportional to the Fourier transform of a product of three spatial functions given by the lattice periodicity, the atomic group of the unit cell and the exterior shape of the crystal. The exterior shape is described by the form function $\sigma(\mathbf{x})$ which is equal to unity inside the sample volume and zero outside with the Fourier transform $\Sigma(\mathbf{s})$. The corresponding reciprocal space is given by the set of functions $\Sigma(\mathbf{s})$ repeated around each node of the reciprocal lattice extending to infinity [59]. Thus the broadening of the reciprocal lattice points Δq_i due to correlation length ℓ_i or finite size effects in a given direction can be estimated by $\Delta q_i \simeq 2\pi/\ell_i$. However, the basic assumption that the x-ray intensity is constant within the sample volume is inconsistent with the resonant nature of the scattering process which results in an intensity fall off within the thin film [60]. This reduces the effective scattering volume and alters the relevance of $\Delta q_i \simeq 2\pi/\ell_i$ to a lower bound of the correlation length.

A sometimes dominant contribution to the peak width is obtained from crystal
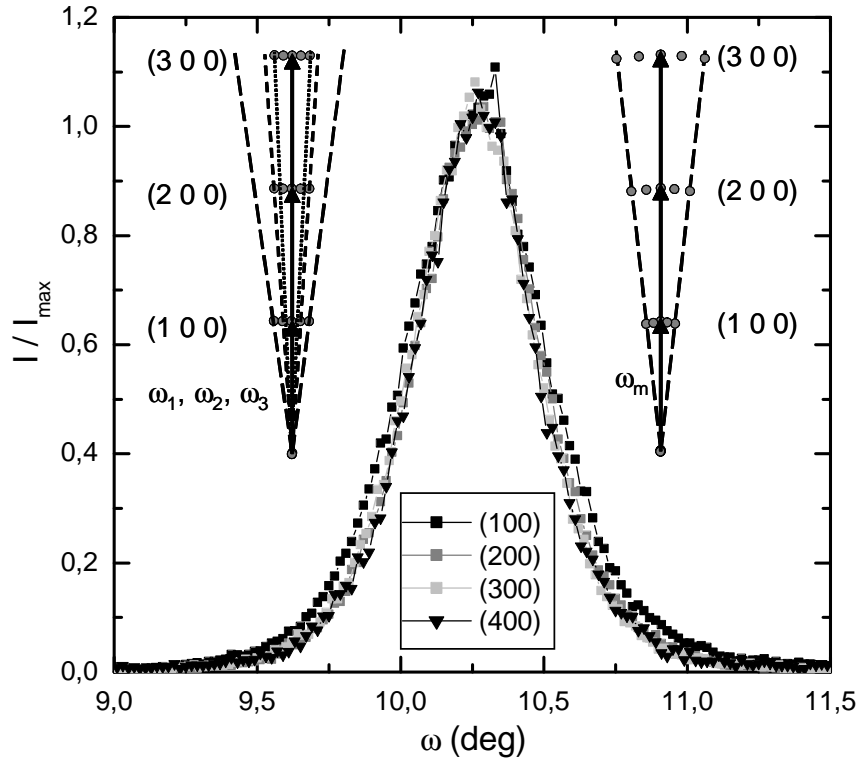
Figure 4.3: ω-scans of the specular (h00) peaks (h=1,2,3,4) of a 1200Å UNi$_2$Al$_3$ thin film. The ω axis of the higher order peaks are shifted to display the scans on top of each other. (measured with a standard 2-circle diffractometer, Cu-anode). Right inset: Schematic representation of the peak broadening due to mosaic spread. Left inset: Schematic representation of the peak broadening due to a finite correlation length within the film plane.

mosaic spread. In epitaxial thin films with island growth mode mosaic spread arising from a distribution of tilting angles ω_m of the crystallite axes perpendicular to the substrate is a common feature. This generates spherical-shell segments in reciprocal space centered at the origin of the specular reciprocal lattice vector with dimensions depending on the scattering order (see right inset of Fig. 4.3).

On the other hand correlation length effects due to atomic disorder or finite size effects generate a broadening which is the same for all points in reciprocal space (see left inset of Fig. 4.3). Thus rocking curves (ω-scans) of specular Bragg reflections of increasing order have the same ω-width if the broadening is dominated by the mosaic spread and a decreasing width if the broadening is due to correlation length effects. In Fig. 4.3 rocking curves of the (h00) peaks (h=1,2,3,4)

are shown. For $h \geq 2$ no dependence of the curve width on h is observable, the (100) curve is only slightly broader than the other curves. Thus the broadening of the structural reciprocal space points is dominantly due to the crystal mosaic with the angular full width at half height of $\omega_m \simeq 0.42°$.

The width of the magnetic Bragg reflections can be discussed in the framework of the magnetic correlation length. The magnetic scattering vectors of the UNi$_2$Al$_3$ thin films are off-specular with an angle φ between the film normal (1, 0, 0) and the scattering vector Q. For the magnetic peak $Q_m =$(2, 0.39, 0.5) $\phi = 16.6°$ is obtain . Thus for an h-scan of Q_m the measured h-width Δh_{Q_m} is similar to the pure correlation length broadening (rlu: reciprocal lattice units): $\Delta h'_{Q_m} = \Delta h_{Q_m} \cdot \cos \phi = (0.0062 \pm 0.0005)\text{rlu} \cdot 0.96 = (0.0059 \pm 0.0005)\text{rlu}$ (see Figure 4.4).
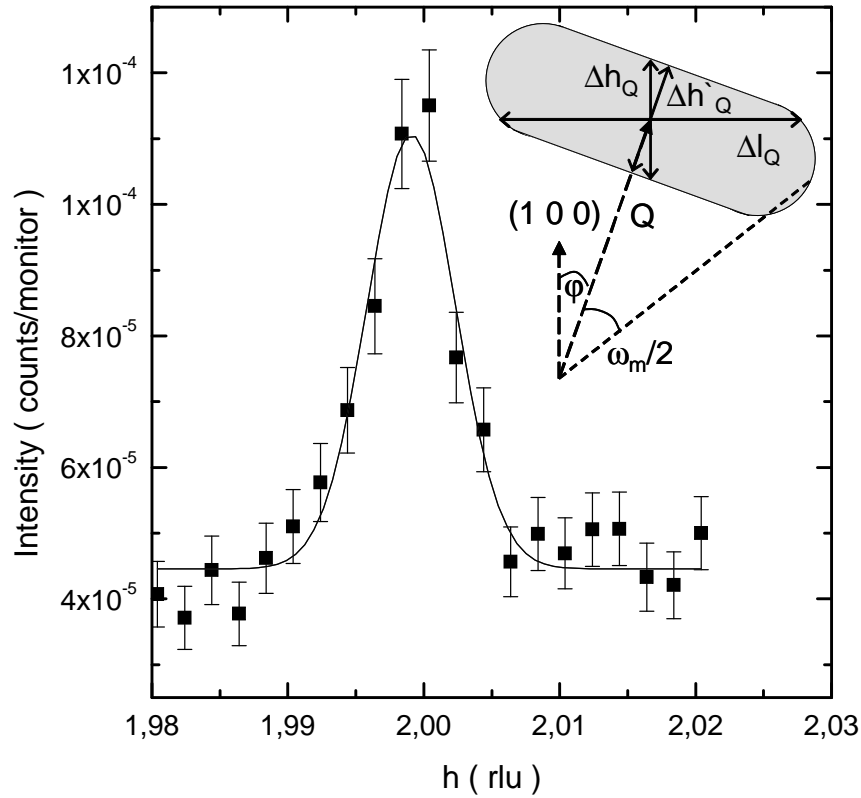
Figure 4.4: Scan parallel to the a^*-axis around the magnetic Bragg position Q_m=(2, 0.39, $\frac{1}{2}$) of UNi$_2$Al$_3$ (T = 2K). Inset: Schematic representation of the influence of mosaicity and finite correlation length on the peak broadening in reciprocal space (see text).

From this a magnetic correlation length of $\ell_{m,h} = (|a|\cos 30°)/\Delta h'_{Q_m} > (760 \pm 60)$Å is calculated. Thus the UNi$_2$Al$_3$ thin films show magnetic order in the a^*-direction (the direction of the surface normal) with a correlation length which exceeds the lower limit (400Å, [23]) estimated for bulk single crystals. At the same wavelength the structural peak $Q_s = (2, 0, 1)$ has a similar correlation length $\ell_{s,h} > (800 \pm 15)$Å.

Given the film thickness of $d = (1200 \pm 50)$Å as determined from rate monitors during the growth process these lower bounds suggest a magnetic and structural correlation which extends over the complete film thickness.

For the determination of the magnetic in plane correlation lengths of the epitaxial thin film scans of Q_s and Q_m along the c axis (l-scan) and a axis were performed. However, the peaks are strongly broadened in these directions due to the mosaic spread (broadening for the l-scan: Δl_Q, see inset of Fig. 4.4). The measured widths are consistent with this mosaicity and no additional broadening is necessary to describe the data within the error of our experiment. Only a lower bound for the magnetic correlation length, independent of the direction in the film plane, of $\ell_{m,in-plane} > 500$Å can be given.

The performed resonant magnetic x-ray scattering experiments have shown that epitaxial thin films of UNi$_2$Al$_3$ exhibit the same type of incommensurable antiferromagnetic order as bulk samples. The magnetic correlation length $\ell > 800$Å estimated from resonant magnetic x-ray scattering exceeds the lower boundary obtained from neutron scattering experiments on bulk samples. The formation of a magnetic domain with a moment direction perpendicular to the film surface seems to be energetically unfavorable, possibly since it would imply an uncompensated magnetic moment.

Chapter 5

Transport measurements

Transport measurements were performed in order to investigate the electronic properties of UNi$_2$Al$_3$ thin films in the normal and superconducting states. Within the scope of this work a detailed study of the temperature dependent resistivity and upper critical magnetic field of UNi$_2$Al$_3$ thin films was performed. The following chapter presents a survey of these experiments.

5.1 Standard R(T)-characterization

Measurements of the temperature dependent resistivity $R(T)$ were performed on all thin films as the last characterization step in order to determinate the sample purity, the superconducting critical temperature T_c and the magnetic transition temperature T_N. The resistance was measured using a standard four-point dc method with the current flowing in the film plane.

Figure 5.1 shows the $R(T)$ dependences of several UNi$_2$Al$_3$ thin films. The observed temperature dependence of the resistance of the samples on both kinds of YAlO$_3$ substrate is consistent with the behavior known from bulk samples [9, 30, 61]. The residual resistance ratio $RRR = R_{300K}/R_{1.1K}$ of the best samples is about $RRR \simeq 10$ with a residual resistance amounting to $\rho_a = 12\,\mu\Omega$cm. This is approximately one-third of the RRR reported for the best bulk single crystals [31], indicating a higher concentration of scattering centers in the thin films. However, most of these scattering centers are probably related to surface and interface scattering, which are typical for thin film samples and not effective in destroying the superconducting state since the transition temperature T_c and the width ΔT_c of the films is as high and sharp as in the best bulk single crystals. The films
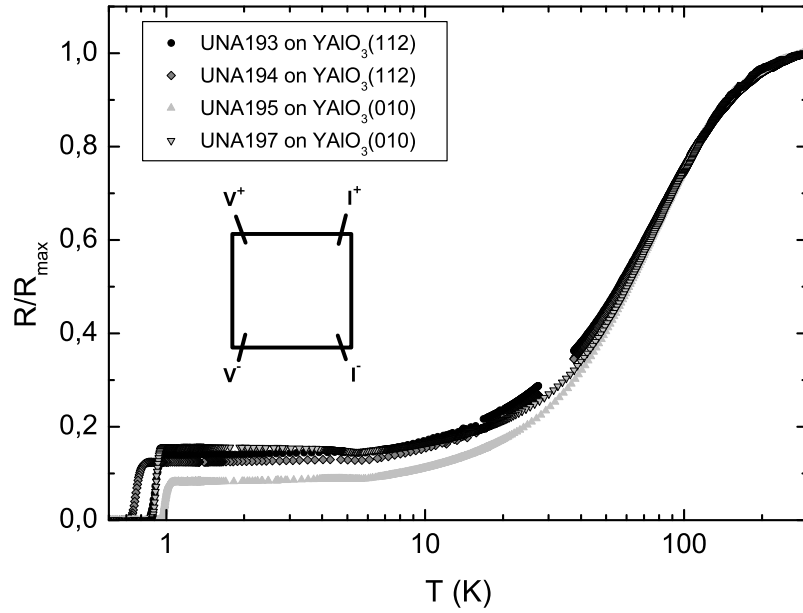
Figure 5.1: Normalized resistance $R(T)/R_{max}$ of several UNi$_2$Al$_3$ thin films on two different substrate types. Inset: Schematic of the measurement geometry (4-point dc method).
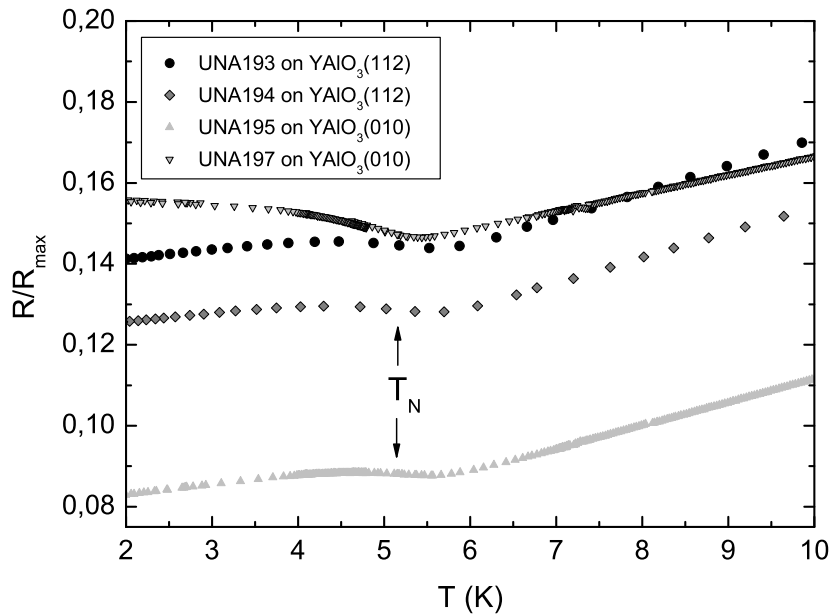
Figure 5.2: Normalized resistance $R(T)/R_{max}$ of several UNi$_2$Al$_3$ thin films at the Neel temperature T_N.

with a thicknesses $d > 100\,\text{nm}$ become superconducting at $T_c^{max} = 1.05\text{K}$ with resistive transition widths $\Delta T_c \simeq 0.05\text{K}$. A clear anomaly in the resistivity curves R(T) identifies the magnetic ordering temperature at $T_N \simeq 5\,\text{K}$ (Figure 5.2).

Thin films with thicknesses reduced to below $d \simeq 50\,\text{nm}$ reveal a qualitatively identical behavior of the resistance but typically with reduced residual resistance ratio and superconducting critical temperature. This quality deterioration of the ultrathin films could be due to the specific morphology of UNi_2Al_3 films. If the film thickness d is comparable with the average height of the islands the electron scattering at the film surface becomes significant concerning the transport properties of the films.

5.2 Transport anisotropy

Evidence for a transport anisotropy in UNi_2Al_3 thin films depending on the current direction became apparent by standard four-point resistivity measurements performed on non patterned thin film samples. The curves measured with the current-voltage terminals along the crystallographic a axis as well as along the c
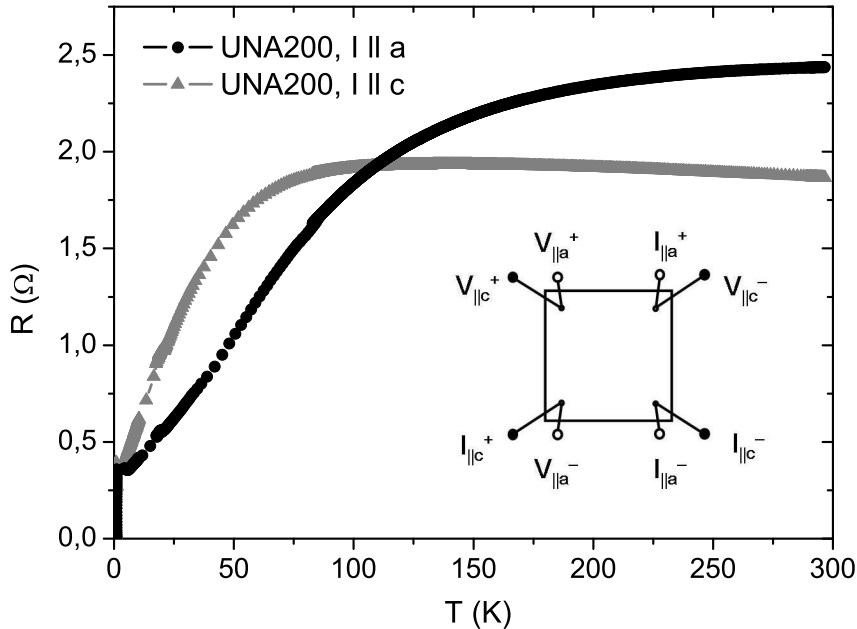
Figure 5.3: R(T) dependence of non patterned UNi_2Al_3 thin film. The inset shows the geometry of the measurement for two different current directions.
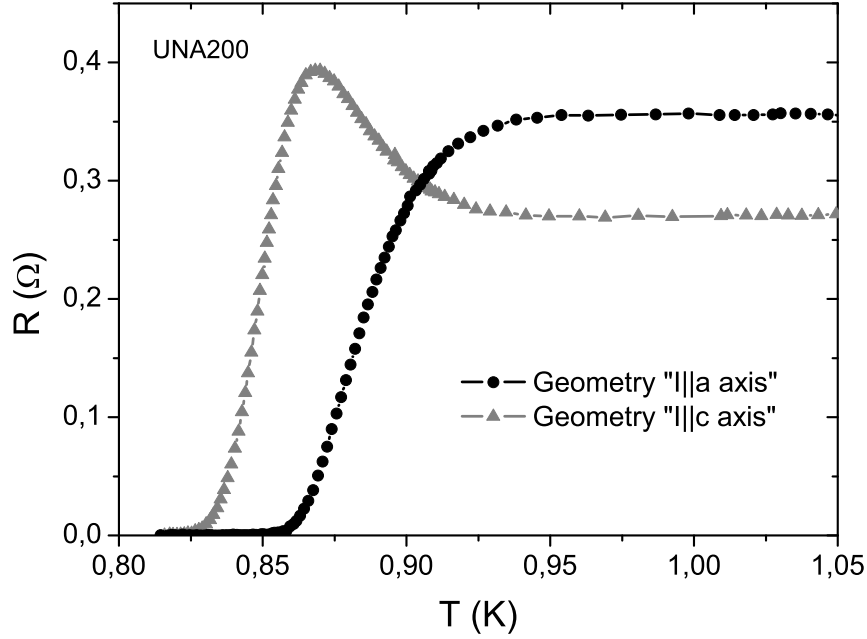
Figure 5.4: Superconducting resistive transitions of a non patterned UNi_2Al_3 thin film for different measurement geometries. For current direction $I \parallel a$ the transition is observed at higher temperature compared to $I \parallel c$. The rise of the curve for $I \parallel c$ appears due to an increase of the voltage signal caused by a redistribution of the current density in the unpatterned sample.

axis reveal a strong anisotropy of the temperature dependence of the resistance (Figure 5.3). Moreover, for the same samples the superconducting transitions were observed at different temperatures for different terminal geometries (Figure 5.4). The increasing of the resistance measured in geometry $I \parallel c$ below the temperature of a superconducting onset in geometry $I \parallel a$ can be explained by an increase of the signal at the voltage terminals due to a redistribution of the current density in the square shaped sample.

Patterning the samples by a standard photolithographic process with ion beam etching made it is possible to obtain well defined geometries for the detailed investigation of anisotropic transport properties. By using special structures measurements can be performed for current directions parallel to different crystallographic axis of the same thin film.

Figure 5.5 represents measurements of the temperature dependent resistivity $R(T)$ of a sample performed with the current direction parallel to the crystallo-
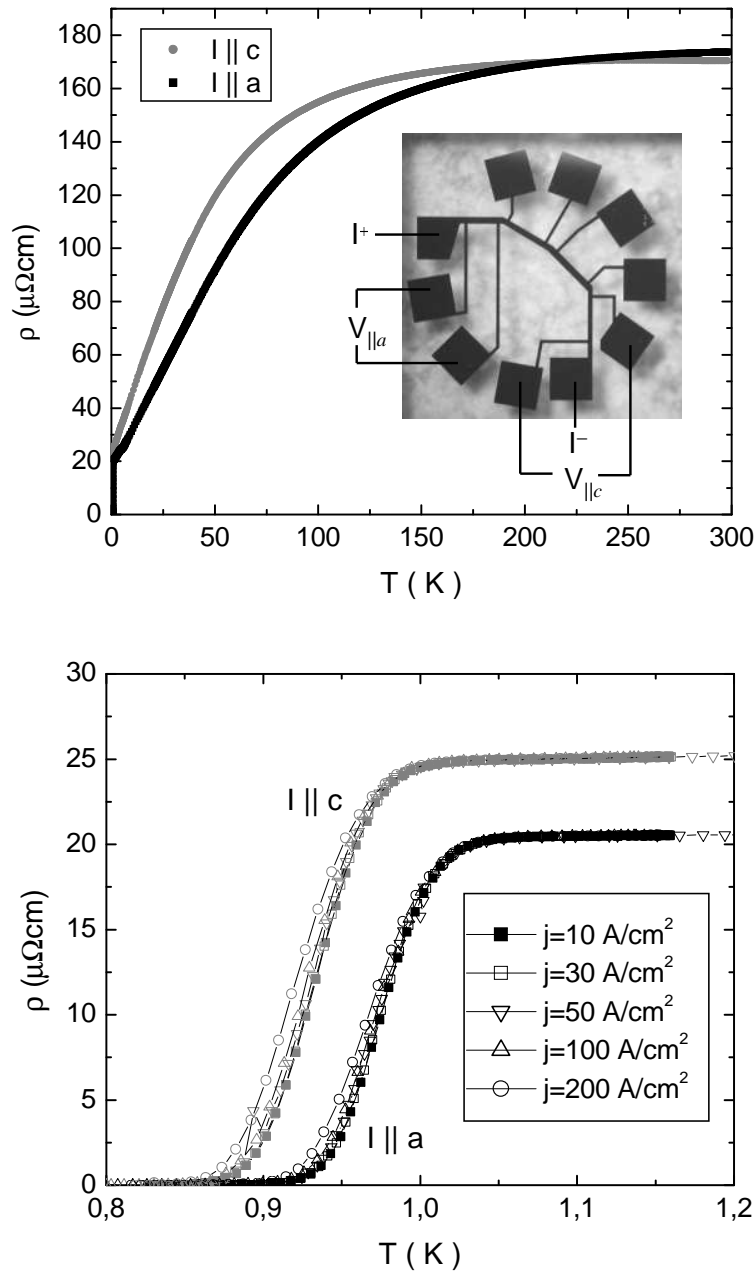
Figure 5.5: Upper panel: Specific resistivity $\rho(T)$ of an UNi$_2$Al$_3$ thin film for different current directions (black squares: $I \parallel a$, grey dots: $I \parallel c$). Inset: Photograph of a patterned UNi$_2$Al$_3$ film (4×4mm). For $R(T)$ measurements a current is sent through the central conductor path (width $d = 100\,\mu$m), the thin strips are voltage probes (4-point dc method). Lower panel: Superconducting resistive transitions of an UNi$_2$Al$_3$ thin film for different current directions (black symbols: $I \parallel$ a, grey symbols: $I \parallel$ c). Measurements with different current densities demonstrate that the probe current does not influence the T_c values (for $10\,\mathrm{A/cm}^2 < j < 200\,\mathrm{A/cm}$).

graphic a axis as well as parallel to the c axis of the same thin film. A pronounced anisotropy was observed.

The residual resistivities of this sample are $\rho_c = 25\mu\Omega$cm for $I \parallel c$ and $\rho_a = 20\mu\Omega$cm for $I \parallel a$. The residual resistance ratios $RRR = R_{300K}/R_{1.1K}$ amount to $RRR_{I\parallel c} = 6.6$ and $RRRI \parallel a = 8.3$. The film becomes superconducting at $T_c^{mid} = 0.98$ K with a resistive transition width $\Delta T_c \simeq 0.1$ K. Large critical current densities of $I_c \simeq 10^4$ A/cm^2 at $T = 0.32$ K for $I \parallel a$ and $I \parallel c$ show that the observed superconductivity is a property of the complete thin film volume. The superconducting transition for current direction $I \parallel c$ was observed at a reduced temperature compared to $I \parallel a$ with $T_c(I \parallel a) - T_c(I \parallel a) \simeq 0.05$ K. The variation of the probe current revealed only weak influence on the transition temperature. At the lowest current densities no influence on the resistive transition was observed (Fig. 5.5 lower panel).

In Figure 5.6 the superconducting transitions of the three samples with the
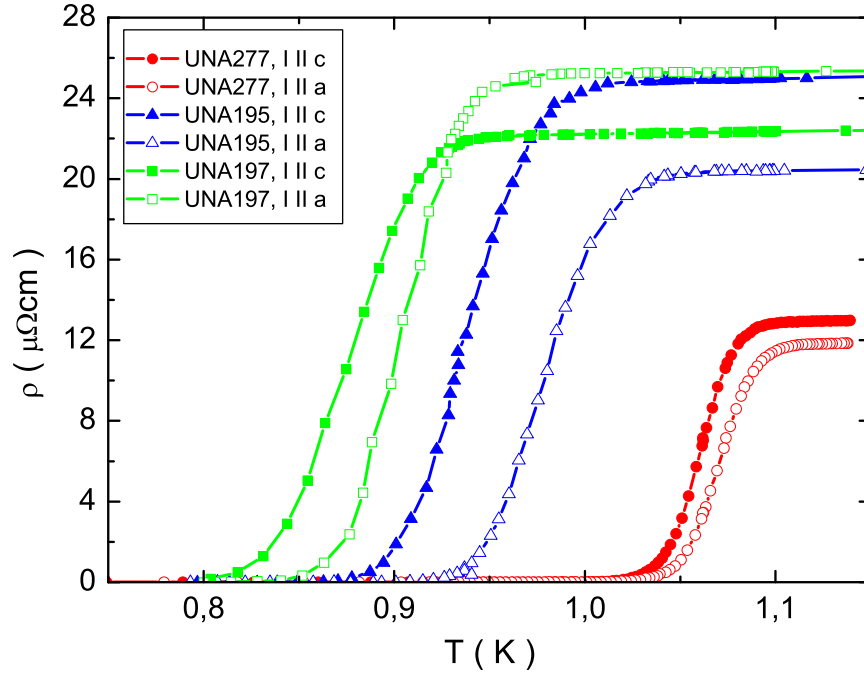
Figure 5.6: Superconducting resistive transitions of different UNi$_2$Al$_3$ films for current directions $I \parallel a$ and $I \parallel c$. The superconducting transition for $I \parallel a$ is observed at slightly increased temperatures compared with $I \parallel c$ for all superconducting samples on both kinds of YAlO$_3$ substrates.

highest transition temperatures prepared up to now are shown. Although the
splitting is quantitatively different from sample to sample, the transition for $I \parallel a$
was always observed at slightly increased temperatures compared with $I \parallel c$ for all
superconducting samples on both kinds of $YAlO_3$ substrates. The same behavior
is visible at a close inspection of the only published $R(T)$-data of a bulk single
crystal by Sato et al. [30]. Thus there is strong evidence that the directional
dependence of the resistive T_c is an intrinsic property of UNi_2Al_3.

A possible explanation for this effect is the existence of two bands in UNi_2Al_3
with intraband pairing interactions but with a very weak superconducting in-
terband interaction. According to ref. [62] an extension of the BCS theory to
the case of two bands with no interband pairing can result in two supercon-
ducting gaps on the Fermi surface which open at different temperatures. The
authors of ref. [62] discuss the corresponding result for the superconducting state
of transition metals with $s-d$ bands, but the same concept can be applied to any
multiband superconductor with any type of superconducting pairing interaction.

Considering a superconductor with, for example, $s-f$ bands, the formation
of the Cooper pair may take place in the following way. The Hamiltonian that is
amenable to the formation of ss, ff, sf and fs pairs takes the form

$$H = \sum_{k\sigma} \epsilon_{ks} c^*_{k\sigma} c_{k\sigma} + \sum_{k\sigma} \epsilon_{kf} d^*_{k\sigma} d_{k\sigma} - V_{ss} \sum_{kk'} c^*_{k\uparrow} c^*_{-k\downarrow} c_{-k'\downarrow} c_{k'\uparrow} - V_{ff} \sum_{kk'} d^*_{k\uparrow} d^*_{-k\downarrow} d_{-k'\downarrow} d_{k'\uparrow}$$

$$-V_{sf} \sum_{kk'} (c^*_{k\uparrow} c^*_{-k\downarrow} d_{-k'\downarrow} d_{k'\uparrow} + d^*_{k\uparrow} d^*_{-k\downarrow} c_{-k'\downarrow} c_{k'\uparrow}).$$

The first and the second term in this expression describe the kinetic energies
of the s- and f-band, respectively. The last three terms contain the averaged
interaction energies V_{ss}, V_{ff}, and V_{sf} resulting in the formation of $s-s$, $f-f$, and
$s-f$ Cooper pairs, respectively.

According to ref. [62] the transition temperature for this system can be found
as

$$k_B T_c = 1.11 \hbar \omega \exp \left[-\frac{[V_{sf}^2/N_s N_f + \frac{1}{4}(V_{ff}/N_s - V_{ss}/N_f)^2]^{\frac{1}{2}} + \frac{1}{2}(V_{ff}/N_s + V_{ss}/N_f)}{V_{sf}^2 - V_{ss} V_{ff}} \right]$$

When the attractive electron interaction is caused by interband scattering pro-
cesses only (s-f processes, $V_{ss} = V_{ff} = 0$) the same transition temperature as in
a simple one band model, but with a density of states given by $(N_s N_d)^{\frac{1}{2}}$ will be
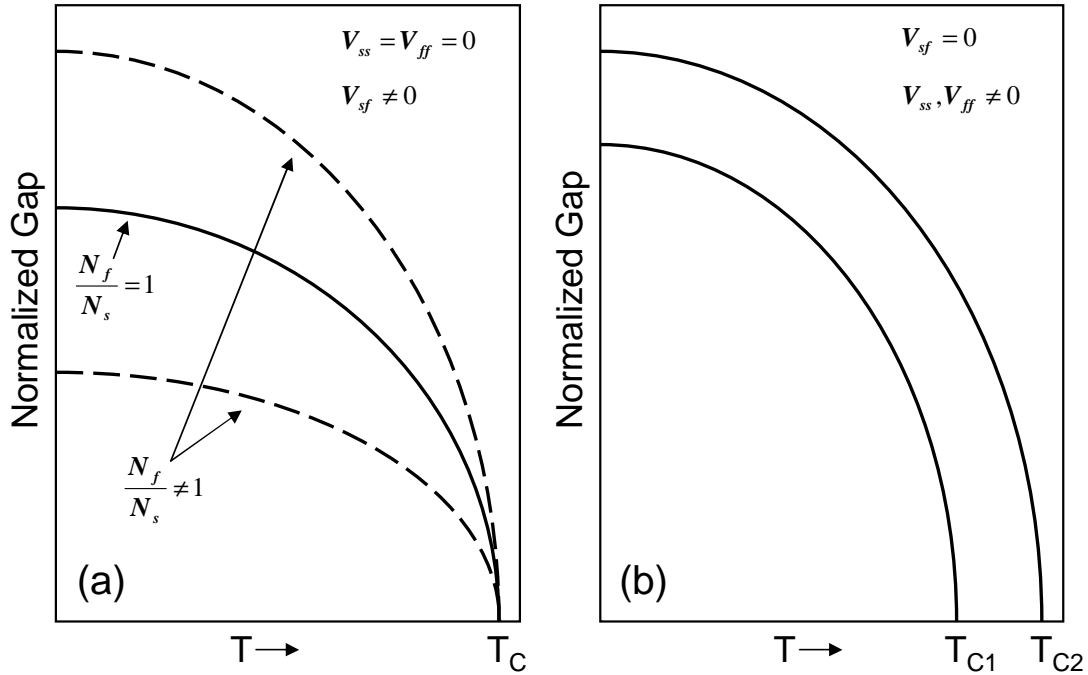
Figure 5.7: Qualitative temperature dependencies of the energy gaps of multiband superconductor. (a): The gap pairs for the case of interband pairing only ($V_{ss} = V_{ff} = 0$). The curves for V_{ss}, V_{ff}, $V_{sf} \neq 0$ are very similar to those shown, axcept when $V_{sf}^2 << V_{ss}V_{ff}$. (b): In the special case of intraband pairing ($V_{sf} = 0$) there are two superconducting gaps with two different transition temperatures.

obtained. However, unless $N_s = N_d$ there are two energy gaps (Figure 5.7a). If the Cooper pairs are formed within the bands only (intraband scattering: s - s and f - f processes, $V_{sf} = 0$), there are two superconducting gaps with two different transition temperatures (Figure 5.7b).

However, even in the case of multiband superconductivity with two gaps opening at different temperatures the existence of different resistive transition temperatures which depend on the current direction is possible only at certain conditions. It is obvious, that the anisotropy on the resistive transition depends on the shape of the Fermi surface and the gap distribution on it. Figure 5.8 represent two Fermi surface models of a multiband superconductor assuming the gaps opening on separate sheets of the Fermi surface. When the gaps are distributed on two Fermi surface spheroids (Figure 5.8a), there are no directional restrictions for a supercurrent spreading. In this case there is the same resistive transition
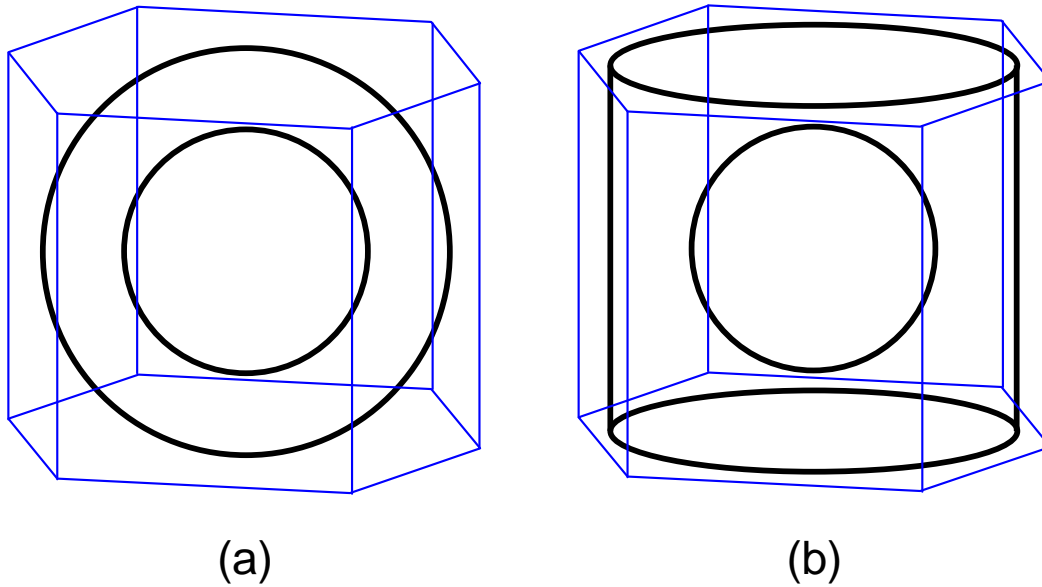
Figure 5.8: Fermi surface examples of a multiband superconductor with the superconducting gaps opening on separated sheets of the Fermi surface: (a) Both gaps are distributed on two Fermi surface spheroids; (b) One of the gaps is distributed on a two dimensional cylinder, another - on a spheroid inside the cylinder.

temperature for all current directions which corresponds to the higher transition temperature T_{c2}. In such a superconductor it is impossible to indicate an opening of another superconducting gap at the lower transition temperature T_c by means of resistivity measurements.

A directional dependence of the transition temperature will appear when the part of the Fermi surface enclosing the gap with the higher T_c is degenerated in a two dimensional sheet. Indeed, when the gap opens on a cylinder (Figure 5.8b), the superconducting current on this sheet can not flow in the direction along the cylinder axis and the resistive transition on the sheet with the lower critical temperature could be observed for this current direction.

The calculated Fermi surface of UNi$_2$Al$_3$ [63] is shown in Figure 5.9 together with the Fermi surface of UPd$_2$Al$_3$ [64, 65], which does not exhibit a different resistive transition temperature for different crystallographic directions. The complicated multisheeted Fermi surfaces of these isostructural compounds consist of four main parts, so called *party hat*, *cylinder*, *cigars* and *eggs*. The first
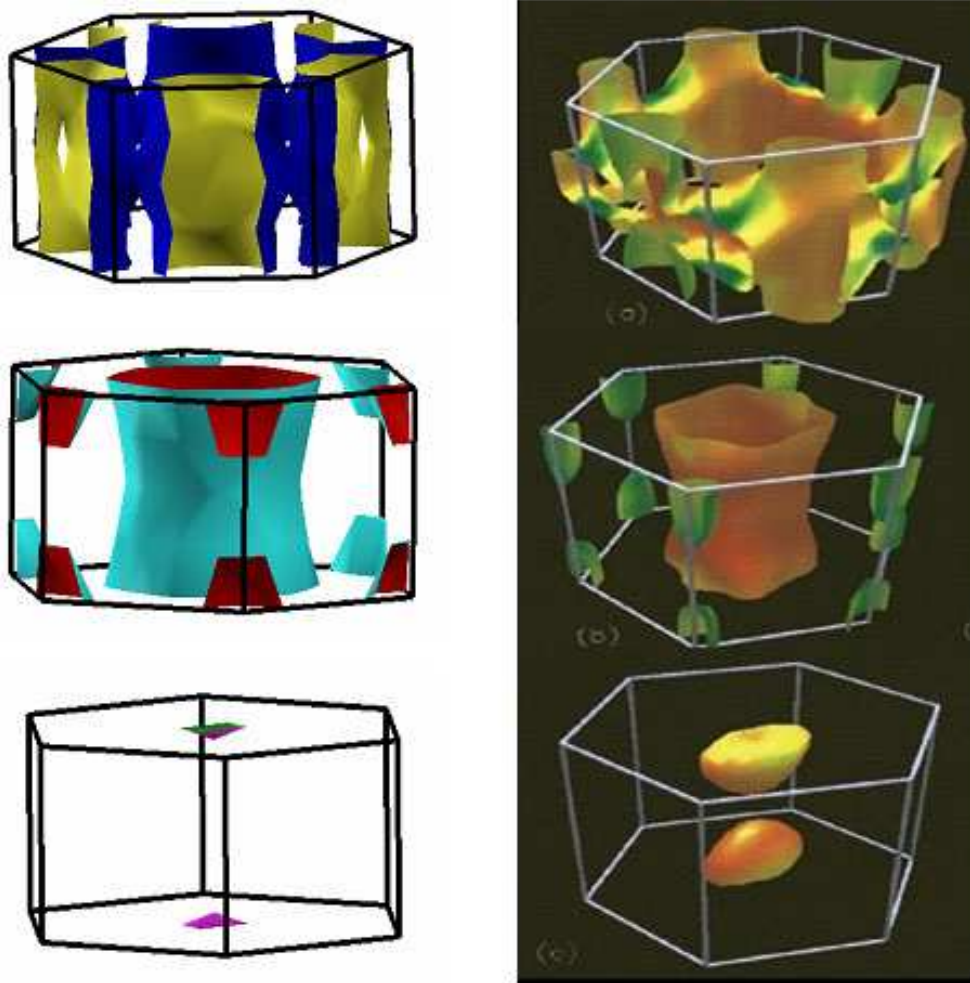
Figure 5.9: Calculated Fermi surfaces of UNi$_2$Al$_3$ (left) and UPd$_2$Al$_3$ (right). Four parts of the structure are represented in different sections for clarity: (a) *party hat*, (b) *cylinder* and *cigars*, (c) *eggs*. Figures taken from [63, 64].
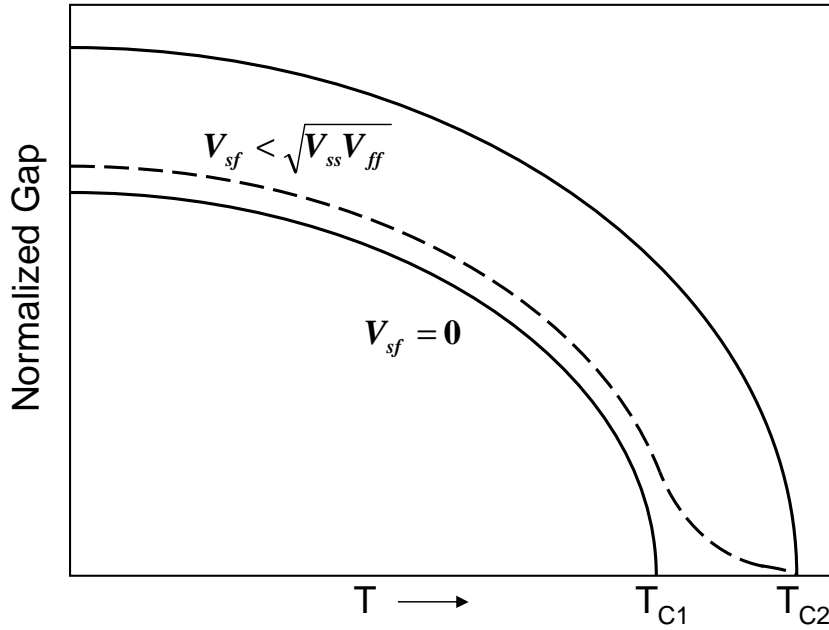
Figure 5.10: By a weak coupling between the two bands ($V_{sf}^2 << V_{ss}V_{ff}$) the lower transition temperature disappears at $\Delta \to 0$ in the manner shown. Figure adopted from Suhl et al. [62].

three sheets are very similar in both compounds, but the *eggs* are much smaller in UNi$_2$Al$_3$ than in UPd$_2$Al$_3$. In reality they could even fully disappear, making the Fermi surface extremely two-dimensional. On such a Fermi surface superconducting gaps opening at different temperatures on different sheets could result in transition temperatures which depend on the current direction.

However, it is very improbable, that in a real multiband superconductor only interband pairing takes place. The coexistence of both couplings is more realistic, though, one of the couplings can dominate. According to ref. [62] a weak coupling between the two bands results in two gaps with a common T_c. However, in one of the bands an initially tiny energy gap is expected which opens drastically at a reduced temperature compared to T_c (Figure 5.10). In a transport experiment such a situation is presumably indistinguishable from the case of two different T_c values because critical current effects can hide the tiny energy gap. Thus, for an accurate inspection of the superconducting transition region small current densities should be used.

The employed structure (see inset of Fig. 5.5) allows to measure the voltage
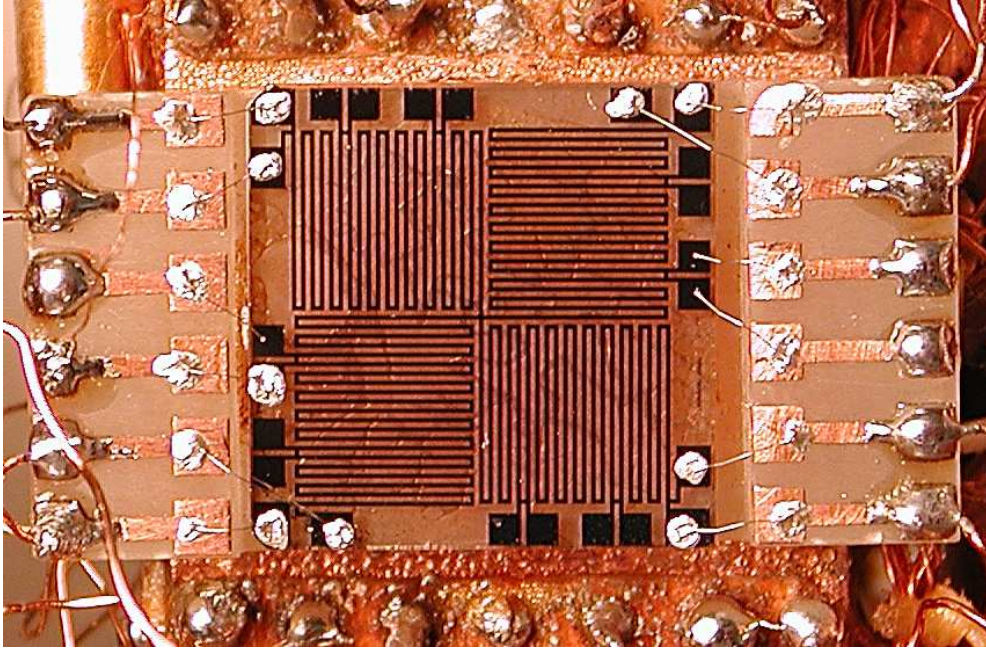
Figure 5.11: Photograph of a meander patterned UNi$_2$Al$_3$ thin film.

drop with sufficient accuracy at current densities down to $5\,\mathrm{A/cm^2}$. In order to investigate the anisotropy at the superconducting transition more carefully another sample was prepared. A meander structure (Figure 5.11) was designed especially for transport measurements with very low current densities. Increasing the length of the conducting paths makes it possible to keep the voltage signal at a sufficiently high level with current densities reduced by a factor of 500 compared to the previously used structure. The meander structure consists of two parts on a $10 \times 10\,\mathrm{mm}$ substrate, each designed for maximum length in one crystallographic direction with minimum contribution of the orthogonal direction. The dimensions of the current paths are: total length in main direction $L = 168\,\mathrm{mm}$; total length in orthogonal direction: $l = 4\,\mathrm{mm}$; width: $b = 100\,\mu\mathrm{m}$; film thickness: $d = 150\,\mathrm{nm}$. Since the contribution of the orthogonal direction is around 2.4% only, the influence on the shape of the transitions is small. With a $T_c = 1.07\,\mathrm{K}$, this sample showed the highest transition temperature ever observed in UNi$_2$Al$_3$ thin films.

Figure 5.12 shows the temperature dependence of the resistivity of the meander sample. A similar anisotropic behavior of the resistivity was observed. The residual resistance ratios of this film are $RRR_{I\|c} = 8.9$ and $RRR_{I\|a} = 10.1$ with
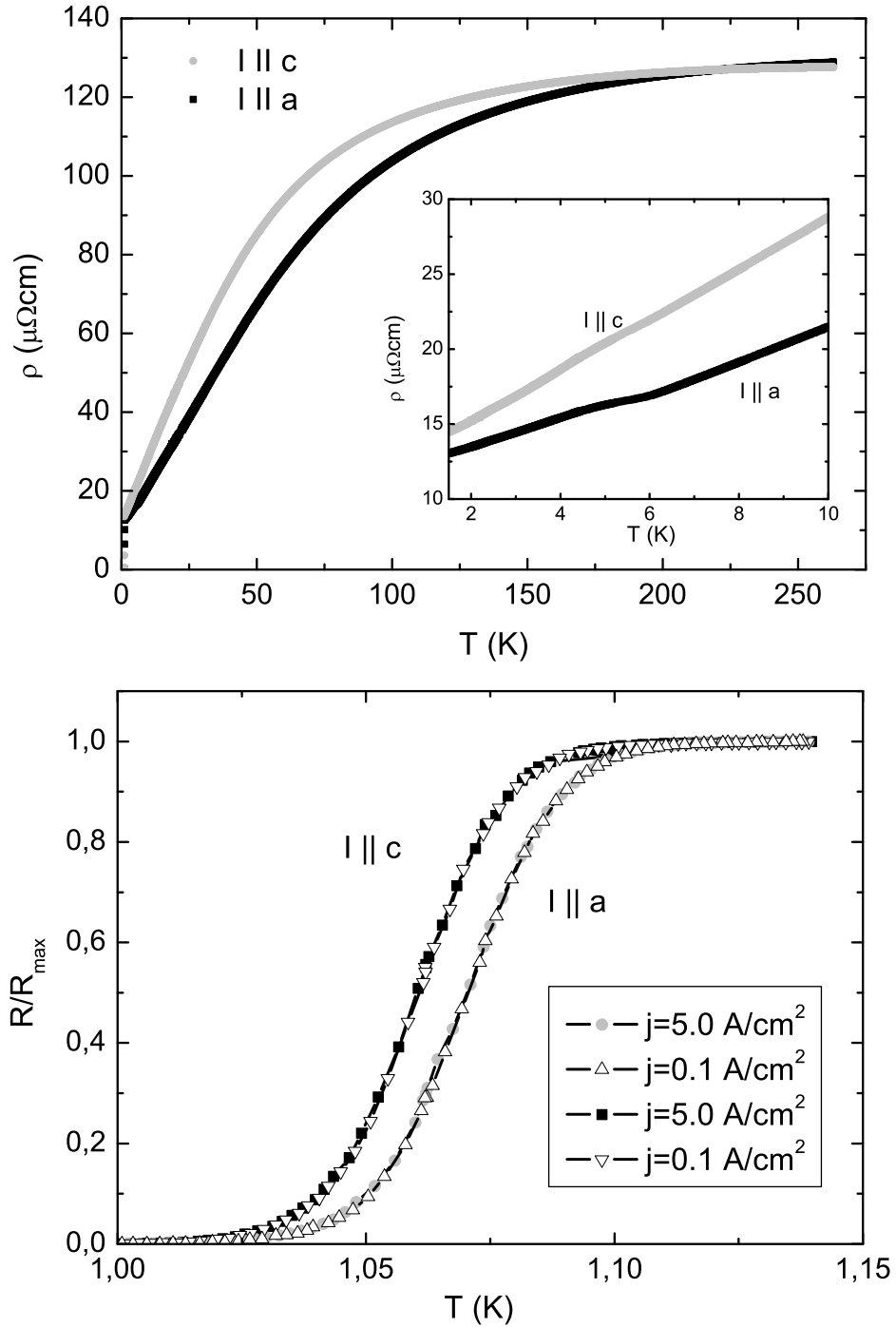
Figure 5.12: Upper panel: specific resistivity $\rho(T)$ of an UNi$_2$Al$_3$ meander structure for different current directions (black symbols: $I \parallel$ a, grey symbols: $I \parallel$ c). Inset: $\rho(T)$ of an UNi$_2$Al$_3$ thin film at T_N. Lower panel: superconducting resistive transitions of an UNi$_2$Al$_3$ meander structure for different current directions with different current densities.

residual resistivities amounting to $\rho_c = 14.1\mu\Omega$cm for $I \parallel c$ and $\rho_a = 12.8\mu\Omega$cm for $I \parallel a$. The film becomes superconducting at $T_c^{mid} = 1.07$K for $I \parallel a$ and at $T_c^{mid} = 1.06$K for $I \parallel c$ with the same resistive transition widths $\Delta T_c \simeq 0.07$K. The lower panel of Figure 5.12 shows the superconducting resistive transition of the film for different current directions with two different current densities. It is obvious, that the transition curves for each current direction are absolutely identical for current densities $j < 5$ A/cm^2. The resistive transition for the current direction $I \parallel c$ does not shift to higher temperatures with decreasing probe current down to the lowest limit. No indications of a possible merging of the transition curves were observed. The results do not support the model of multiband superconductivity of UNi$_2$Al$_3$. However, the simple model of ref. [62] presents only the first attempt to explain the directional dependence of T_c and does not consider the coupling between superconductivity and magnetism as well as the order parameter anisotropy of UNi$_2$Al$_3$. In order to explain the phenomena of the directional dependence of T_c in UNi$_2$Al$_3$ thin films additional experimental investigations are needed. Moreover, possible alternative sources for the direc-
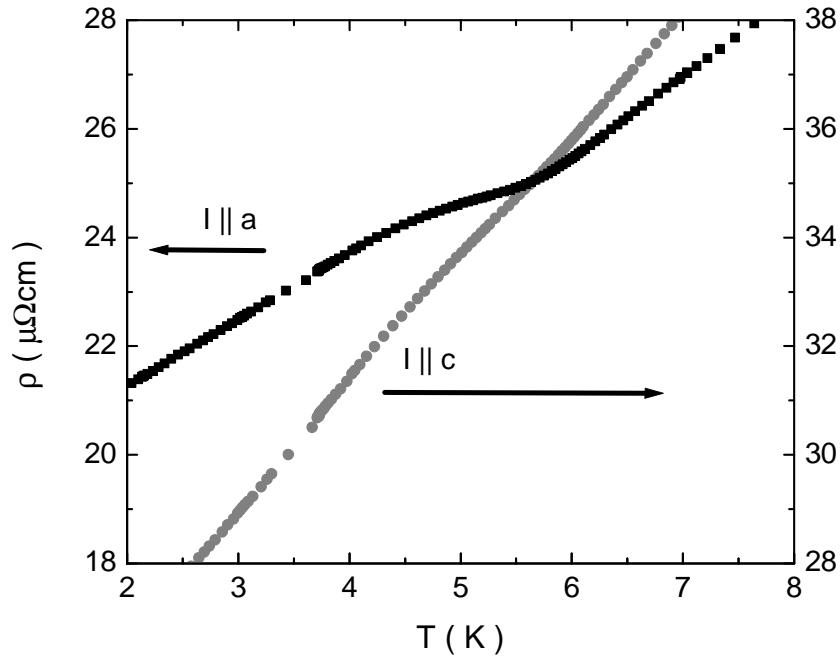
Figure 5.13: Specific resistivity $\rho(T)$ of an UNi$_2$Al$_3$ thin film. Left axis: $I \parallel a$ (black squares). Right axis: $I \parallel c$ (grey dots).

tional dependence of T_c such as scattering on crystal defects or grain boundaries as well as vortex dynamics have to be considered.

Resistivity measurements of UNi_2Al_3 films in the normal state reveal an anisotropic influence of the magnetic features on the transport properties. At the magnetic ordering temperature $T_N \simeq 5\,K$ a clear anomaly in the resistivity $R(T)$ of the films is visible for currents $I \parallel a$ but not for $I \parallel c$ (Fig. 5.13). The influence of the magnetic ordering on the resistivity of UNi_2Al_3 is different from the behavior of UPd_2Al_3 where a clear steepening of $R(T)$ is observed on cooling beyond T_N for $I \parallel a$ as well as for $I \parallel c$ [66]. In contrast, in the UNi_2Al_3 films a flattening of $R(T)$ at T_N is observed for $I \parallel a$ which is similar to the behavior of URu_2Si_2 [67]. This dependence can result from a change in the Fermi surface topology associated with the formation of a magnetization-density wave which opens a gap over a portion of the Fermi surface. Since $R(T)$ of UNi_2Al_3 is not affected by the magnetic ordering for currents $I \parallel c$ it can be concluded that only the sheet of the Fermi surface providing the a-axis transport couples to the magnetic order parameter.

The observation of the higher superconducting T_c on the Fermi surface sheet which is more affected by the magnetic ordering provides evidence that the same electrons are responsible for superconductivity and magnetism.

5.3   Upper critical magnetic field H_{c2}

The upper critical field H_{c2} of a superconductor is determined as the value of the external magnetic field above which the bulk superconductivity of the sample is completely destroyed. The external magnetic field breaks the Copper pairs by affecting the orbital motion and the spins of the paired electrons, determining two main mechanisms: *orbital* and *paramagnetic* pairbreaking, respectively. The orbital pairbreaking is described in the Hamilton operator by the Lorenz term $e/m\vec{A} \cdot \vec{p}$ $(\vec{H} = \vec{\nabla} \times \vec{A})$. This mechanism takes place in all (conventional and unconventional) superconducting states. At low magnetic fields it is the dominant pairbreaking effect. Therefore the initial slope of H_{c2} close to T_c is determined basically by the orbital pairbreaking. The orbital critical field H_{c2}^{orb} is the critical field which the superconductor would have in the absence of a magnetic field interaction with the spins of the electrons. For a BCS s-wave superconductor the

orbital critical field H_{c2}^{orb} at $T \to 0$ is given by [68]

$$H_{c2}^{orb} = n \frac{(-dH_{c2}/dT)_{T_c}}{T_c},$$

where the coefficient n takes values between 0.693 in the dirty limit ($l << \xi_0$) [69] and 0.727 in the clean limit ($l >> \xi_0$) [70], respectively. For superconductors with an anisotropic order parameter the orbital critical field H_{c2}^{orb} depends also on the direction of the magnetic field, therefore the range of the values of the coefficient n is wider in this case. As long as paramagnetic pairbreaking can be neglected, the anisotropy of H_{c2} of a superconductor in the clean limit represents the anisotropy of the Fermi surface and of the superconducting order parameter. However, at low temperatures the paramagnetic limiting, also known as Pauli limit, can influence dramatically the temperature dependence and anisotropy of H_{c2}. This coupling of the magnetic field to the electron spins described by a Zeeman term $-g\vec{H} \cdot \vec{\sigma}$ leads to paramagnetic pairbreaking. The Cooper pairs are brocken when the normal conducting state with the magnetic energy $\frac{1}{2\mu_0}(\chi_n - \chi_s)H^2$ is energetically more favorable than the superconducting state with the condensation energy $\frac{1}{2\mu_0}H_c^2$. χ_s and χ_n describe spin susceptibilities of the superconducting and the normal conducting phase, respectively. The Pauli limiting occurs in all superconductors with reduced χ_s compared to χ_n. The efficiency of the Pauli limiting depends significantly on the magnitude of the difference $\chi_n - \chi_s$. Therefore, beside the ratio χ_n/χ_s, which is known for a given order parameter, the magnitude of χ_n is very important. It is obvious that Pauli limiting achieves its maximum in states of even parity, since $\chi_s = 0$. The maximum critical field which a BCS superconductor would have in the absence of orbital interaction is given by [71]

$$H_{c2}^{P} = \frac{1.8 k_B T_c}{\mu_B}.$$

For triplet superconducting states with parallel aligned spins the spin susceptibility of the superconducting phase is equal to that of the normal conducting phase ($\chi_n = \chi_s$) because the rotation of the spin part of the order parameter is unrestricted with respect to the spatial part. Thus, there is no Pauli limiting for triplet superconductivity. However, in heavy fermion systems it is possible, that due to a strong spin-orbit interaction the alignment of the spin part of the order parameter is affected by the spatial part even in a spin triplet state. Moreover, if the orbital wavefunction is anisotropic due to the crystal symmetry, the paramagnetic pairbreaking becomes anisotropic as well ($\chi_s < \chi_s$ along certain crystallographic directions).
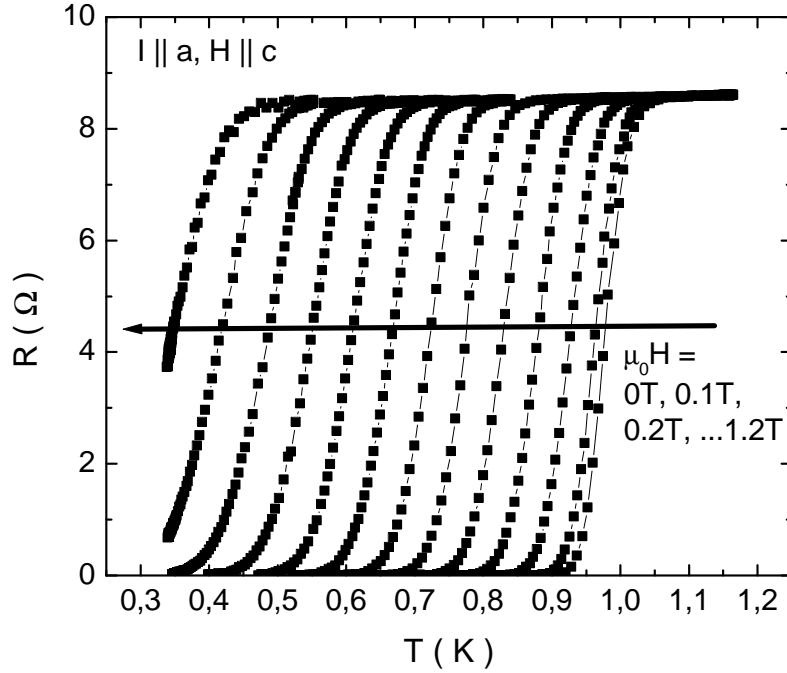
Figure 5.14: Resistive superconducting transitions of an UNi_2Al_3 thin film in magnetic fields $\mu_0 H$ from 0 T to 1.2 T. Probe current $I \parallel a$ and fields $H \parallel c$.

The measurements of the upper critical field of the UNi_2Al_3 thin films were performed in order to study the influence of the orbital and paramagnetic pair-breaking mechanisms on H_{c2} and to investigate the possible existence of a spin triplet state. The anisotropic features of H_{c2} were investigated by studding the temperature dependencies for different field and current directions.

The upper critical field $H_{c2}(T)$ of the UNi_2Al_3 thin films was determined by measuring resistive transitions $R(T)$ in different magnetic fields using a midpoint criterion. Fig. 5.14 shows the $R(T)$ curves obtained for probe currents $I \parallel a$ and field orientation $H \parallel c$ as an example. The width and shape of the transitions depend only weakly on the field H as opposed to the behavior reported from bulk single crystals [30]. The upper critical field was determined for field directions parallel to the real space a and c axis as well as parallel to the reciprocal a^* axis of the hexagonal compound each with $I \parallel a$ and $I \parallel c$ (Fig. 5.15).

For $H \parallel a^*$ the film plane was oriented perpendicular to the field direction, whereas for $H \parallel c$ the thin films had to be mounted with the film surface parallel
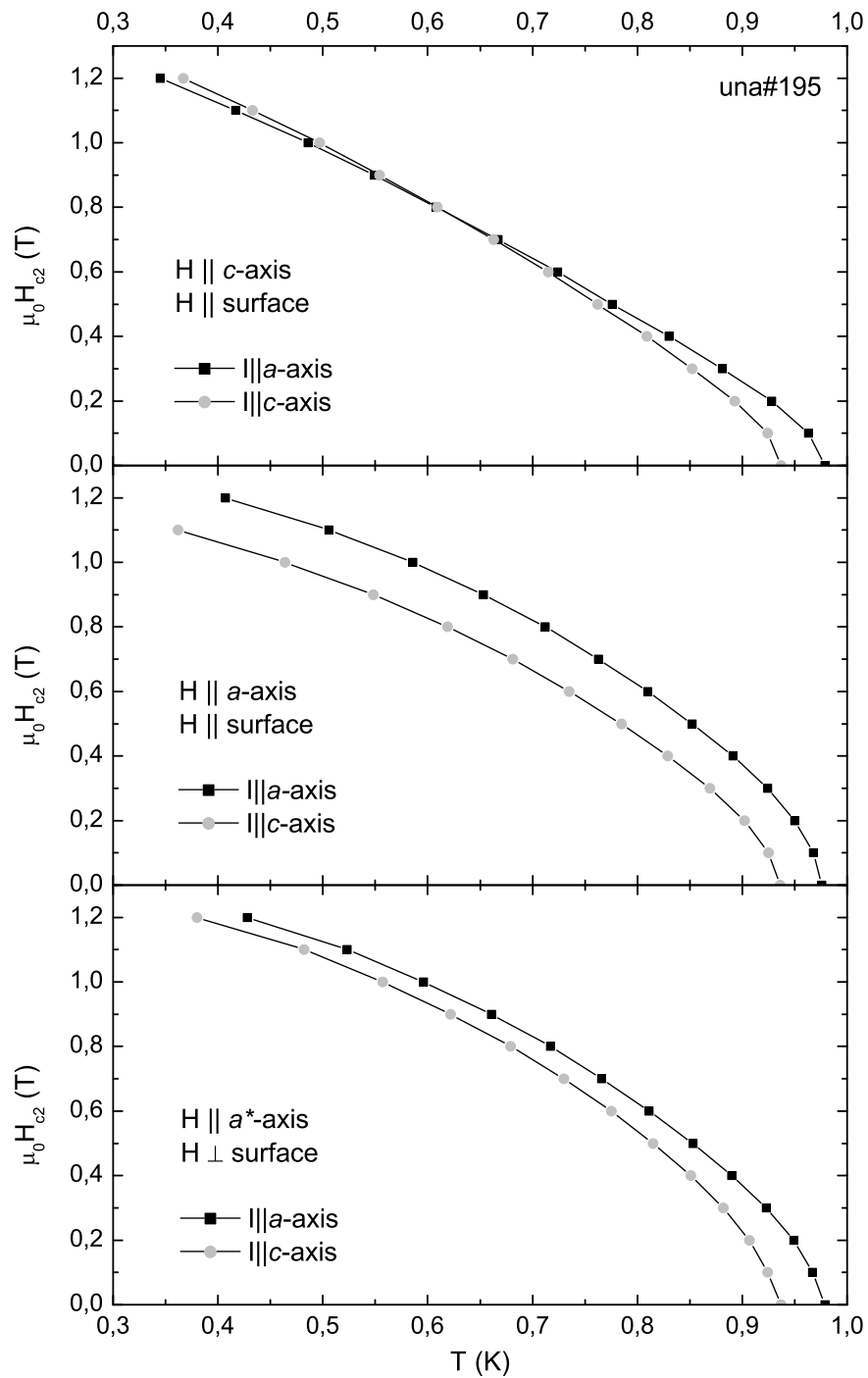
Figure 5.15: Upper critical fields $\mu_0H(T)$ of an UNi$_2$Al$_3$ thin film with different orientations relative to the field direction and different current directions relative to the crystallographic axis of UNi$_2$Al$_3$(see insets).
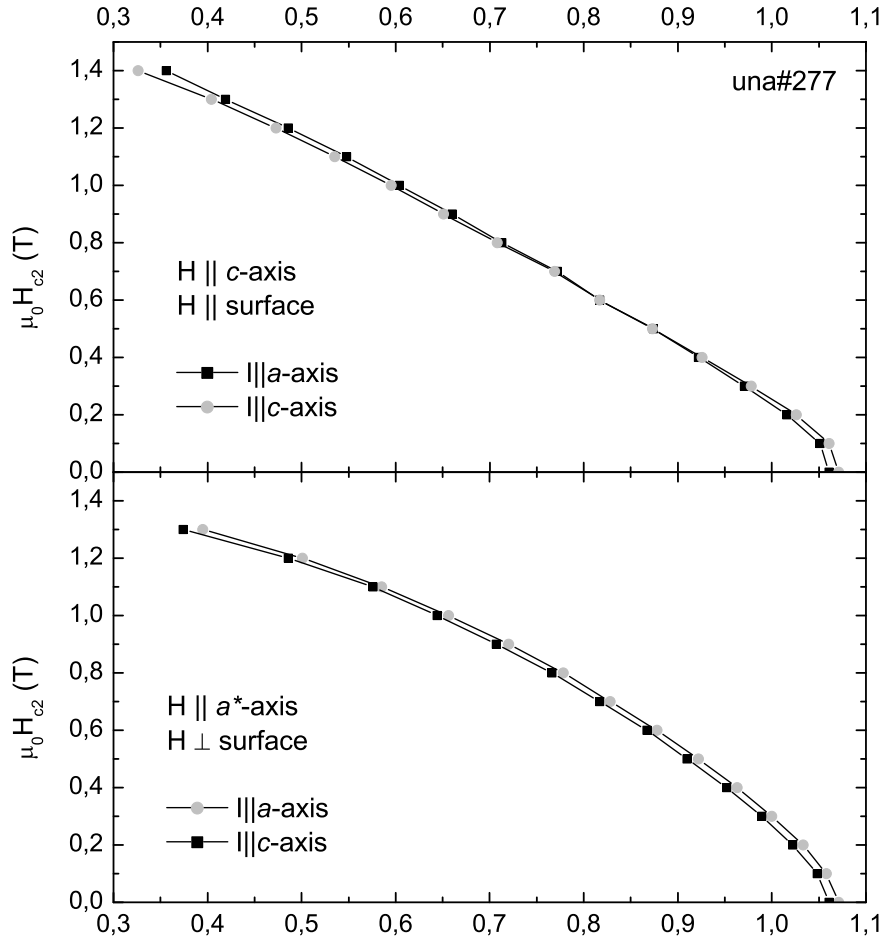
Figure 5.16: Upper critical fields $\mu_0 H(T)$ of an UNi$_2$Al$_3$ meander structure with different orientations relative to the field direction and different current directions relative to the crystallographic axis of UNi$_2$Al$_3$(see insets).

to the field direction. In principle the parallel configuration allows the appearance of increased critical fields due to finite size effects (thin film and surface superconductivity) [75]. However, these phenomena should result in a pronounced angular dependence of $H_c(\Theta)$ which was not observed. For additional investigation of these possible effects the film was rotated by 90° on the sample platform resulting in a configuration with $H \parallel a$ parallel to the film surface. Due to the hexagonal symmetry of UNi$_2$Al$_3$ only a very weak anisotropy of the critical field is expected within the ab plane. Thus the observation of very similar $H_{c2}(T)$ curves for $H \parallel a$ parallel to the film surface and for $H \parallel a^*$ perpendicular to the film surface shows that finite size effects do not influence the critical field.

The influence of the probe current direction on H_{c2} depends on the magnetic field direction. For $H \parallel a^*$ as well as for $H \parallel a$ qualitatively the same $H_{c2}(T)$ behavior is observed for $I \parallel a$ and $I \parallel c$ (shifted to lower temperatures). However, for $H \parallel c$ the two $H_{c2}(T)$ curves cross. Although T_c is smaller for $I \parallel c$, $H_{c2}(0.3\,\text{K})$ is slightly larger for this current direction at $H \parallel c$. Figures 5.15 and 5.16 show $H_{c2}(T)$ curves of two different samples. The qualitative influence of the current direction on the $H_{c2}(T)$ behavior is similar for all investigated thin films. However, the strength of the effect is varies from sample to sample proportionally to the difference of the critical temperatures for current directions $I \parallel a$ and $I \parallel c$. This dependence on the current direction provides additional evidence for multiband superconductivity in UNi_2Al_3 showing that there is no trivial explanation for the split of the superconducting transition.

For the thin films a steep slope $-\mu_0 H'_{c2}(T_c) > 5\,\text{T/K}$ was observed for all investigated magnetic field directions in contrast to the much smaller slopes reported previously from investigations of bulk polycrystals [72] and single crystals [30, 31]. Additionally, the critical fields of the thin films are much larger and exhibit different anisotropic behavior than reported for the best bulk single crystals [31] with $T_c \simeq 0.9\,\text{K}$. Employing the conventional WHHM-theory of the upper critical field, the authors of Ref.[31] concluded that orbital pair breaking limits H_{c2} of UNi_2Al_3 single crystal samples. With the same approach [69] an orbital upper critical field of $\mu_0 H_{c2}^{orb} > 3.5\,\text{T}$ can be calculated for the thin film samples. However, from the measured $H_{c2}(T)$ curves an upper critical field of only $\mu_0 H_{c2}(0K) \simeq 1.6\,\text{T}$ can be estimated. This discrepancy provides evidence for a non-negligible paramagnetic pair breaking contribution and thus a spin singlet superconducting order parameter of UNi_2Al_3 as opposed to the experimental evidence for spin triplet superconductivity of ref. [32], based on Al-Knight shift measurements. However, there is some doubt about the quality of the sample. The recent $H_{c2}(T)$ measurements on new high-quality (RRR $\simeq 40$) UNi_2Al_3 single crystal [31] reveal almost two times higher and much less anisotropic upper critical field than reported for the sample used for Knight shift measurements. Thus, alternative explanation for the observation of no Knight shift such as sample inhomogeneity is possible.

Additional conclusions concerning the order parameter symmetry can not be drawn from the $H_{c2}(T)$ measurements. For a realistic description a concept which goes beyond the WHHM theory considering the presumably multi-sheeted anisotropic Fermi surface and strongly anisotropic order parameter of UNi_2Al_3 is needed.

Chapter 6

Tunneling spectroscopy

Tunneling spectroscopy has proved to be a powerful tool for studying the properties of superconductors [73]. This experimental method makes it possible to investigate the density of states of the superconductor directly. Moreover, tunneling spectroscopy could provide information about order parameter symmetry and pairing mechanism of superconducting compounds. The first section of this chapter gives a short introduction to tunneling spectroscopy on superconductors. To perform a tunneling experiment one has first to prepare the tunnel junction. In the second sections of this chapter different techniques of planar tunnel junction preparation are described. The last section presents a survey of tunneling conductivity measurements on different junction types.

6.1   Introduction to tunneling spectroscopy

The experimental examination of the density of states of conductors by means of tunneling spectroscopy is based on the quantum mechanical property of the electron to pass through the energy barrier by a tunneling process provided it can find an empty state with the same energy on the other side of the barrier. This technique was pioneered by Giaever in 1960 [73], who used it to confirm the prediction of the Bardeen-Cooper-Schrieffer theory (BCS) concerning the density of states and temperature dependence of the energy gap of conventional superconductors [74].

A simple tunneling experiment can be performed on a sample consisting of two conductors separated by a thin layer of an insulator (Figure 6.1). In the case when both conductors are normal metals, the simple model assuming constant
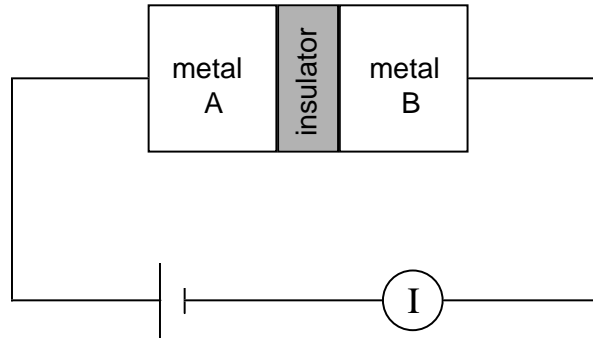
Figure 6.1: Schematic of a tunneling experiment.

densities of states at the Fermi energy can be used. At $T = 0\,\mathrm{K}$, all states in both metals are filled below the Fermi level and are empty above it; for $T > 0\,\mathrm{K}$, the thermal excitations smear out the occupied states in a small region around the Fermi energy of width $\propto k_B T$. In Figure 6.2 the energy diagram of a normal conductor–insulator–normal conductor (NIN) junction at $T = 0\,\mathrm{K}$ is shown. Since the metals are in contact, the Fermi energies are at the same level (Figure 6.2a). The conduction electrons on both sides of the junction are in thermodynamic equilibrium and no transport current flows through the junction. Now, if a voltage
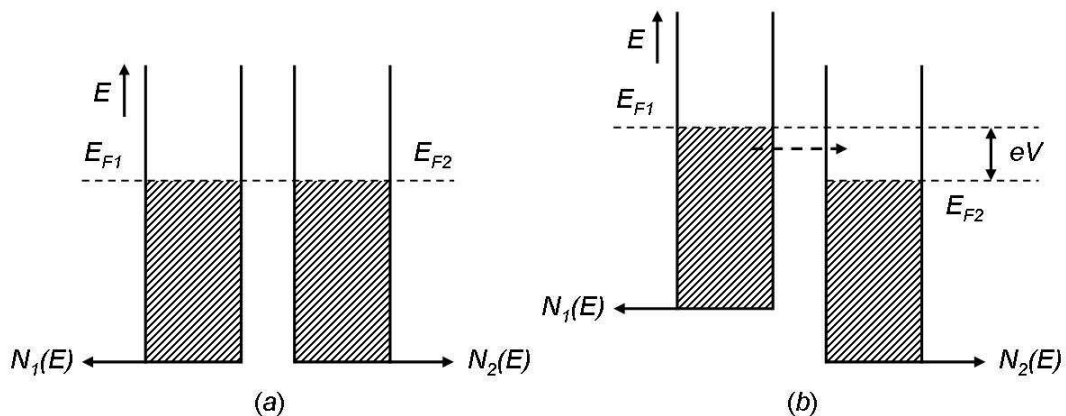
Figure 6.2: Illustration of the tunneling process between two normal metals at $T = 0\,\mathrm{K}$: $a)$ $V = 0$, all electron states below Fermi levels are occupied, tunneling is not possible; $b)$ $V \neq 0$, the tunneling current is proportional to applied voltage $\propto eV$.

V is applied across the barrier, the Fermi levels are separated by an energy eV (Figure 6.2b) and a tunneling current can be measured. Assuming that in a region near the Fermi energy the density of states remains constant, the tunneling current will be proportional to the applied voltage.

A simple theoretical description of a tunneling process is based on perturbation theory assuming the electrodes to be only weakly coupled [75]. The Hamilton operator for the quasi-particle tunneling from state $\mathbf{k}$ of one electrode in the state $\mathbf{q}$ of the other electrode (σ: spin index) reads in second quantization:

$$\mathcal{H}_T = \sum_{\sigma \mathbf{kq}} T_{\mathbf{kq}} c^+_{\mathbf{k}\sigma} c_{\mathbf{q}\sigma} + h.c.$$

with the phenomenological tunneling matrix element $T_{\mathbf{kq}}$ which includes the barrier properties.

In order to describe the transfer of an electron into a $\mathbf{k} \uparrow$ state of a superconductor, the electron states have to be reexpressed in terms of the appropriate quasi-particle excitations $\gamma_{e\mathbf{k}s}$ and $\gamma_{h\mathbf{k}s}$ of the superconductor:

$$c^+_{\mathbf{k}\uparrow} = u_{\mathbf{k}} \gamma^+_{e\mathbf{k}0} + v^+_{\mathbf{k}} \gamma_{h\mathbf{k}1}$$

From symmetry considerations it can be shown that the characteristic coherence factors of the superconducting wave function, $u_{\mathbf{k}}$ and $v_{\mathbf{k}}$, drop out [75]. Since the coherence factors disappear and, as a consequence, the tunneling current depends only on the density of states, the so called semiconductor model can be introduced to illustrate the tunneling process. In this model the normal metal is represented in the same way like it was described for a NIN-junction. The superconductor is represented by an ordinary semiconductor with independent-particle energy states which correspond to the density of state of the superconducting quasi-particle excitations. Such a density of state will reduce properly to the normal-metal density of states as $\Delta \to 0$. In Figure 6.3 the tunneling process between a normal-metal and a superconductor is illustrated.

Within the independent-particle approximation the tunneling current is proportional to an energy integral over the product of the density of occupied states of one electrode times the density of empty states of the other electrode and can be written as:

$$I = \text{const } |T|^2 \int_{-\infty}^{\infty} N_1(E) N_2(E + eV)[f(E) - f(E + eV)] dE \qquad (6.1)$$

Figure 6.3: Illustration of a normal conductor–insulator–superconductor tunneling process in the so called semiconductor description. The density of states is plotted horizontally versus energy vertically; occupied electron states are shaded ($T = 0\,\mathrm{K}$). a) The difference of the contact potentials equalizes the Fermi energy of the normal metal and ground state energy of the superconductor. For bias voltages $eV < \Delta$ no tunneling current is possible. b) The bias voltage $eV = E_{F1} - E_{F2}$ slightly exceeds the energy gap Δ. The horizontal arrow represents electrons tunneling from occupied states in the left into empty states in the right electrode.

with the appropriate equations of the densities of states $N_1(E)$ and $N_2(E)$, applied voltage V and Fermi-Dirac distribution function $f(E)$. In this expression the tunneling matrix element $T_{\mathbf{kq}}$ is assumed to be a constant.

For a superconductor–insulator–normal metal (SIN) tunnel junction equation (6.1) becomes

$$I(V)_{SIN} \propto \int_{-\infty}^{\infty} dE \frac{|E|}{\sqrt{E^2 - \Delta^2}} \left(f(E) - f(E + eV) \right)$$

where Δ is the energy gap of a superconductor. Finally, the differential conductivity normalized to the normal conductor–insulator–normal conductor (NIN) conductivity is directly proportional to the superconducting density of states [75] (for $T \to 0\,\mathrm{K}$):

$$\left(\frac{dI}{dV} \right)_{SIN} = \left(\frac{dI}{dV} \right)_{NIN} \int_{-\infty}^{\infty} dE \frac{|E|}{\sqrt{E^2 - \Delta^2}} \left(-f'(E + eV) \right)$$

As shown in Figure 6.3, at $T = 0\,\mathrm{K}$, there is no current until $e|V| \geq \Delta$, since there are no available states for the electrons in the superconducting gap. The

magnitude of the current is symmetric with respect to zero bias because hole and electron excitations have the same energies. For $T > 0\,\mathrm{K}$ the excited states are already partially filled, allowing electrons to tunnel at lower energies.

In the case of a superconductor-insulator-superconductor (SIS) junction the energy integral (6.1) has to be taken over both superconducting densities of states [75]. However, the tunneling process in a SIS junction can be also discussed qualitatively within the energy diagram. In Figure 6.4 the energy level structure of a SIS junction is shown.
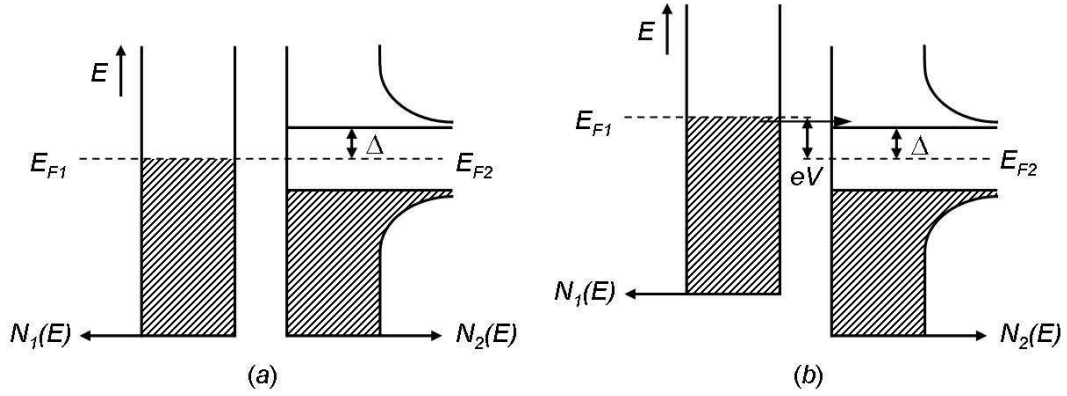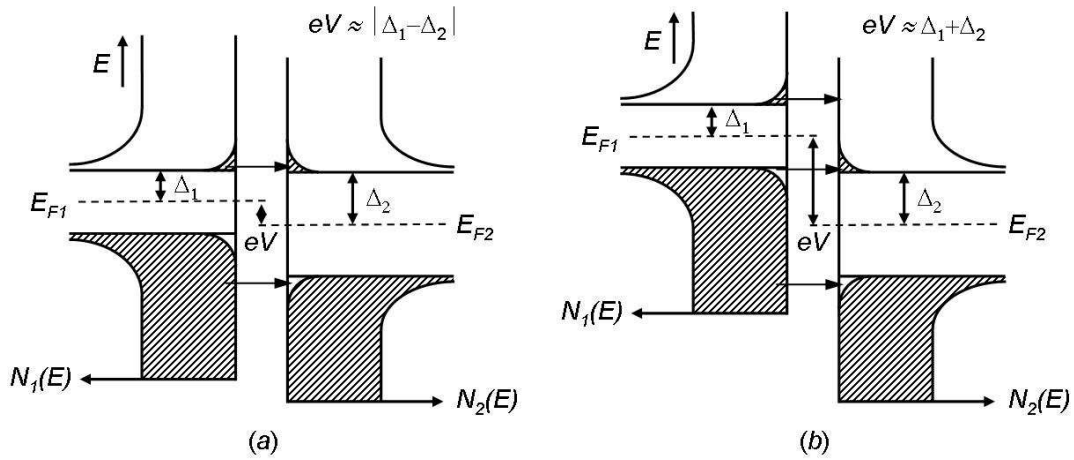

Figure 6.4: Illustration of a superconductor–insulator–superconductor tunneling process in the semiconductor model. The density of states is plotted horizontally versus energy vertically; occupied electron states are shaded ($T = 0\,\mathrm{K}$). The horizontal arrow represents electrons tunneling from occupied states in the left into empty states in the right electrode. The bias voltage $eV = \mu_1 - \mu_2$ slightly exceeds the energy gap Δ.

At $T = 0\,\mathrm{K}$ no current can flow through the junction until $eV = \Delta_1 + \Delta_2$, since all available states in both superconductors are occupied. At $T > 0\,\mathrm{K}$ the thermally excited quasi-particles provide the current flow also at lower voltages but there is additional enhanced contribution to the current at $eV = |\Delta_1 - \Delta_2|$ (Figure 6.4a), corresponding to the tunneling of thermally excited quasi-particles from the peak of the density of states at Δ_1 into the peaked density of available states at Δ_2.

The simple treatment of the tunneling processes described above assumes certain conditions of the junction: both electrodes are in a stable thermodynamic equilibrium and are separated by the ideal insulator with sufficiently high barrier

potential, which keeps the amount of tunneling charge carriers small. Experimentally it is very difficult to prepare a tunneling junction with ideal barrier properties. The theory proposed by Blonder, Tinkham and Klapwijk (BTK-theory) is able to describe transport through a barrier with variable transmission and reflection coefficient [74]. This theory covers the complete crossover from metallic to tunnel junction behavior of the contact.

The BCS-model prediction of the superconducting density of states is in perfect agreement with the tunneling spectroscopic results on conventional weak-coupling superconductors like Al, Sn and In, for example. However, for strong coupling superconductors like Pg, Hg and In measurements of the differential conductivities show clear deviations from the BCS-behavior. Although these deviations are small compared to the large peak in the conductivity at Δ, they result in changes in the conductance of up to some percent (5% for Pb) over rather small energy ranges. Giaever et al. noticed first that there are small bumps in the tunneling conductivity curves of a Mg–MgO–Pb junction. The total energy range of these structures is suggestively close to the Debye energy, which is characteristic of a phonon structure. As Schrieffer, Scalapino and Wilkins have shown, the observed density of states can be explained by considering the complex and energy dependent gap parameter $\Delta(E)$. In order to produce an energy dependent $\Delta(E)$, a more realistic superconducting pairing interaction than in BCS-model has to be assumed. The simple BCS approximation of an energy independent attractive pairing potential V suppresses the details of the interaction, but the more exact Eliashberg theory accounts for the strong-coupling features.

The Eliashberg theory considers the Cooper-pair formation processes of emission and absorption of virtual boson (not necessary phonons) in the framework of quantum field theory. The correction of the energy necessary to add an electron to the Fermi sea results in a self-consistent equation for a complex gap function $\Delta(\omega, T)$, which depends on the phonon density of states $F(\omega)$ and an effective electron-phonon coupling function $\alpha^2(\omega)$, both as functions of energy. In Figure 6.5 the numerically calculated Eliashberg density of states for two boson modes together with the density of states in Pb determined by tunneling are shown [76]. The phonon density of states, used in the calculation, agrees well with the Pb phonon spectrum determinated by inelastic neutron scattering [77]. This is strong evidence that the phonon exchange between the charge carriers is responsible for superconductivity in conventional superconductors.
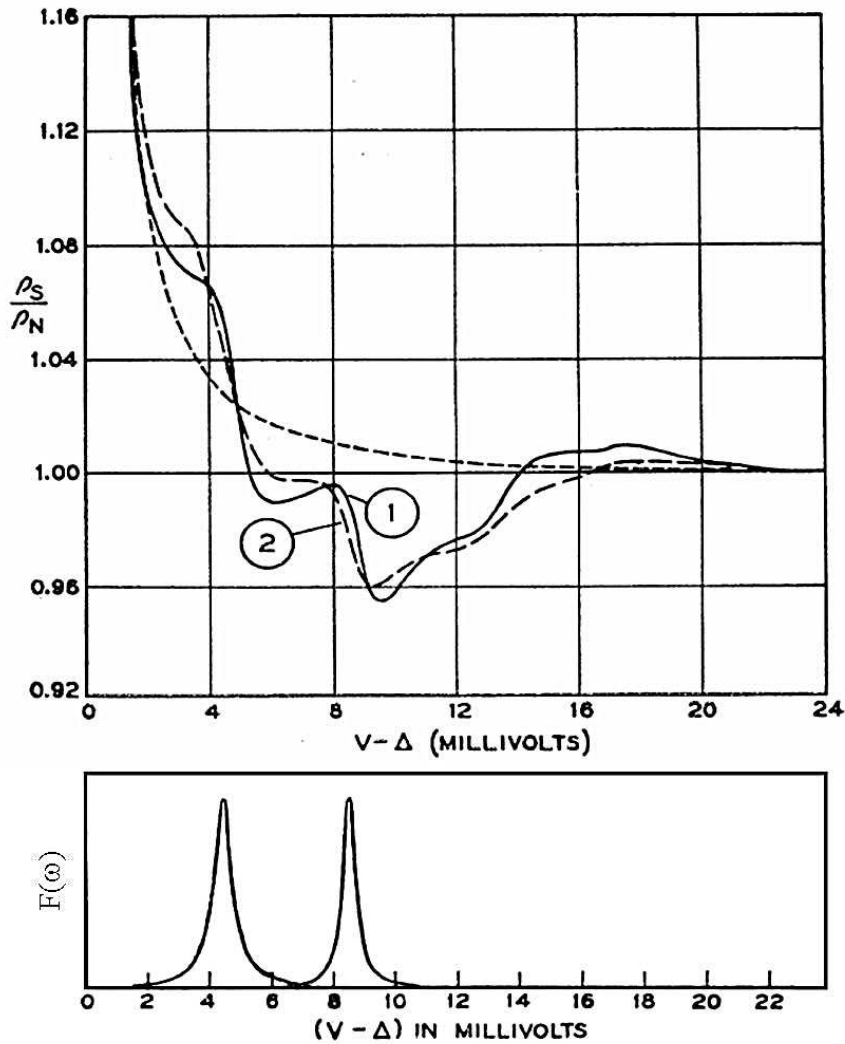
Figure 6.5: Comparison of calculated (1) and experimental (2) density of states of lead. The lower panel shows the phonon density of Pd used in the calculation. *Adapted from J. M. Rowell and L. Kopf [76].*

6.2 Planar tunneling junctions

From all available experimental methods tunneling spectroscopy provides the most direct information of the superconducting density of states. The opportunity to gain knowledge about the presumably unconventional order parameter symmetry and mechanism of the pairing interaction in heavy fermion superconductors motivates tunneling experiments on these compounds. However, many

attempts to investigate the superconducting state of heavy fermions by standard point or break junction spectroscopy were not successful, generally, due to disturbed superconductivity in the surface region of the investigated samples. From the sample quality point of view this problem can be overcome by in-vacuo preparation of planar Giaever-type junctions based on thin film samples with high crystalline purity even in the surface region. Recently, using this technique it was possible to prepare $UPd_2Al_3-AlO_x-Pb$ junctions and to investigate the superconducting properties of UPd_2Al_3 by means of tunneling spectroscopy [15]. The observation of a strong-coupling feature in the tunneling conductivity together with inelastic neutron scattering data provide strong evidence that the pairing interaction in this compound is mediated by magnetic excitations. From this point of view, the preparation of tunnel junctions based on UNi_2Al_3 thin films is of a great interest.

6.2.1   Concept of the preparation

The Giavier-type junction consists of two planar electrodes separated by a small distance of the order of some atom layers. The realization of this very thin but precise flat and uniform tunneling barrier is probably the most crucial point and definitely the major problem of junction preparation. In practice a tunneling barrier is created by fabrication of an insulating layer between the tunneling electrodes. During his tunneling experiments on different materials I. Giaever found, that some metals like Al, Ni, Sn, Pb, etc. form a good insulating surface oxide. Therefore, these metals can be deposited as a base electrode and then simply oxidized in air before the counter electrode is evaporated on top [78, 79]. However, this simple method has the disadvantage of poor reproducibility, since, as I. Giaever wrote: *the forming of thin oxide films tends to be more an art than a science.* For better results the complete junction preparation process should be performed in a vacuum chamber and the oxidation should be done in pure oxygen instead of air [80].

However, there are many materials which do not form a good native surface oxide. In this case an artificial insulating barrier has to be prepared. It can be done, for example, by depositing on top of the base electrode a very thin film of Al and its subsequent complete oxidation. For the first time this technique was demonstrated for $Nb-AlO_x-Nb$ tunnel junctions [81]. It is used now to prepare junctions for technical applications [82, 83, 84] as well as for investigations of

the superconducting order parameter of different materials [85, 15]. In order to obtain a good artificial barrier, two main demands have to be met. First of all, the base electrode has to be covered with the barrier material completely without pinholes. Secondly, the whole of the barrier material has to become an oxide but the base electrode should not be affected by the oxidation process. Figure 6.6 represents schematically a situation with possible barrier defects, which occur when the required conditions are ignored.
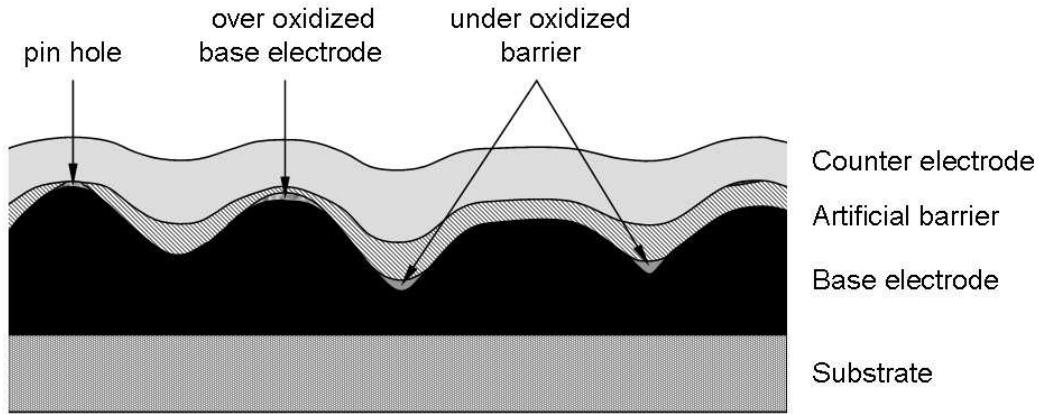
Figure 6.6: Schematic of a cross section of the interface region with the possible barrier defects.

6.2.2 UNi$_2$Al$_3$-based junctions

UNi$_2$Al$_3$–AlO$_x$–(Ge)–Pb junctions

First planar junctions with UNi$_2$Al$_3$ were prepared by the technique developed for UPd$_2$Al$_3$–AlO$_x$–(Ge)–Pb tunneling contacts [29]. All preparation steps were performed in situ without breaking the vacuum. After the deposition of a UNi$_2$Al$_3$ thin film and cooling the substrate down to 100° C a thin layer ($d \approx 4\,\text{nm}$ - $6\,\text{nm}$) of Al was sputtered (or thermally evaporated) on the top. Then the sample was transfered in another chamber where the artificial insulating barrier was formed by oxidizing Al in a glow discharge. In order to obtain a four terminal geometry insulating material was thermally evaporated employing a shadow-mask technique. The whole film was covered with $200\,\text{nm}$ of amorphous Ge except a narrow stripe of width $b = 0.5\,\text{mm}$ in the center of the sample. The counter electrode consisting of $200\,\text{nm}$ of Pb was also thermally evaporated with a shadow mask defining

three stripes of width 0.15 mm, 0.25 mm, and 0.35 mm. The preparation steps and the final geometry of the single UNi_2Al_3-AlO_x–(Ge)–Pb junction are shown in Figure 6.7.
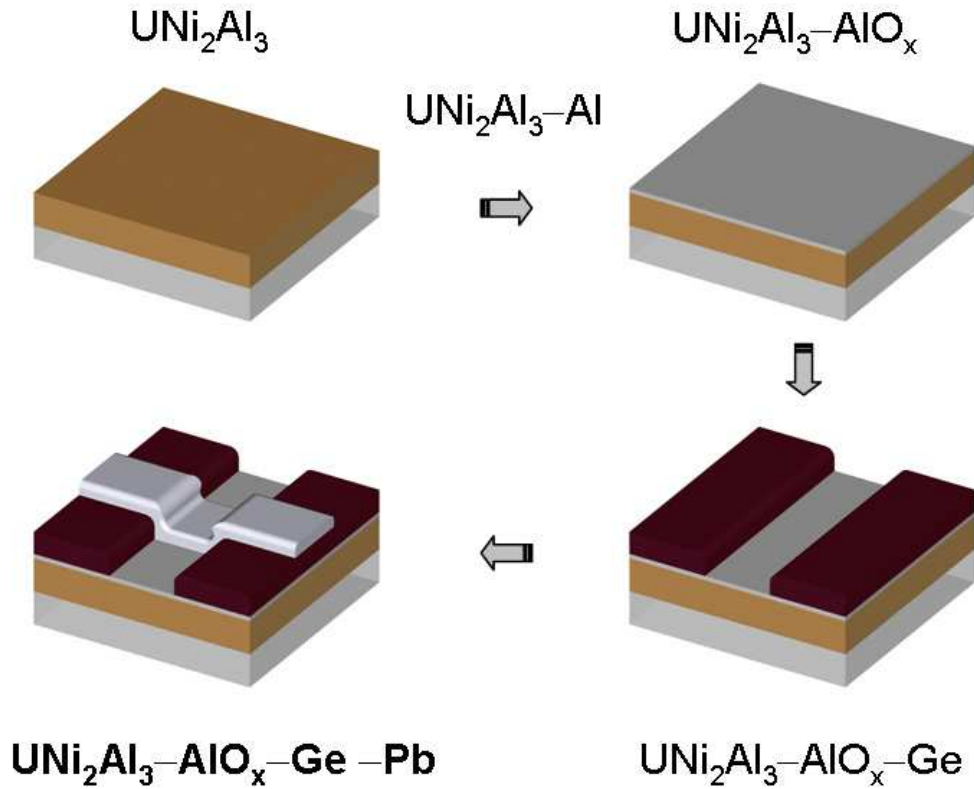
Figure 6.7: Schematic of the preparation steps of UNi_2Al_3–AlO_x–(Ge)–Pb planar tunnel junctions.

UNi_2Al_3–AlO_x–Pb cross-type junctions

Although the method described in the previous section was successfully used for the preparation of tunnel junctions based on UPd_2Al_3, the UNi_2Al_3–AlO_x–(Ge)–Pb junctions reveal pure reproducibility due to frequent short circuits between base and counter electrodes through the Ge insulating layer. To avoid this problem junctions without insulating Ge layer were prepared using an alternative shadow-mask technique for the deposition of the UNi_2Al_3 base electrode. After the deposition of a narrow stripe of UNi_2Al_3 film of width $b \approx 0.5$ mm a thin layer of Al was evaporated on the top and oxidized. Finally, through a shadow mask

the Pb counter electrode was evaporated. In Figure 6.8 the preparation steps and the final geometry of the single UNi_2Al_3–AlO_x–Pb cross-junction are shown.
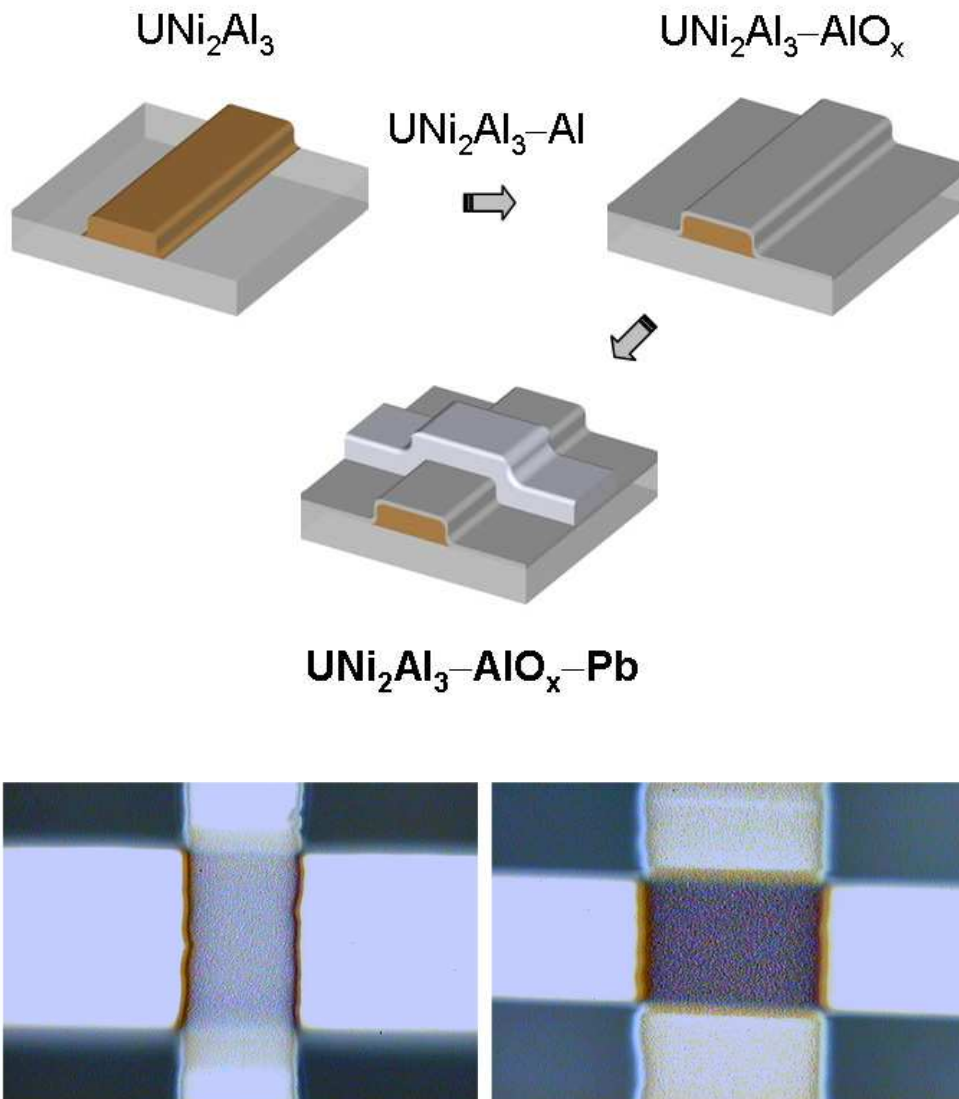
Figure 6.8: Schematic of the preparation steps and photograph (phase-contrast optical microspope) of a UNi_2Al_3–AlO_x–Pb planar cross-type junction.

However, there are principle problems due to the deposition of the narrow stripe of UNi_2Al_3 employing a shadow-mask, which cannot be completely eliminated. As the elements are evaporated out of three different electron beam evaporators, placed at a distance from each other, changes in the stoichiometry

of the films at the structure edges due to the use of a shadow mask, placed at
a final distance from the substrate, cannot be avoided. The half-shadow effect
can be reduced by decreasing the distance between the substrate and the shadow
mask. On the other hand, at very short distances the heat radiation shielding by
the mask becomes significant, leading to a temperature gradient in the film and,
as a consequence, to quality inhomogeneity.

UNi_2Al_3–AlO_x–Ag mesa-junctions

In the framework of this project, the following process was developed. In order to
eliminate the necessity of using shadow masks for the deposition of the UNi_2Al_3
base electrode mesa-junctions were prepared involving a standard photolithog-
raphy technique. The preparation process of all junction layers was performed
completely in vacuo as before. After the deposition of UNi_2Al_3 and the creation
of the AlO_x insulating barrier, 200 nm of Ag were sputtered on top, produc-
ing a UNi_2Al_3–AlO_x–Ag junction on the whole substrate area. A silver counter
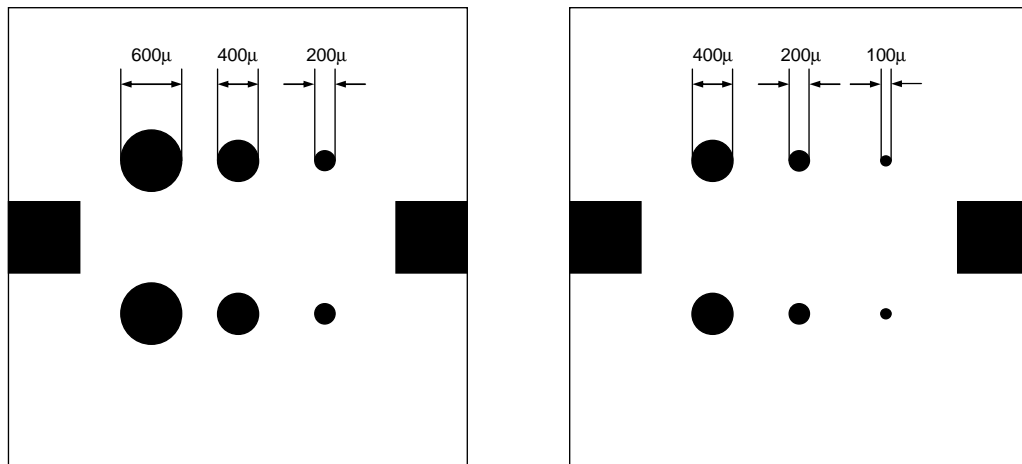
Figure 6.9: Schematic of *mesa* (left) and *window* (right) photomasks used for the
preparation of the mesa-junctions. Black areas are not transparent to the UV light.

was exposed to air and transfered to the clean room for further photolithography
treatment. There the sample was covered with a positive photoresist and exposed
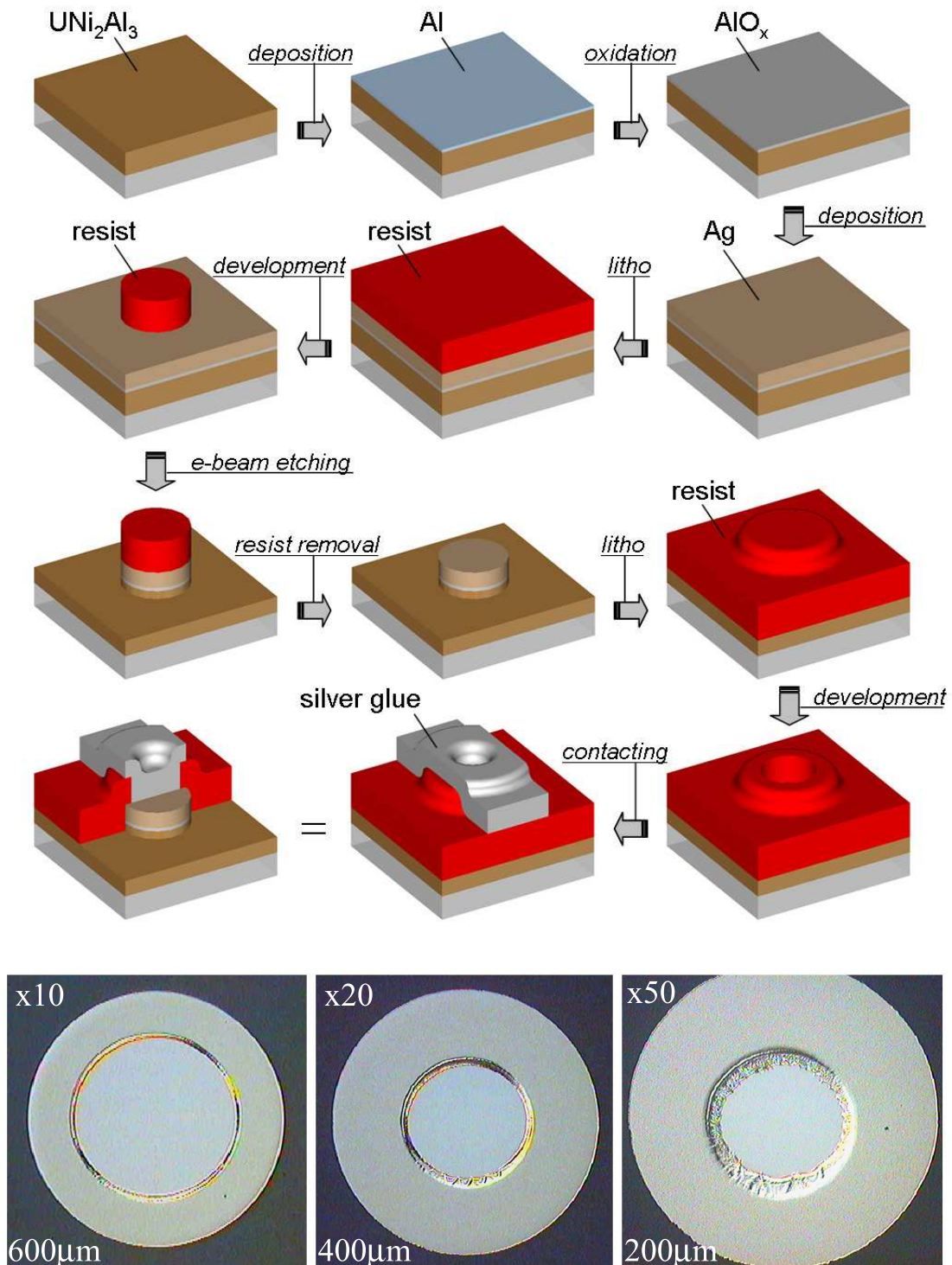
Figure 6.10: Schematic of the preparation steps of UNi$_2$Al$_3$–AlO$_x$–Ag mesa-junctions and photograph (phase-contrast optical microspope) of the structure with the opened contact windows.

to ultraviolet (UV) light under a mesa photomask, which shadowed six junction spots of diameter 100μm, 200μm and 400μm as well as ground electrode contact areas (Figure 6.9). Then the exposed photoresist was selectively removed in a wet developer. After that the sample was etched by an ion beam, so that the silver counter electrode was completely removed from the surface except on the areas, which were protected by the photoresist. After ion beam etching the rest of the potoresist was completely removed by acetone and the sample was covered again with a negative photoresist in order to insulate the UNi$_2$Al$_3$ ground electrode. Then the sample was again exposed to UV light under a window photomask (Figure 6.9). This mask opens ground electrode contacts and six spots of diameter 50μm, 100μm and 200μm at the centers of the mesa towers. The mechanical and insulating properties of the resist were additionally strengthened by a *hard bake* process. After that the connections to the Ag counter electrode at the top of the mesa structures and to the UNi$_2$Al$_3$ base electrode were opened by a wet developer. Finally, the electrodes were contacted through the *windows* by silver glue. The preparation steps and the final geometry of a single UNi$_2$Al$_3$–AlO$_x$–Ag mesa-junction as well as a photograph of mesa structures are shown in Figure 6.10. Details of the lithographic part of the mesa-junction preparation process are described elsewhere [86].

6.3   Measurement technique

The measurements of the tunneling conductivity were performed employing an ac-modulation technique. Additionally to a dc-current I_0 an ac-component $\hat{I}\sin(\omega t)$ flows through the junction and the dc-voltage V_{dc} as well as the ac-voltage V_{ac} of the resulting voltage drop are measured separately. Since

$$V(I_0 + \hat{I}\sin(\omega t)) = V_{dc} + V_{ac} + ... = V(I_0) + \left.\frac{\partial V}{\partial I}\right|_{I_0} \hat{I}\sin(\omega t) + ...$$

the inverse of the ac-voltage is directly proportional to the tunneling conductivity.

The measurements presented in this thesis were performed by the ac-modulation set-up shown in Fig. 6.11. The tunnel junctions were mounted in a top-loading ^{3}He-cryostat (*Oxford Instruments, Kelvinox TLM*). The contacts were bonded using silver paint. The junction current was generated by employing a Lock-In amplifier (*Stanford Research Systems SRS-830*). An ac-modulated current output was obtained by connecting two resistors of variable resistance R_{dc} and R_{ac}
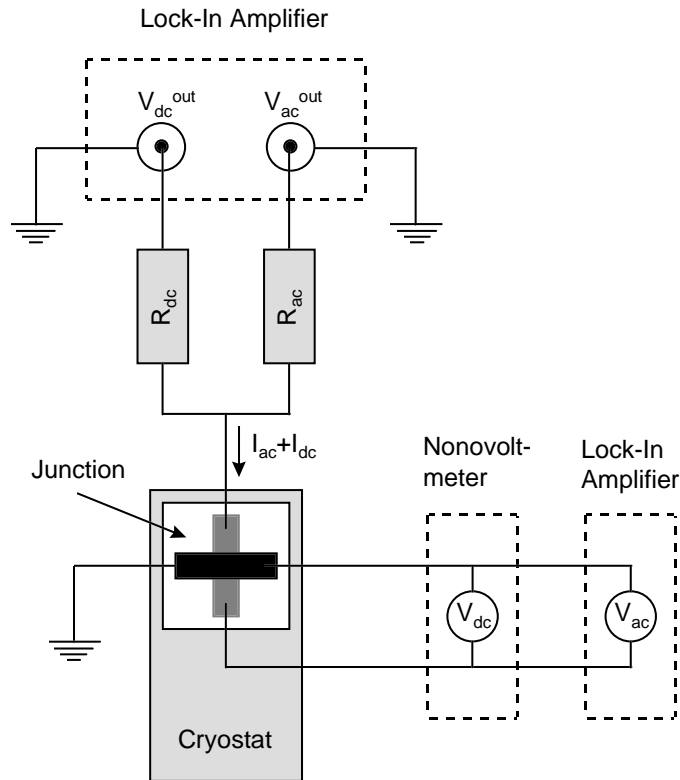
Figure 6.11: Schematic of the ac-modulation set-up used for the measurement of the tunneling differential conductivity. (Courtesy of M. Jourdan)

much larger than the junction resistance to the dc- and ac-voltage outputs of the Lock-In amplifier. For the measurement of the dc- and ac-voltage drop across the junction a nanovoltmeter (*Keithley 181*) and a Lock-In amplifier (*SRS 830*) input were connected to the junction in parallel.

6.4 Tunneling conductivity measurements

6.4.1 UNi$_2$Al$_3$–AlO$_x$–(Ge)–Pb junctions

Despite frequent problems with the insulating properties of the Ge layer it was possible to prepare UNi$_2$Al$_3$–AlO$_x$–(Ge)–Pb junctions which were in a clearly demonstrated tunneling regime at low temperatures. The zero bias conductivity of these junctions revealed only a weak temperature dependence indicating

pinhole-free barriers consisting of insulating material. The resistances of the
UNi_2Al_3–AlO_x–(Ge)–Pb junctions are estimated to $\rho_A \simeq 21\Omega mm^2$ for a bar-
rier thickness of $d \simeq 6nm$. At temperatures below the superconducting crit-
ical temperature of the counter electrode T_c^{Pb}, but above T_c of UNi_2Al_3 (SIN
regime) the typical tunneling density of states of superconducting Pb including
strong coupling-features was observed, proving the contacts to be in the tunneling
regime.
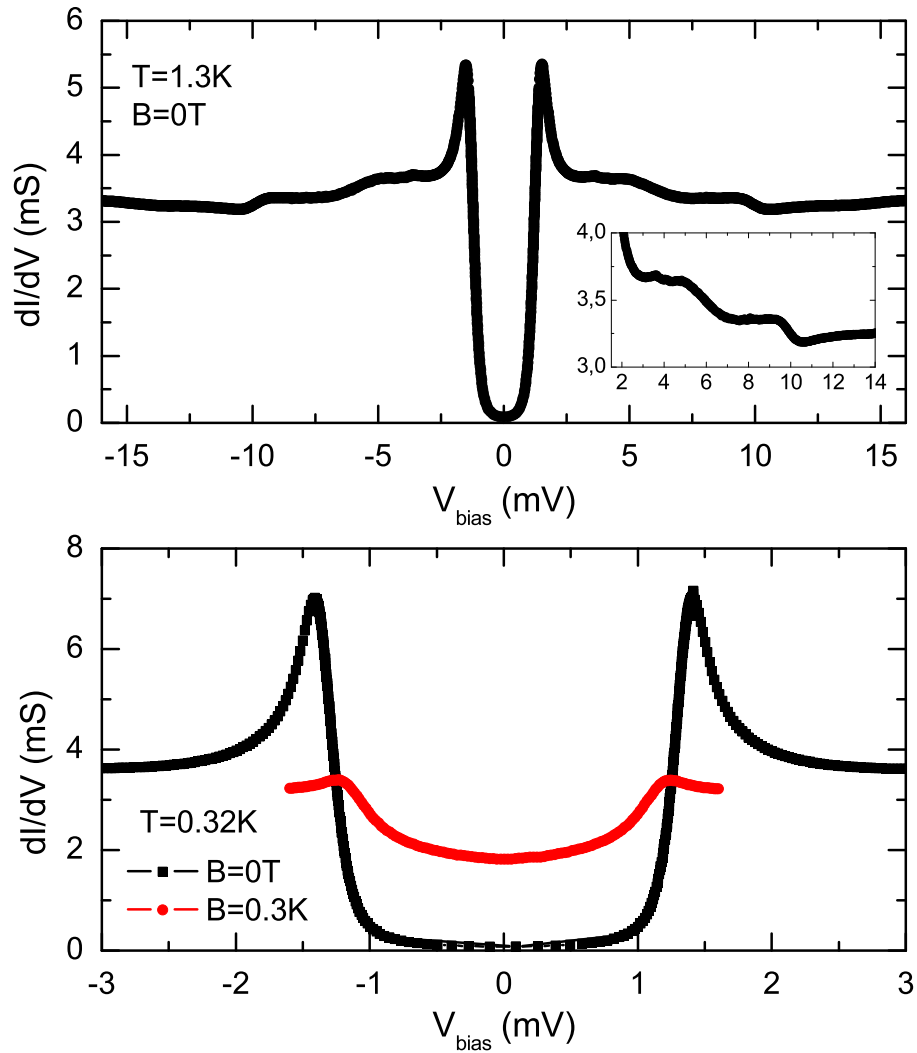
Figure 6.12: Differential conductivity of an UNi_2Al_3–AlO_x–(Ge)–Pb junction.
Upper panel: Tunneling density of states of the Pb counter electrode.
Lower panel (b): Magnetic field dependent conductivity of a junction at $T = 0.32\,K$.
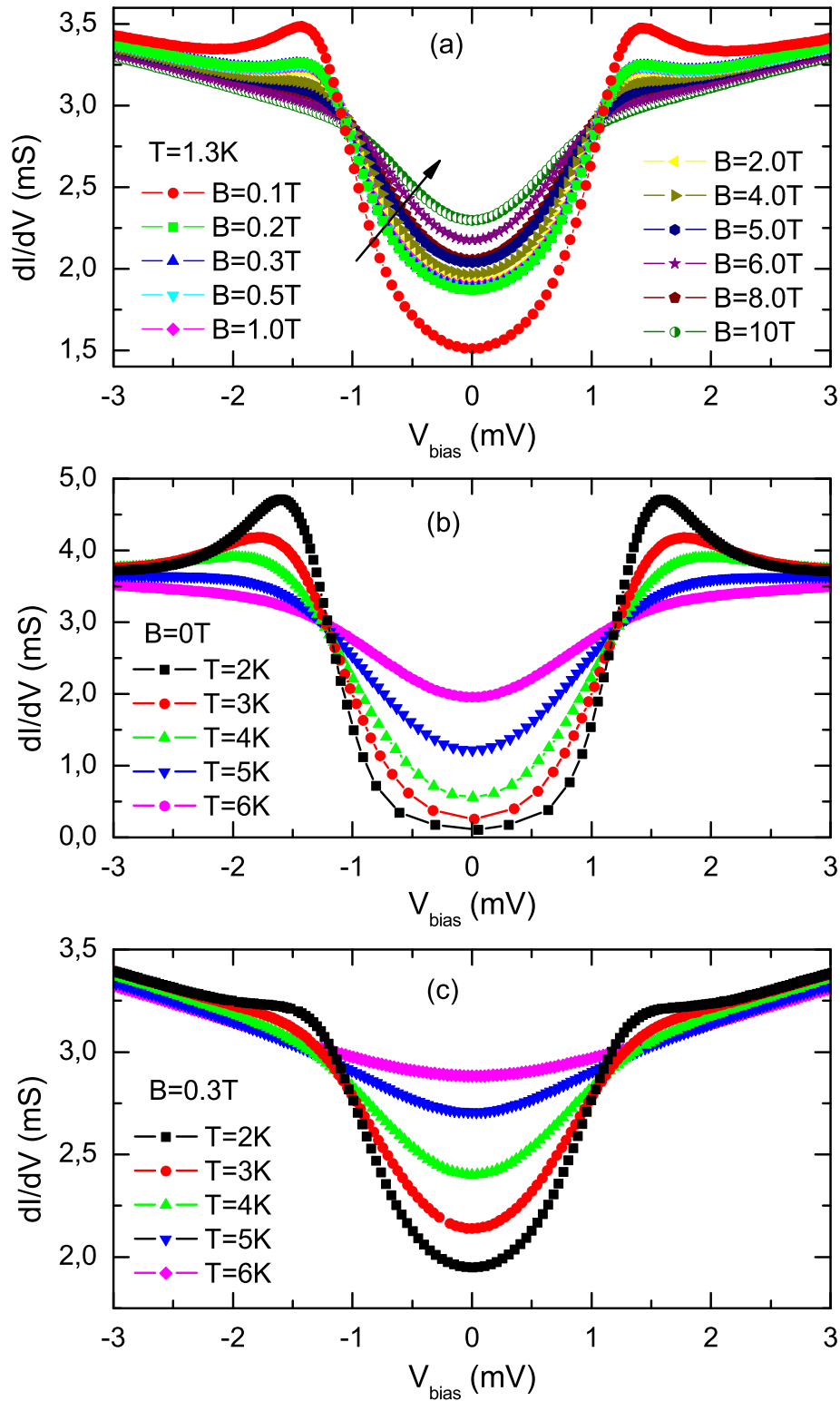
Figure 6.13: Temperature and magnetic field dependences of Pb gap features in UNi$_2$Al$_3$–AlO$_x$–(Ge)–Pb junction conductivity. Panel (a): Differential conductivity of a junction in various magnetic fields at $T = 1.3$ K. Panel (b): Temperature dependent conductivity of a junction in zero magnetic field. Panel (c): Differential conductivity of a junction for various temperatures in a magnetic field of $\mu_0 H = 0.3$ T.

In the upper panel of Figure 6.12 the tunneling density of states of the Pb counter electrode at $T = 1.3\,\mathrm{K}$ is presented. BCS-calculation of the thermally smeared superconducting density of states fits perfectly the junction conductivity in the gap region; only a small barrier leakage conductivity $\sigma_l = 0.09\,\mathrm{mS}$ ($3\,\%$ of the total barrier conductivity) had to be added as a background. The typical phononic strong coupling features are clearly shown in the inset of upper panel.

Below the superconducting critical temperature of the base electrode, the junctions are expected to be in the superconductor-insulator-superconductor (SIS) regime. Due to an opening of the superconducting energy gap of UNi_2Al_3 additional conductivity features as well as a reduction of the low bias conductivity are expected. Applying a magnetic field overcritical for Pb, but not for UNi_2Al_3, the superconductivity of the counter electrode should be suppressed, and the influence of the density of states of the base electrode should be directly observable. However, none of the features which could be associated with the UNi_2Al_3 superconducting gap was observed (Figure 6.12 lower panel), only the Pb gap structure is visible even in a magnetic field of $\mu_0 H = 0.3\,\mathrm{T}$.

Moreover, as shown in Figure 6.13, panel (a), a gap like structure, which could be associated with superconductivity of the counter electrode is visible in the differential conductivity of the junction at $T = 1.3\,\mathrm{K}$ in magnetic fields much higher than the upper critical field of bulk Pb. The reduced low bias conductivity was observed in an external magnetic field up to $\mu_0 H = 10\,\mathrm{T}$. Panel (b) and (c) of Figure 6.13 show the temperature dependences of the junction conductivity in a zero magnetic field and in a magnetic field of $\mu_0 H = 0.3\,\mathrm{T}$, respectively. It is evident, that the gap like structure is induced by superconductivity of the counter electrode, since it disappears above T_c of Pb. The enhancement of the upper critical field of Pb could be explained by a high concentration of non-magnetic impurities in the counter electrode. These impurities could be produced by the oxidation of Pb as well by an interaction of Pb and AlO_x at the barrier–counter electrode interface during the deposition process.

6.4.2 UNi_2Al_3–AlO_x–Pb cross-type junctions

Measurements of the contact resistances of UNi_2Al_3–AlO_x–Pb cross-type junctions above T_c^{Pb} of the counter electrode showed only a weak temperature dependence. The contact resistance continuously increased by a factor of 2 with decreasing temperature from $300\,\mathrm{K}$ to $7\,\mathrm{K}$. This temperature dependence indi-

cates a pinhole-free barrier consisting of an insulating material.

In Figure 6.14 the differential conductivities of a UNi_2Al_3–AlO_x–Pb cross-junction at various temperatures and in various external magnetic fields are shown. In zero magnetic field the typical tunneling density of states of superconducting Pb including strong coupling-features is clearly observed at $T = 1.3\,K$ (panel (a)), demonstrating the tunneling regime of the contact. In panel (b) the magnetic field dependent differential conductivities of the contact at $T = 0.32\,K$ are shown. In contrast to UNi_2Al_3–AlO_x–(Ge)–Pb junctions described above the gap structure of the Pb counter electrode in the differential conductivity of UNi_2Al_3–AlO_x–Pb cross-junction was almost completely suppressed in magnetic fields above $\mu_0 H > 0.3\,T$. However, again no trace of an UNi_2Al_3 gap was observed. Only a weak increase of the low bias conductivity, which vanished in magnetic fields above $\mu_0 H > 1.5\,T$ was visible. The origin of this anomaly is not clear. It could be assigned to intrinsic properties of the UNi_2Al_3 base electrode as well as to residual superconductivity of the Pb counter electrode or to barrier imperfections. Neglecting the low bias anomaly it can be assumed, that in magnetic fields above $\mu_0 H > 0.3\,T$ the junction was in a NIN tunneling regime, although the superconductivity of the UNi_2Al_3 base electrode was proven by direct four probe resistivity measurements. The lack of UNi_2Al_3 superconducting features in differential conductivity measurements could be explained by the existence of a normal-conducting layer at the junction interface below the AlO_x insulating barrier. This layer could consist of residual non oxidized Al or non superconducting UNi_2Al_3, which had degradated during the junction preparation process.

In contrast to the possible degradation of the UNi_2Al_3 interface layer the potential problem of non oxidized Al residuals could be directly investigated by the preparation of junctions with various thicknesses of Al layers applying always the same oxidation process. In order to investigate the barrier properties depending on the thickness of the Al layer three junctions with different deposition times of the Al films were prepared. Based on the effective deposition rate of Al, the approximate thicknesses of the resulting Al layers were estimated to: sample#1 – 6.5 nm , sample#2 – 4 nm, sample#3 – 2 nm. For all three junctions the Al barrier was naturally oxidized in 0.8 mbar of dry oxygen for 6 minutes. The area resistances of these three junctions are almost identical and estimated to $\rho_A \simeq 10\Omega mm^2$. The small difference between the area resistances suggests that in all three junctions approximately the same number of Al monolayers was oxidized. Hence, it is reasonable to suppose that the Al layer was not completely
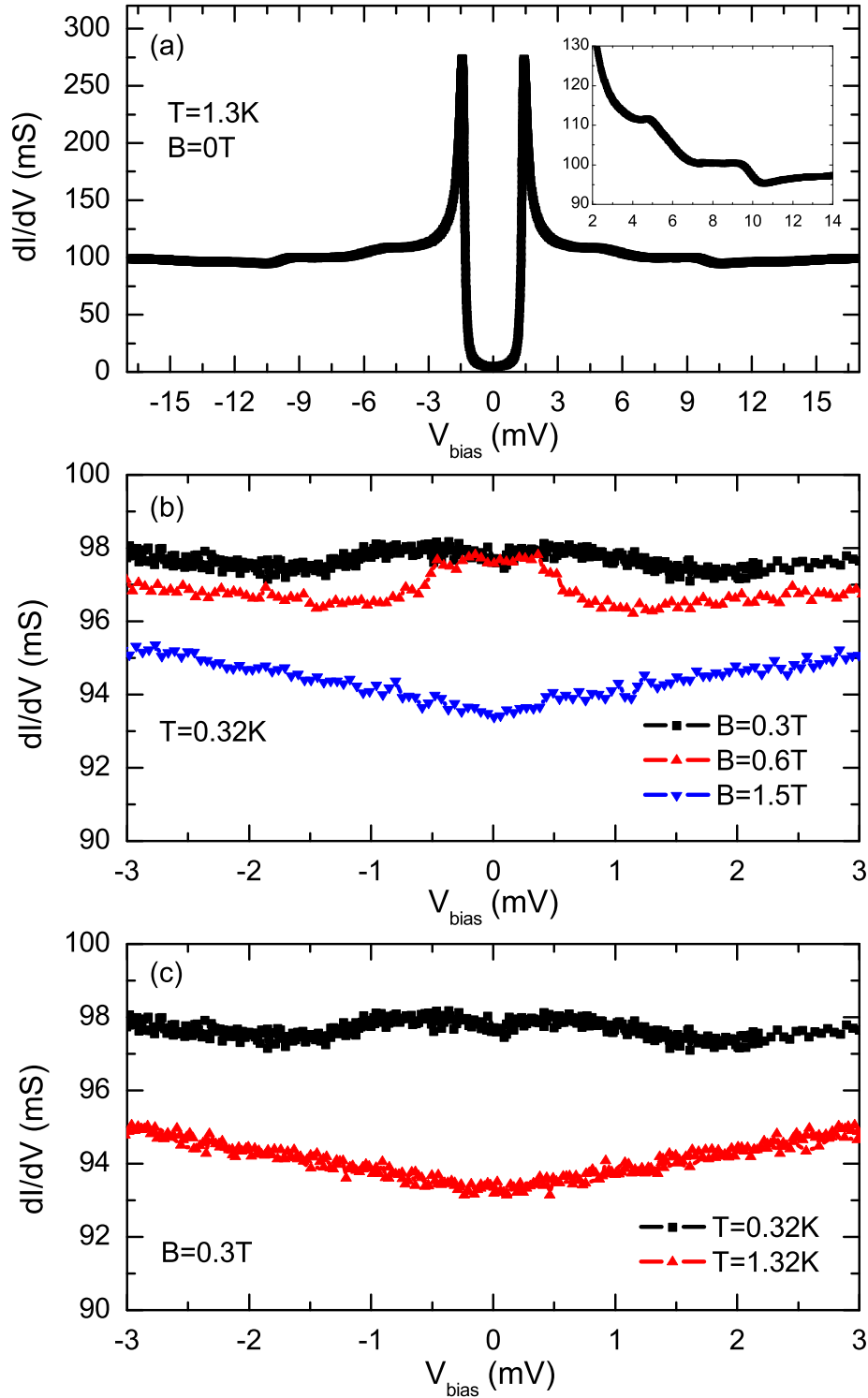
Figure 6.14: UNi_2Al_3–AlO_x–Pb cross type tunnel junction conductivity. Panel (a): Tunneling density of states of the Pb counter electrode. Panel (b): Magnetic field dependent conductivity of a junction at the lowest temperature $T = 0.32$ K. Panel (c): Temperature dependent conductivity of a junction in a magnetic field of $\mu_0 H = 0.3$ T.
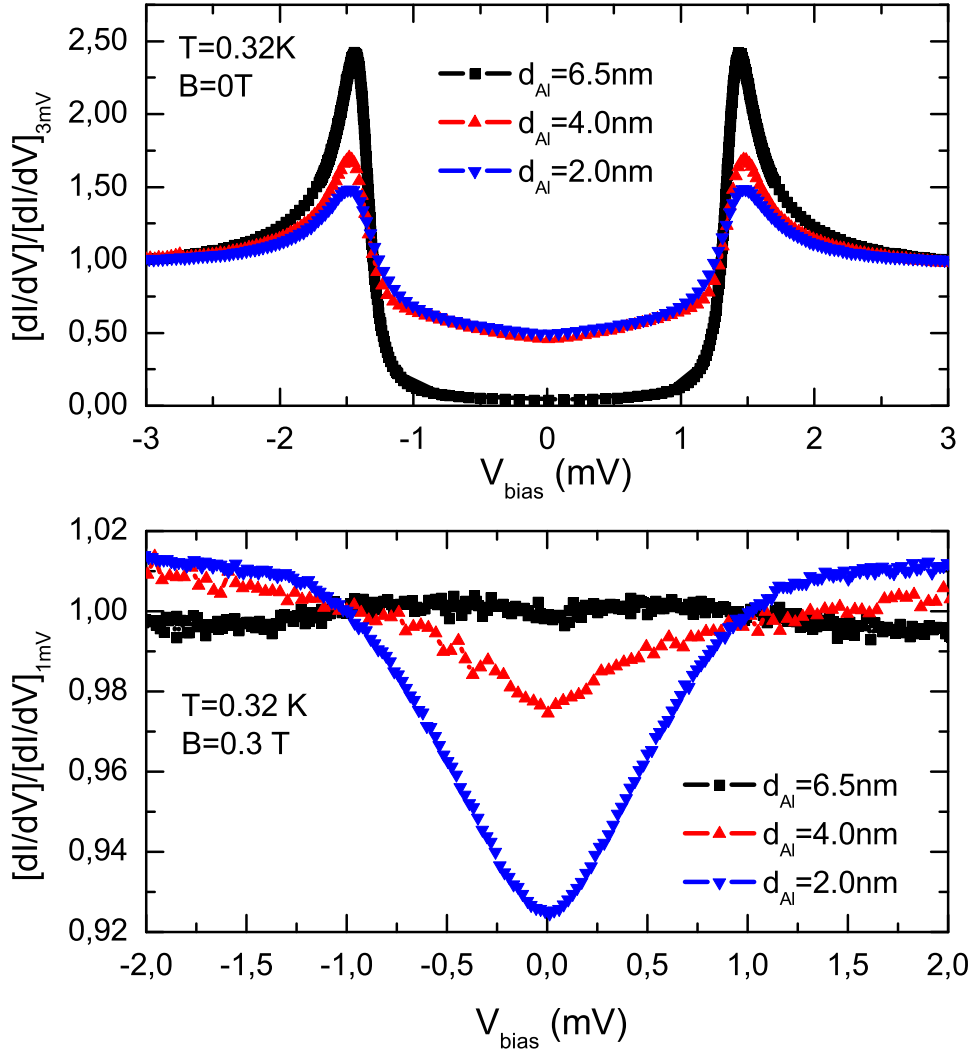
Figure 6.15: UNi$_2$Al$_3$–AlO$_x$–Pb cross junctions with a different barrier thicknesses.
Upper panel: Tunneling density of states of the Pb counter electrode.
Lower panel: Differential conductivity of junctions in a magnetic field of $\mu_0 H = 0.3\,\mathrm{T}$.

oxidized at least in the junction with the thickest barrier layer (sample#1). However, these speculations assume a homogeneous Al film of constant thickness on a flat surface, which is probably not the case for the real UNi_2Al_3–Al interface (see Figure 6.6).

In Figure 6.15 normalized differential conductivities of junctions with different thicknesses of Al layers are compared. The junction with the thickest Al film can be described perfectly by a Dynes-fit for a SIN-junction with a small offset conductivity ($S_{offset} = 2\,mS$) and broadening parameter ($\Gamma = 40\,\mu V$). A reduced barrier thickness results in an increased offset current, but the Pb gap is still clearly visible. If a magnetic field of $\mu_0 H = 0.3\,T$, which should be overcritical for Pb, was applied, the pronounced structure of the Pb gap in the differential conductivity disappeared (Figure 6.15, lower panel). The differential conductivity of the junctions with the thickest barrier remained almost constant at low bias voltages, which is typical for junctions in the NIN tunneling regime. The characteristic feature of junctions with a small barrier thickness is a V-shaped background at low bias voltages ($-1\,mV < V_{bias} < 1\,mV$). This structure became most apparent for the junction with the thinnest Al layer and vanished completely for the junction with the thickest Al film.

Comparing the junction conductivities it can be concluded, that only sample#1 provides an ideal tunneling barrier while the samples #2 and #3 show an increased offset current and a V-shaped background at low bias voltages. Thus, a pinhole-free oxide barrier can be formed only when the Al layer is thick enough. On the other hand, the small difference between the area resistances of the junctions indicate that the barrier thickness of the contacts remains nearly the same. This means that in the case of UNi_2Al_3–Al(AlO_x)-Pb interface the thickness of the deposited Al layer is probably not constant. Thus, the preparation of barriers with a larger amount of Al provides after oxidation a reliable pinhole-free oxide of sufficient thickness on the one hand, but on the other hand it produces as well areas with a too thick Al layer, which is not completely oxidized, resulting in a UNi_2Al_3–Al–AlO_x–Pb tunneling stack. Decreasing the total thickness of the Al layer results in areas with a too thin oxide barrier or even pinholes. Moreover, on the sites where the barrier layer is too thin (or inexistent) the oxidation process will affect the UNi_2Al_3 base electrode as well, changing its properties and the tunneling signal respectively. One could hope that the thickness of the oxide on the Al islands is larger than in Al valleys. In this case the islands would not contribute to the transport process. However, this probably requires that the Al

oxidizes more easy than UNi_2Al_3, which might not be the case considering the U planes, which are perpendicular to the surface in (100)-oriented UNi_2Al_3 film.

Additionally, a contribution of disturbed stoichiometry areas along the borders of the base electrode due to the shadow effect during deposition can not be excluded.

6.4.3 UNi_2Al_3–AlO_x–Ag mesa-junctions

As it was mentioned in the previous section that because of the use of a wet photolithographic processes for the preparation of the mesa-structures the lead counter electrode was replaced by a silver electrode in order to improve the mechanical and anticorrosion stability of the junction. However, in contrast to the superconducting Pb counter electrode the non-superconducting Ag does not allow to prove the existence of a tunneling regime directly. On the other hand, the results described above showed, that the tunneling conductivity of the junctions with lead counter electrode was often affected by residual superconductivity of Pb. For the normal-conducting s-electrons of a silver electrode a perfectly constant density of state at the Fermi energy can be assumed. Thus, this counter electrode can be consider as an ideal normal conductor even in zero magnetic field and all non-ohmic contributions to the tunneling conductivity should be assigned to the UNi_2Al_3 base electrode or to barrier imperfections.

The temperature dependence of the contact resistance of UNi_2Al_3–AlO_x–Ag mesa-junctions is similar to those of cross-junctions. A continuous increase of the resistance by a factor of 2 with decreasing temperature from $300\,K$ to $1\,K$ indicates a pinhole-free barrier consisting of an insulating material. The area resistance of the UNi_2Al_3–AlO_x–Ag mesa-junctions at the lowest temperature is estimated to $\rho_A \simeq 300\Omega mm^2$.

Although a direct prove for a tunneling regime of the junctions is not possible, the barrier quality can be evaluated applying the Simmons [87, 88] or Brinkman [89] models of tunneling conductivity. According to these models, the junction conductivity at high bias voltages exhibits roughly a parabolic dependence when a trapezoidal barrier potential is assumed. The experimental bias-dependent conductance can be fitted to the theoretical model applying the Brinkman formula:

$$\frac{dI/dV(V)}{dI/dV(0)} = 1 - \left(\frac{A_0\Delta\varphi}{16\varphi^{3/2}}\right)eV + \left(\frac{9A_0^2}{128\varphi}\right)(eV)^2,$$

with $A_0 = 4(2m)^{1/2}d/3\hbar$, where φ and d are the average height and width of the

potential barrier, and $\Delta\varphi$ is the asymmetry of the barrier.

In Figure 6.16 the differential conductivity of UNi_2Al_3–AlO_x–Ag mesa junction at $T = 300\,K$ and the corresponding calculation with a Brinkman model are shown. Based on the deposition rate the thickness of the Al layer was estimated to $d = 3\,nm$. From the fit an almost symmetrical barrier potential ($\Delta\varphi = -0.08\,V$) with an average height of $\varphi = 1.4\,V$ and thickness of $d = 2.3\,nm$ were obtained, which is in good agreement with the expected values for a AlO_x insulating barrier. Thus, based on the values of the area resistance of the contact and the Brinkman fit parameters it can be assumed, that a tunneling regime is realized in the UNi_2Al_3–AlO_x–Ag mesa-junction, at least at the room temperature. However, at low temperatures the asymmetry of the differential conductivity increases dramatically, so that the experimental data can not be fitted very well to the theoretical model. This qualitative difference between high and low temperature data puts in doubt the contact quality and accuracy of the fit. However, It

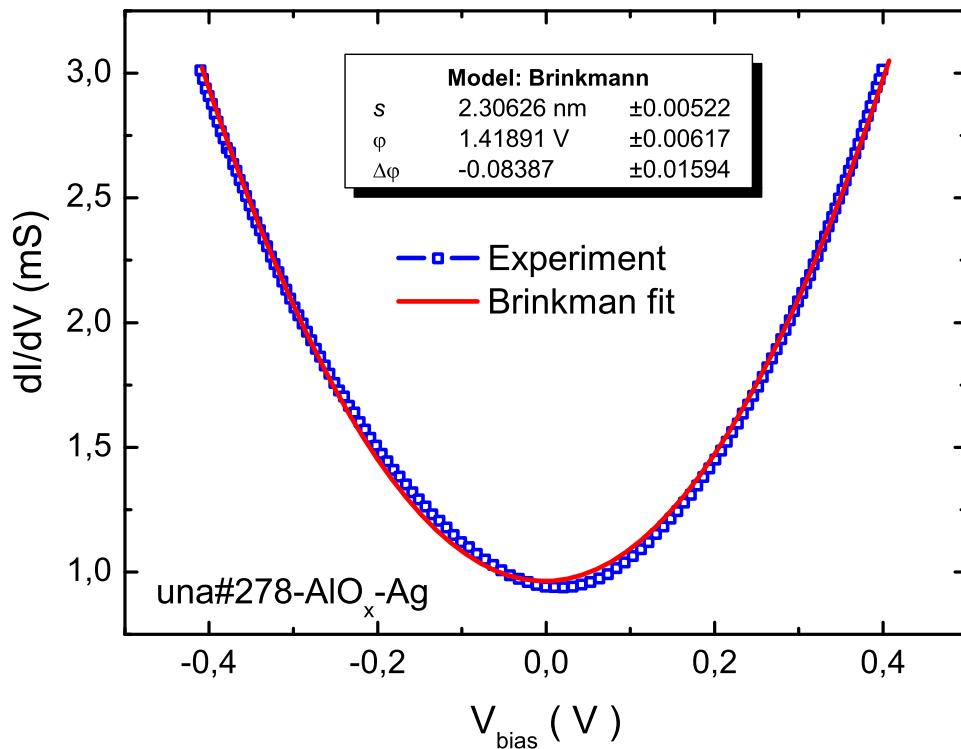
Figure 6.16: Differential conductivity of a mesa-junction ($T = 300\,K$) at high bias voltages and the corresponding Brinkmann fit. The fit parameters s and φ are the average width and height of the potential barrier, $\Delta\varphi$ is the asymmetry of the barrier.

could also be a result of a changing band structure of the heavy fermion system at low temperatures.

On the other hand, recent experimental and theoretical works [90, 91] have demonstrated that a good fit alone cannot prove the quality of a junction. Modelling the electrical and thermal properties of a tunnel junction containing a pinhole, the authors of Ref. [92] have extracted adequate values of the Simmons effective barrier height and effective barrier width even when more than 80% of the current flows through the pinhole short rather than tunneling through the barrier.

Conductivity measurements at temperatures below T_c did not reveal any clear and reproducible evidence of superconductivity of UNi_2Al_3. However, one of the junctions exhibited a conductivity modulation at low bias voltages which can be associated with the superconducting tunneling density of states. In Figure 6.17 the temperature and magnetic field dependent differential conductivities of this UNi_2Al_3–AlO_x–Ag mesa junction are shown. The clearly visible gap-like feature is most pronounced at the lowest temperature and in zero magnetic field. The anomaly becomes weaker with increasing the temperature and vanishes above $T \approx 1\,K$. The external magnetic field suppresses the structure as well and the gap-like feature disappears completely in magnetic fields above $\mu_0 H = 1\,T$. The temperature and magnetic field dependencies of the gap-like structure correlate with the T_c and H_{c2} values of UNi_2Al_3. However, comparing the measured conductivity with a BCS-prediction of the gap size it is obvious, that the structure appears at too high bias voltages. On the other hand, a large parallel ohmic conductivity $\sigma_{parallel} \approx 0.3\,S$ measured at the zero bias reveals large pin hole current contributions to the total conductivity. Due to the low total resistance of the contact and the strongly inhomogeneous distribution of the current the real voltage drop across the tunneling barrier can differ from the measured bias voltage, so that the true bias voltage scale can not be determined properly. However, alternative explanations of the origin of the gap-like structure, such as tunneling into superconducting nonoxidized Al are also possible. Since the structure was observed only for one junction, which was strongly influenced by pin hole shorts, this result should not be used to evaluate the superconducting order parameter of UNi_2Al_3.

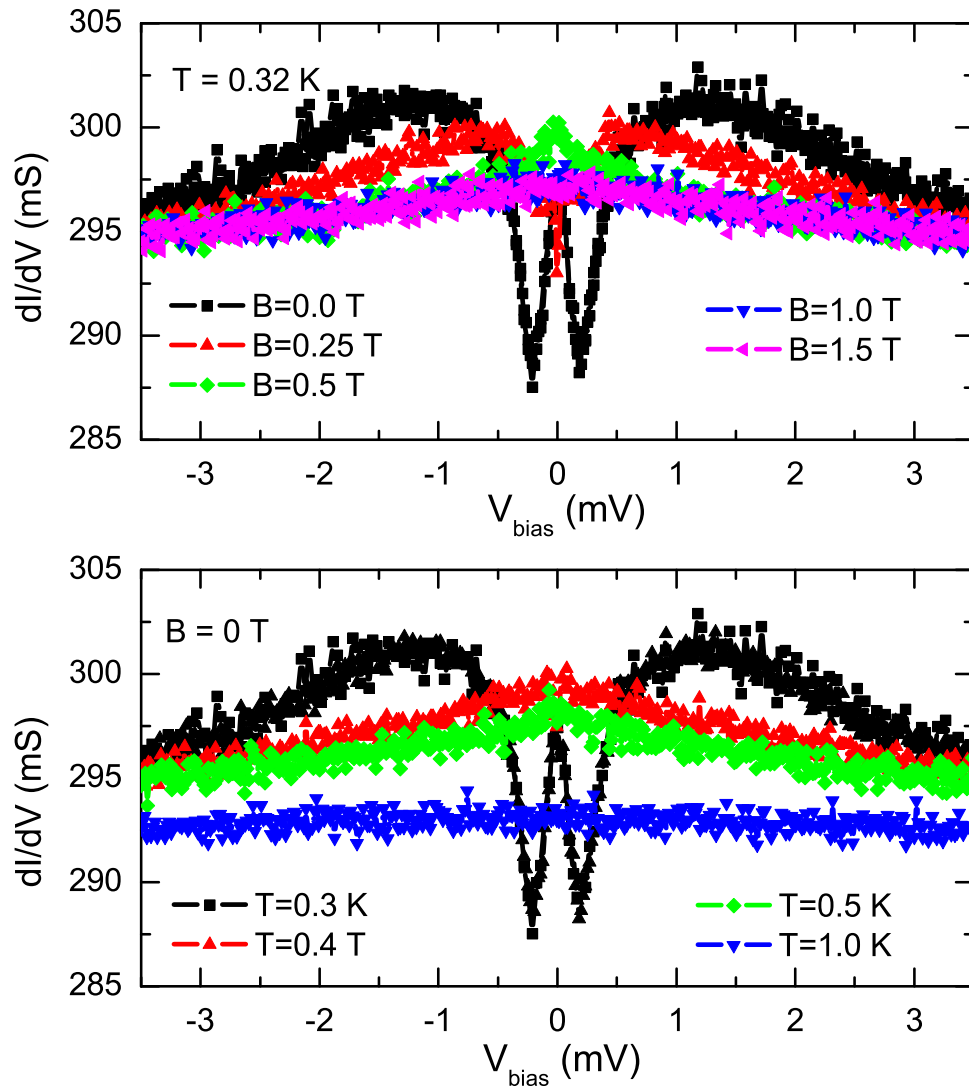Figure 6.17: Differential conductivity of an UNi_2Al_3–AlO_x–Ag mesa-junction. Upper panel: Magnetic field dependent conductivity of the junction at the lowest temperature $T = 0.32$ K. Lower panel: Temperature dependent conductivity of the junction in zero magnetic field.

6.5 Conclusion

There are several possibilities to interpret the experimental tunneling data. The absence of superconducting features of UNi_2Al_3 in the tunneling spectra can be explained by imperfection of the tunneling contacts as well as by intrinsic properties of UNi_2Al_3. The tunneling spectroscopy experiments show, that the preparation of the ideal tunneling junction is more an art than a technique. Therefore, a tunneling contact failure is the most probable reason for the lack of superconducting gap features of UNi_2Al_3. Firstly, the UNi_2Al_3 base electrode could be normal conducting in the bulk and superconducting only in some percolation path. However, the high critical current density measured for UNi_2Al_3 films ($I_c^{0.3K} \approx 10^4 \, A/cm^2$) corresponds to bulk superconductivity. Alternatively, superconductivity could be suppressed just in a degraded surface layer, which is actually probed by tunneling spectroscopy. Finally, the insulating layer could be oxidized not completely, resulting the tunneling into non superconducting Al.

Assuming an unconventional superconducting order parameter of UNi_2Al_3, alternative explanations such as intrinsic pair breaking effects at the interface to the barrier are also possible. Additionally, recent theoretical work of D. Parker and P. Thalmeier concerning tunneling spectroscopy on UPd_2Al_3 suggests, that the behavior of the tunneling conductance can differ radically depending on the metal used on the normal side [93]. Assuming translational invariance of the transmission (reflection) process parallel as well as perpendicular to the barrier interface and considering only a cylindrical part of the UPd_2Al_3 Fermi surface, the authors of Ref. [93] have shown, that the measured gap magnitude, the zero-energy density of states and even the existence of a zero bias anomaly depends strongly on the counter electrode material. Since the Fermi surfaces of UPd_2Al_3 and UNi_2Al_3 are very similar, it is necessary to the consider the material of the counter electrode interpreting the tunneling experiments on UNi_2Al_3-based junctions as well.

Summary

The heavy fermion superconductors UNi_2Al_3 and UPd_2Al_3 both exhibit the coexistence of superconductivity and magnetic order at low temperatures, stimulating speculations about possible unconventional (non-phononic) Cooper-pairing interactions in these compounds. Although UNi_2Al_3 and UPd_2Al_3 are isostructural, they display important differences, which help to understand the interplay between magnetism and superconductivity, an area of active debate in condensed matter physics. However, in contrast to UPd_2Al_3, there is less progress in the experimental investigation of UNi_2Al_3 due to the lack of high quality samples. The present thesis concentrates on the preparation, characterization and electronic properties investigations of UNi_2Al_3 single crystalline thin film samples.

The preparation of thin films was accomplished by coevaporation of the elementary components on heated substrates in a molecular beam epitaxy (MBE) system. (100)-oriented epitaxial thin films of UNi_2Al_3 were grown on single crystalline $YAlO_3$ substrates cut in (010)- or (112)-direction. The optimal deposition parameters were found by a systematical variation of the substrate temperature and of the evaporation rates and investigations of the film quality by means of diffraction experiments and transport measurements.

Several different methods were involved for the detailed investigation of the crystallographic quality of the samples. In situ reflection high energy electron diffraction (RHEED), comprehensive x-ray analysis, as well as TEM measurements proved in-plane and out-of-plane order of the UNi_2Al_3 thin films. Considering the width of the Bragg reflection peaks, it can be assumed that the structural correlation extends over the complete film thickness.

Resonant magnetic x-ray scattering was employed to investigate the magnetic state of the epitaxial thin films. The observed incommensurate propagation vector as well as the Neél temperature correspond to those of bulk samples. The magnetic correlation length $\ell > 800\text{Å}$, estimated from resonant magnetic x-ray scattering on a 1200Å film, exceeds the lower boundary obtained from neutron

scattering experiments on bulk samples. It was found that out of the three possible magnetic domains the one with the moment direction perpendicular to the film surface was not realized. The formation of this domain seems to be energetically unfavorable, since it would imply an uncompensated magnetic moment.

Transport measurements were performed in order to investigate the electronic properties of UNi_2Al_3 thin films in the normal and superconducting states. The best samples have the residual resistance ratio $RRR = R_{300K}/R_{1.1K}$ of about $RRR \simeq 10$ with residual resistance amounting to $\rho_a = 12\,\mu\Omega$cm and become superconducting at $T_c^{max} = 1.05$K with resistive transition widths $\Delta T_c \simeq 0.06$K.

The temperature dependent resistivity $\rho(T)$ showed a pronounced anisotropy depending on the probe current direction. Moreover, it has been found that the resistive transition temperature T_c is not the same for different current direction. All of the measured superconducting samples on both kinds of substrate showed the superconducting transition for current direction $I \parallel c$ at a slightly reduced temperature compared to $I \parallel a$. Since only a negligible influence of the probe current density on T_c was observed, the split superconducting transition was assumed to be an intrinsic property of UNi_2Al_3. A possible explanation for this effect is multiband superconductivity with two superconducting gaps opening at different temperatures on different sheets of the Fermi surface of UNi_2Al_3. In a real multiband superconductor a weak coupling between two band should result in a common T_c. However, in one of the bands an initially tiny energy gap is expected which opens drastically at a reduced temperature compared to T_c. The observation of two different resistive transition temperatures in UNi_2Al_3 thin films can be explained by critical current effects, hiding the tiny energy gap.

The influence of the magnetic ordering at $T_N \simeq 5$K on $R(T)$ was found to be strongly anisotropic, indicating different coupling between the magnetic moments and itinerant charge carriers on the multi-sheeted Fermi surface. The higher superconducting T_c has been observed on the Fermi surface sheet which is more affected by the magnetic ordering, providing evidence that the same electrons are responsible for superconductivity and magnetism.

Measurements of the temperature dependent upper critical magnetic field $H_{c2}(T)$ of the thin film samples reveal much less anisotropy than reported for bulk single crystals. Independent of the field and current direction a contribution of paramagnetic pair breaking was observed. The initial slope of the upper critical field $H'_{c2}(T)$ of thin film samples suggests a spin-singlet superconducting state in UNi_2Al_3, as opposed to bulk single crystal data.

Within this work many planar tunneling junctions of different design were prepared employing different techniques. The artificial tunneling barrier was formed by the oxidation of thin Al layers, deposited on the top of the UNi_2Al_3 base electrodes. As a counter electrode material superconducting Pb as well as normal conducting Ag were used. All preparation steps between the deposition of base and counter electrodes were performed without breaking the vacuum in order to avoid a non-controlled oxidation of interface layers. The barrier quality was evaluated applying the standard Brinkman model or directly from the observation of the well-known superconducting tunneling density of states of the Pb counter electrode. Despite the realization of junctions in the tunneling regime, no features of the superconducting density of state of UNi_2Al_3 was ever observed. It is possible that the absence of the UNi_2Al_3 gap features in the tunneling spectra was caused by imperfections of the tunneling contacts. The superconductivity of UNi_2Al_3 could be suppressed just in a degraded surface layer, resulting in tunneling into non superconducting UNi_2Al_3. However, an alternative explanation such as intrinsic pair breaking effects at the interface to the barrier is also possible. In order to gain more knowledge about tunneling experiments with heavy fermion superconductors the investigation of additional compounds would be helpful.

Bibliography

[1] F. Steglich, J. Aarts, C. D. Bredel, W. Lieke, D. Meschede, W. Franz, and H. Schäfer, *Phys. Rev. Lett.* **43**, 1892 (1979).

[2] N. Grewe and F. Steglich, *Heavy Fermions*, in *Handbook on the Physics and Chemistry of Rare Earths*, Vol. 14, chapter 97, Elsevier Science Publishers, Amsterdam (1991).

[3] F. Steglich, C. Geibel, K. Gloos, G. Olesch, C. Schank, C. Wassilew, A. Loidel, A. Krimmel, and G. R. Stewart, *J. Low. Temp. Phys.* **95**, 3 (1994).

[4] M. B. Maple, Y. Dalichaouch, M. C. de Andrade, N. R. Dilley, J. Herrmann, and R. Movshovich, *J. Phys. Chem. Solids* **56**, 1963 (1995).

[5] G. R. Stewart, Z. Fisk, J. O. Willis and J. L. Smith, *Phys. Rev. Lett.* **52**, 679 (1984).

[6] H. R. Ott, H. Rudigier, Z. Fisk, and J. L. Smith, *Phys. Rev. Lett.* **50**, 1595 (1983).

[7] T. T. M. Palstra, A. A. Menovsky, J. van den Berg, A. J. Dirkmaat, P. H. Kes, G. J. Nieuwenhuys, and J. A. Mydosh, *Phys. Rev. Lett.* **55**, 2727 (1985).

[8] C. Geibel, C. Schank, S. Thies, H. Kitazawa, C. D. Bredel, A. Böhm, M. Rau, A. Grauel, R. Caspary, R. Helfrich, U. Ahlheim, G. Weber, and F. Steglich, *Z. Phys. B* **84**, 1 (1991).

[9] C. Geibel, S. Thies, D. Kaczorowski, A. Mehner, A. Grauel, B. Seidel, U. Ahlheim, R. Helfrich, K. Petersen, C. D. Bredl and F. Steglich, em Z. Phys. B **83**, 305 (1991).

[10] H. R. Ott, *J. Low. Temp. Phys.* **95**, 95 (1994).

[11] B. Lüthi, B. Wolf, D. Finsterbusch, and G. Bruls, *Physica B* **204**, 228 (1995).

[12] F. Steglich, P. Gegenwart, C. Geibel, R. Helfrich, P. Hellmann, M. Lang, A. Link, R. Modler, G. Sparn, N. Büttgen, and A. Loidel, *Physica B* **223& 224**, 1 (1996).

[13] D. L. Cox and M. B. Maple, *Phys. Tod.* **275**, 32 (1995).

[14] R. H. Heffner and M. R. Norman, *Comm. Cond. Mat. Phys.* **17**, 361 (1996).

[15] M. Jourdan, M. Huth, and H. Adrian, *Nature* **398**, 47 (1999).

[16] N. Metoki, Y. Haga, Y. Koike, and Y. Onuki, *Phys. Rev. Lett.* **80**, 5417 (1998).

[17] N. Bernhoeft, N. Sato, B. Roessli, N. Aso, A. Hiess, G. H. Lander, Y. Endoh, and T. Komatsubara, *Phys. Rev. Lett.* **81**, 4244 (1998).

[18] N. K. Sato, N. Aso, K. Miyake, S. Shiina, P. Thalmeier, G. Vareloggiannis, C. Geibel, F. Steglich, P. Fulde, and T. Komatsubara, *Nature* **410**, 340 (2001).

[19] N. Bernhoeft, *Eur. Phys. J. B* **13**, 685 (2000).

[20] P. Thalmeier, Eur. Phys. J. B **27**, 29 (2002).

[21] P. McHale, P. Fulde and P. Thalmeier, *Phys. Rev. B* **70**, 014513 (2004).

[22] L. Paolasini, J. A. Paixao, G. H. Lander, P. Burlet, N. Sato, T. Komatsubara, *Phys. Rev. B* **49**, R7072 (1994).

[23] A. Schröder, J. G. Lussier, B. D. Gaulin, J. D. Garrett, W. J. L. Buyers, L. Rebelsky, and S. M. Shapiro, *Phys. Rev. Lett.* **72**, 136 (1994).

[24] N. Aso, B. Roessli, N. Bernhoeft, R. Calemczuk, N. K. Sato, Y. Endoh, T. Komatsubara, A. Hiess, G. H. Lander, H. Kadowaki, **Phys. Rev. B 61**, R11 867 (2000).

[25] A. Hiess, P. J. Brown, E. Lelievre-Berna, B. Roessli, N. Bernhoeft, G. H. Lander, N. Aso, and N. K. Sato, Phys. Rev. B **64**, 134413 (2001).

[26] H. Tou, Y. Kitaoka, K. Asayama, C. Geibel, C. Schank, and F. Steglich, *J. Phys. Soc. Jpn.* **64**, 725 (1995).

[27] K. Matsuda, Y. Kohori, and T. Kohara, *Phys. Rev. B* **55**, 12233 (1997).

[28] K. Gloos, R. Modler, K. Schimanski, C. D. Bredl, C. Geibel, F. Steglich, A. I. Buzdin, N. Sato, and T. Komatsubara, *Phys. Rev. Lett.* **70**, 501 (1993).

[29] M. Jourdan, *Tunneling spectroscopy of the heavy-fermion superconductor* UPd_2Al_3 PhD-thesis (1999) , Institut für Physik, Johannes Gutenberg-Universität Mainz, Mainz, Germany (unpublished).

[30] N. Sato, N. Koga, and T. Komatsubara, *J. Phys. Soc. Jpn.* **65**, 1555 (1996).

[31] T. Terashima, K. Enomoto, T. Konoike, S. Uji, N. K. Sato and H. Yamagami, *Physica B* **378-380**, 991 (2006).

[32] K. Ishida, D. Ozaki, T. Kamatsuka, H. Tou, M. Kyogaku, Y. Kitaoka, N. Tateiwa, N. K. Sato, N. Aso, C. Geibel, and F. Steglich, *Phys. Rev. Lett.* **89**, 037002 (2002).

[33] M. Mihalik, F. E. Kayzel, T. Yoshida, K. Kuwahara, H. Amitsuka, T. Sakakibara, A. A. Menovsky, J. A. Mydosh, J. J. M. Franse, Physica B **230**, 364 (1997).

[34] C. Geibel, Physica B **186**, 188 (1993).

[35] M. Jourdan, A. Zakharov, M. Foerster, and H. Adrian, Phys. Rev. Lett. **93**, 097001 (2004).

[36] M. Jourdan, A. Zakharov, H. Schneider and H. Adrian, *Physica B* **359**, 1153 (2005).

[37] M. Foerster, A. Zakharov, and M. Jourdan *Phys. Rev. B* **76**, 144519 (2007).

[38] A. Zakharov, M. Jourdan, and H. Adrian, *AIP Conference Proceedings* **850**, 655 (2006).

[39] M. Dressel, N.V. Kasper, B. Gorshunov, K. Petukhov, D.N. Peligrad, M. Jourdan, M. Huth, and H. Adrian, *Phys. Rev. B* **66**, 035109 (2002).

[40] M. Scheffler, M. Dressel, M. Jourdan, and H. Adrian, *Nature* **438**, 1135 (2005).

[41] M. Scheffler, M. Dressel, M. Jourdan, and H. Adrian, *Physica B* **378-380**, 993 (2006).

[42] M. Henzler and W. Göpel, *Oberflächenphysik des Festkörpers*, Teubner, Stuttgart (1994).

[43] L. C. Feldman and J. W. Mayer, *Fundamentals of surface and thin film analysis*, North-Holland, New York (1986).

[44] M. A. Herman and H. Sitter, *Molecular Beam Epitaxy*, Springer, Berlin (1989).

[45] D. T. J. Hurle, eds. , *Handbook on Crystal Growth 3a,3b – Thin Films and Epitaxy*, North-Holland, Amsterdam (1993).

[46] P. Wagner, *Präparation epitaktischer Filme der Hochtemperatursupraleiter* $YBa_2(Ca_{1-x}Zn_x)O_7$ *und* $Bi_2Sr_2CaCu_2O_{8+\delta}$ *mittels DC-Hochdruck-Sputtern und Messung charakteristischer Eigenschaften.* Diploma-thesis (1991), Institut für Festkörperphysik, TU-Darmstadt, Germany (unpublished).

[47] M. Huth, *Transportphänomene und Kohärenz in epitaktisch gewachsenen Schwere-Fermionen-Supraleiter Filmen.* PhD-thesis (1995), Institut für Festkörperphysik, TU-Darmstadt, Darmstadt, Germany (unpublished).

[48] W Braun *Applied RHEED: reflection high-energy electron diffraction during crystal growth*, Springer, Berlin (1999).

[49] I. Hernández-Calderon and H Höchst Phys. Rev. B **27**, 4961 (1983)

[50] L. G. Parratt, *Phys. Rev.* **5**, 359 (1954).

[51] L. Nevot, P. Croce, *Rev. Phys. App.* **15**, 761 (1980).

[52] P. F. Miceli, C. J. Palmstrom, *Phys. Rev. B* **51**, 5506 (1995).

[53] M. Jourdan, *Präparation und Thermokraft dünner Schichten der Schwere-Fermionen-Supraleiter* UPd_2Al_3 *und* UNi_2Al_3. Diploma-thesis (1995), Institut für Festkörperphysik, TU-Darmstadt, Darmstadt, Germany (unpublished).

[54] P. M. Platzmann and N. Tzoar, *Phys. Rev. B* **2**, 3556 (1970).

[55] F. de Bergevin and M. Brunel, *Phys. Lett. A* **39**, 141 (1972).

[56] G. H. Lander and W. G. Stirling *Physica Scripta* **T45**, 15 (1992).

[57] J. P. Hannon, G. T. Trammell, M. Blume, and D. Gibbs, *Phys. Rev. Lett.* **10**, 1245 (1988).

[58] J. H. Hill and D. F. McMorrow, Acta Cryst. **A52**, 236 (1996).

[59] e. g. A. Guinier, *X-Ray Diffraction In Crystals, Imperfect Crystals and Amorphous Bodies* (Dover Publications, New York 1994) 90.

[60] N. Bernhoeft, *Acta Cryst.* **A55**, 274 (1999).

[61] S. Süllow, B. Becker, A. de Visser, M. Mihalik, G. J. Nieuwenhuys, A. A. Menovsky, and J. A. Mydosh, *J. Phys. Condens. Matter* **9**, 913 (1997).

[62] H. Suhl, B. T. Matthias, and L. R. Walker, *Phys. Rev. Lett.* **3**, 552 (1959).

[63] P. Oppeneer (private communication).

[64] K. Knöpfle, A. Marromaras, L. M. Sandratskii, and J. Kübler, *J. Phys.: Condens. Matter* **8**, 901 (1996).

[65] G. Zwicknagl, A. Yaresko, and P. Fulde, *Phys. Rev. B* **68**, 052508 (2003).

[66] N. Sato, T. Sakon, N. Takeda, T. Komatsubara, C. Geibel, F. Steglich, *J. Phys. Soc. Jpn.* **61**, 32 (1992).

[67] M. B. Maple, J. W. Chen, Y. Dalichaouch, T. Kohara, C. Rossel, M. S. Torikachvili, M. W. McElfresh, and J. D. Thompson, *Phys. Rev. Lett.* **56**, 185 (1986).

[68] N. R. Werthamer, E. Helfand, and P. C. Hohenberg, Phys. Rev. **147**, 295 (1966); K. Maki, *ibid.* **148**, 392 (1966).

[69] R. R. Hake, *Appl. Phys. Lett.* **10**, 186 (1967).

[70] E. Helfand and N. R. Werthamer, *Phys. Rev.* **147**, 288 (1966).

[71] A. M. Clogston, *Phys. Rev. Lett.* **9**, 266 (1962).

[72] Y. Dalichaouch, M. C. de Andrade, and M. B. Maple, Phys. Rev. B **46**, 8671 (1992).

[73] I. Giaever, *Phys. Rev. Lett.* **5**, 147, 464 (1960).

[74] J. Bardeen, L. N. Cooper, J. R. Schriffer, *Phys. Rev.* **108**, 1175 (1957).

[75] See, for example, M. Tinkham, *Introduction to superconductivity*, (McGraw-Hill, New York, 1996).

[76] J. M. Rowell and L. Kopf, *Phys. Rev.* **137**, A907 (1965).

[77] R. Stedman, L. Almqvist, and G. Nilsson, *Phys. Rev.* **162**, 549 (1967).

[78] I. Giaever and K. Megerle, *Phys. Rev.* **122**, 1101 (1961).

[79] I. Giaver, H. R. Hart, and K. Megerle, *Phys. Rev.* **126**, 941 (1962).

[80] J. Vrba and S. B. Woods, *Can. J. Phys*, **50**, 548 (1972).

[81] J. M. Rowell, M. Gurvitch, and J. Geerk, *Phys. Rev. B* **24**, 2278 (1981).

[82] R. Dolata, M. Neuhaus, W. Jutzi, *Physica C* **241**, 25 (1995).

[83] K. Joosse, H. Nakagawa, H. Akoh, S. Takada, K. Maehata, and K. Ishibashi, *Appl. Phys. Lett.* **68**, 702 (1996).

[84] N. Rando, P. Videler, A. Paecock, A. Van Dorrecht, P. Verhoeve, R. Venn, A. C. Wright, and J. Lumley, *J. Appl. Phys* **77**, 4099 (1995).

[85] W. Bangert, J. Geerk, and P. Schweiss, *Phsy. Rev. B* **31**, 6066 (1985).

[86] A. Conca, *Magnetic tunneling junctions with the Heusler compound* $Co_2Cr_{0.6}Fe_{0.4}Al$. PhD-thesis (2007), Institut für Physik, Johannes Gutenberg-Universität Mainz, Mainz, Germany (unpublished).

[87] J. G. Simmons, *J. Appl. Phys.* **34**, 1793 (1963).

[88] J. G. Simmons, *J. Appl. Phys.* **35**, 2655 (1964).

[89] W F Brinkman, R C Dynes, and J M Rowell, *J. Appl. Phys.* **41**, 1915 (1970).

[90] B. J. Joňsson-Akerman, R. Escudero, C. Leighton, S. Kim, I. K. Schuller,and D. A. Rabson, *Appl. Phys. Lett.* **77**, 1870 (2000).

[91] J. J. Akerman, R. Escudero, C. Leighton, S. Kim, D. A. Rabson, R. W. Dave, J. M. Slaughter, and I. K. Schuller, *J. Magn. Magn. Mater.* **240**, 86 (2002).

[92] Z. -S. Zhang and D. A. Rabson, *J. Appl. Phys.*, bf 95 557 (2004).

[93] D. Parker and P. Thalmeier *Phys. Rev. B* **75**, 184502 (2007).

Publications closely related to the present work

Anisotropic transport properties of UNi$_2$Al$_3$thin films

M. Foerster, A. Zakharov, and M. Jourdan

Phys. Rev. B **76**, 144519 (2007)

Tunneling spectroscopy on epitaxial UNi$_2$Al$_3$thin films

A. Zakharov, M. Jourdan, and H. Adrian

AIP Conference Proceedings **850**, 655 (2006)

Magnetic order in thin films of the heavy fermion superconductor UNi$_2$Al$_3$

M. Jourdan, A. Zakharov, A. Hiess, T. Charlton, N. Bernhoeft, and D. Mannix

Eur. Phys. J. B **48**, 445 (2005)

Preparation of superconducting thin films of UNi$_2$Al$_3$

A. Zakharov, M. Jourdan, M. Foerster and H. Adrian

Physica B **359**, 1108 (2005)

Transport anisotropy and B-c2(Theta, T) of UNi$_2$Al$_3$thin films

M. Jourdan, A. Zakharov, H. Schneider and H. Adrian

Physica B **359**, 1153 (2005)

Evidence for multiband superconductivity in the heavy fermion compound UNi$_2$Al$_3$

M. Jourdan, A. Zakharov, M. Foerster, and H. Adrian

Phys. Rev. Lett. **93**, 097001 (2004)

Preparation of thin films of the heavy fermion superconductor UNi$_2$Al$_3$

M. Jourdan, A. Zakharov, M. Foerster, and H. Adrian

J. Magn. Mag. Mat. **272**, E163-E164 (2004)

Lebenslauf

Persönliche Daten:

Name:	Andrey Zakharov
Geburtstag:	23.1.1980
Geburtsort:	Kharkiv, Ukraine
Familienstand:	verheiratet
Nationalität:	ukrainisch

Ausbildung:

1987-1997	Allgemeinbildende Schule N. 35, Kharkiv
Jun. 1997	Abitur
Jul. 1997	Immatrikulation am Fachbereich Physik der Kharkiv National-Universität
Jul. 2002	Diplom. Thema der Arbeit: *Influence of point-like defects on the guided motion of vortices in high-T_c superconductors*
Sept. 2002 - Aug. 2006	Wissenschaftlicher Angestellter am Institut für Physik der Johannes Gutenberg-Universität, Mainz
Sept. 2002	Beginn der Promotion am Fachbereich Physik der Johannes Gutenberg-Universität, Mainz
Sept. 2006 - Jul. 2007	Fertigungsingenieur bei AMD, Dresden
Seit Aug. 2007	Prozessingenieur bei AMD, Dresden